UNIVERSITÀ DI PARMA

UNIVERSITA' DEGLI STUDI DI PARMA

DOTTORATO DI RICERCA IN
Scienza e Tecnologia dei Materiali

CICLO XXXVII

Investigation of crystallization and growth of oxides and metals towards sustainability

Coordinatore:
Chiar.mo Prof. Enrico Dalcanale
Tutor:
Chiar.mo Prof. Ludovico Cademartiri

Dottorando: Dario Florio

Anni Accademici 2021/2022 – 2023/2024

UNIVERSITÀ DI PARMA

UNIVERSITA' DEGLI STUDI DI PARMA

DOCTORAL COURSE IN
Materials Science and Technology

Cycle XXXVII

Investigation of crystallization and growth of oxides and metals towards sustainability

Coordinator:
Chiar.mo Prof. Enrico Dalcanale
Supervisor:
Chiar.mo Prof. Ludovico Cademartiri

Candidate: Dario Florio

Academic Years 2021/2022 – 2023/2024

"Even after the coldest winter,

the cherry trees will bloom again."

Dario Florio

dario.florio@unipr.it

Department of Chemical Sciences, Life and Environmental Sustainability

Università degli Studi di Parma

Parco Area delle Scienze 17/A

I-43124 Parma, Italy

Tables of Contents

1 Introduction

Reducing global energy consumption is a critical challenge in pursuing of sustainable development, as the current levels of energy use are closely linked to environmental degradation and climate change. Industrial processes, which account for a significant portion of global energy demand, play a pivotal role in this context.

Crystallization is a key process in various industries, such as in producing chemicals, pharmaceuticals, electronic components, and food products, areas in which a high level of purity is essential. The specific requirements in temperature control and thus energy consumption of crystallization can vary depending on the type of crystallization procedure (e.g., heating, evaporation, reactive crystallization, seeding) and the scale of production. Among these, SiO_2 crystallization, possibly required in a very wide range of different forms and combinations, as bulk or nanostructures, as stand-alone, in alloys or composite systems, is a significant energy-demanding process, particularly in the semiconductor, glass and ceramic, and solar energy industries, where high-purity and carefully controlled crystal structures are required. SiO_2, one of the most abundant materials on Earth, is well known for its extensive polymorphism, exhibiting distinct physical and chemical properties for each of the distinguished crystalline structures. Controlling the crystallization process is therefore crucial to ensuring the material's applicability in a specific technological field. The sectors mentioned above in which silica is involved are central to the development of modern technology, and advancements in reducing the energy footprint of SiO_2 crystallization processes are extremely important for enhancing sustainability in these industries.

Another global energy-intensive industrial activity is the production and manufacturing of metals. This sector includes the mining of ores, smelting, refining,

and the fabrication of metal products. For example, aluminium and steel production are particularly energy-consuming due to the high temperatures required for smelting and processing. For instance, steel production alone is responsible for about 7-9% of global CO_2 emissions, reflecting its high energy demand. Among the most employed materials, iron is not only crucial due to its abundance (6.3% only on the earth's crust) but also because of its versatile mechanical properties, such as high strength, ductility, and hardness, which make it indispensable for a wide range of bulk applications, including construction, infrastructure, and manufacturing. However, achieving the desired mechanical properties in iron often necessitates multiple industrial treatments, such as heating, cooling, alloying, and surface treatments. Consequently, this enhancement of iron's properties to meet specific industrial requirements, such as increased wear resistance or improved tensile strength, contributes to supplementary costs and energetic consumptions to obtain the final efficient product. While iron's mechanical properties and broad applications are fundamental to modern industry, they come with a high energy cost, highlighting the importance of optimizing production processes to reduce the overall energy footprint of this metal. Notably, an intrinsic improvement of the mechanical properties (but not only) of metals is observed when their dimensions are reduced to the nanoscale, mainly thanks to their unique high values of area-to-volume ratio, dimension scale materials in which some properties results enhanced with respect to the one of the equivalent bulk materials. Consequently, conveying nanomaterials advanced features in a massive structure could enable higher throughput, lower energy consumption (e.g., in transportation), and greater precision in these processes, thereby pushing the boundaries of current technological capabilities.

Crystallization and metal manufacturing are thus only a few sectors in which innovations in process design, materials, and technologies that can minimize energy usage while maximizing efficiency are therefore of paramount importance. These advancements can significantly reduce the environmental impact of industrial activities, thereby supporting global efforts towards a more sustainable future.

Within this framework, the present PhD thesis explores fundamental synthetic studies as a first step in reducing the impact of specific crystallization and metal manufacturing problems.

Specifically, the thesis investigates the phase transformation of SiO_2 from amorphous to crystalline structures, focusing on Metal-Induced Crystallization as a method to modify and potentially lower the crystallization temperature required for polymorph transformations compared to traditional methods. Various experiments were conducted using different metals as a source of crystallization, and hypotheses have been proposed regarding the fundamental mechanisms driving this process, which is at the current state of the art in literature not clear.

In parallel, as a side project, different home-made experimental setups, similar conceptually to the Chemical Vapor Deposition, have been designed and developed in order to synthesize massive quantities of nanostructured iron, with the aim to put a first step investigation to transfer the peculiar properties of nanostructures to the large-scale bulk applications.

2 Investigation of crystallization catalysis mechanisms on amorphous SiO_2

2.1 Metal-induced crystallization: state of the art and open questions

2.1.1 The importance of crystals

Crystalline materials are essential to the technological advancements of modern society. Their applications, whether in bulk or thin-film forms, are vast and crucial across numerous high-tech fields. Among them, crystals have played a pivotal role in the development of modern electronics[1], optical-fiber communications[2], solid-state lasers[3], optical industry[4], and high-efficiency photovoltaic sector[5]. Beyond these advanced technologies, crystallization techniques are also fundamental in the production of everyday consumer items, such as sugar and salt[6,7], pharmaceutical compounds and new drugs[8]. The increasing demand for crystals with specific sizes and high quality drives ongoing improvements in production methods, aiming to reduce costs and enhance the performance of these materials.

The evolution of crystal growth techniques is remarkable. From the initial experiments with supersaturated solutions in the 18th century to the sophisticated growth technologies of the 20th century, there has been significant progress. These include advancements in temperature gradient control, mechanistic movements within growth equipment, and a deeper understanding of the fundamental processes involved in crystal growth. Historically, crystal growth was primarily a curiosity or

a means to produce materials for academic research and gemstones. However, the discovery of germanium and silicon transistors in the mid-20th century marked a turning point[9,10]. These breakthroughs laid the foundation for modern microelectronics and catalyzed the growth of the enormous silicon industry that underpins today's technological landscape[11,12].

The growth of inorganic materials often leads to the formation of amorphous rather than crystalline structures, a phenomenon that can be attributed to several factors related to thermodynamic and kinetic processes. In growth techniques such as chemical vapor deposition (CVD), physical vapor deposition (PVD)[13], and growth from solution[14], the deposition rate, process temperature, and environmental conditions may not favour the atomic ordering necessary for crystallization, thus leading to the formation of amorphous phases.

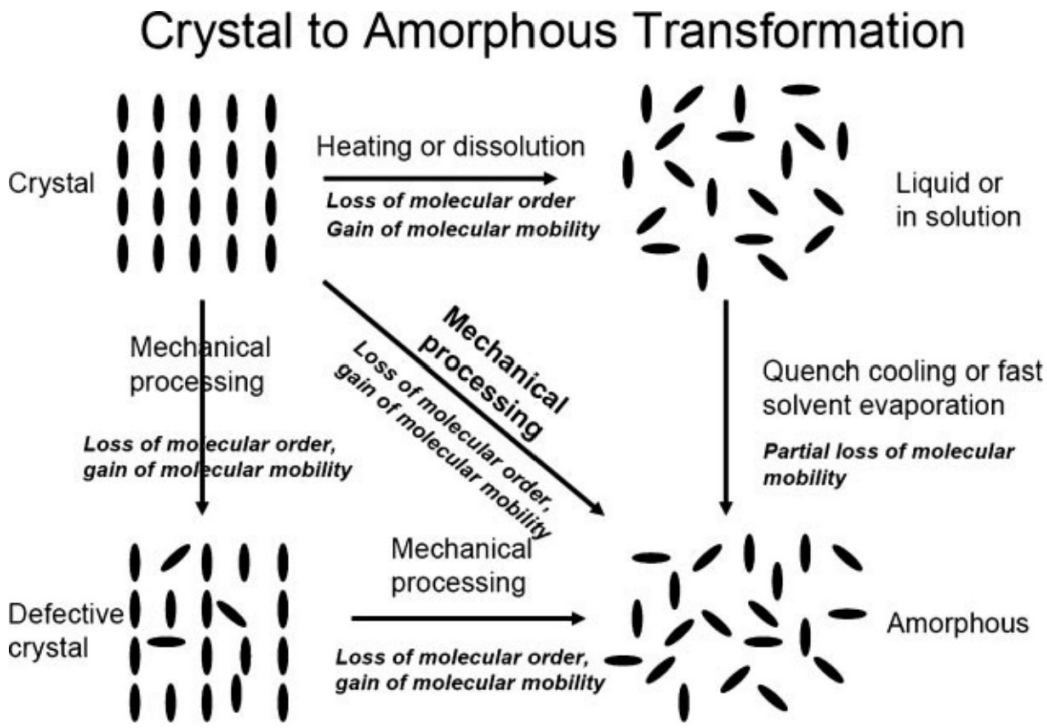

Figure 2.1.1 *Crystal to amorphous transformation, gradually reducing structural order[15].*

Amorphous structures are characterized by long-range disorder in the atomic arrangement, in contrast to crystalline materials that show a defined periodic

order. This disorder can emerge during rapid cooling or under non-equilibrium growth conditions, where the atoms do not have sufficient mobility to organize into a stable crystalline structure.

Crystallization of inorganic materials is a process that requires a high activation energy, which is needed to overcome energy barriers that prevent atomic ordering into a well-defined crystalline structure. This activation energy is often provided through high-temperature calcination processes, a common method in the synthesis of crystalline materials.

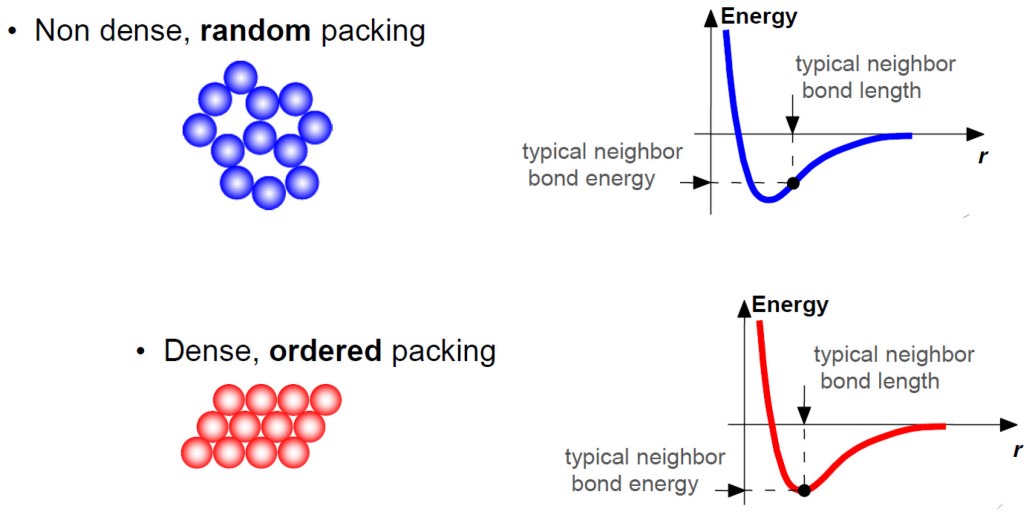

Figure 2.1.2 *Amorphous (top) and crystalline (bottom) materials. Dense, ordered packed structures tend to have lower energies*[16].

Calcination, which involves heating a solid material to high temperatures, induces thermal decomposition, removal of volatiles, and promotion of chemical reactions necessary for the formation of crystalline phases. At these temperatures, atoms gain sufficient kinetic energy to migrate and rearrange into a stable crystal lattice, thereby reducing the free energy of the system. This process is essential in the production of oxides[17], silicates[18], and other ceramic materials[19], where the formation of well-defined crystalline structures is essential to achieving the desired physical and chemical properties.

The activation energy required for crystallization varies depending on the material and process conditions. Materials with strong chemical bonds, such as metal oxides, typically require very high calcination temperatures, even above 1000°C, to reach the crystalline state[20,21]. During calcination, phase transformations can also be accompanied by changes in the mechanical, thermal and optical properties of the material, making precise control of temperature and time conditions fundamental.

The high temperatures required for crystallization can also present practical technological challenges. Materials used in reactors and furnaces must be able to withstand these extreme conditions without degrading, which often requires the use of expensive materials[22] or advanced cooling technologies. In addition, such high temperatures can induce thermal stress in materials, leading to deformations, defects or even promoting the formation of undesirable or metastable phases, further complicating the control over the quality and purity of the final product.

A high activation energy, especially in the industrial sector, means high energy consumption and a large carbon footprint, which are not aligned with greenhouse gas reduction goals and the associated fight against climate change. Therefore, reducing the activation energy of such transformations is a key challenge for the development of more sustainable and cost-effective synthetic processes.

2.1.2 Crystallization catalysts

Catalysis constitutes a good solution to facilitate chemical reactions by lowering the activation energy, the minimum energy required for reactants to convert into products. By providing an alternative reaction pathway with a lower energy barrier, catalysts increase the reaction rate without being consumed in the process. This not only enhances the efficiency of the reaction but also allows it to proceed under milder conditions, such as lower temperatures or pressures, which is advantageous from both an industrial and environmental point of view. The role of catalysis is particularly significant in fields like synthetic chemistry, petrochemistry, biochemistry, and material science, allowing precise control over reaction kinetics.

In biological systems, for instance, enzymes act as natural catalysts, enabling complex biochemical reactions to occur rapidly and selectively under physiological conditions[23]. Similarly, in industrial applications, catalysts are indispensable for optimizing processes such as the synthesis of chemicals, energy production, and environmental protection through emission control[24].

This concept applies not only to traditional chemistry but also to processes such as the crystallization of solid materials. There are, in fact, crystallization catalysts that allow the formation of crystals at lower temperatures or in shorter times.

A method to decrease crystallization temperature is a solid-state process called Metal-Induced Crystallization (MIC) in which a material crystallizes at a lower temperature if in contact with a metal. This process has been used extensively in the semiconductor industry, especially for thin-film deposition, as a solution to achieve crystallization, reducing energy consumption and minimizing thermal stress on substrates[25,26].

In recent decades, a similar effect has been observed in the case of amorphous oxides. Indeed, there is evidence in the literature of metals being used as crystallization catalysts for oxides, in the form of metals in the elemental state[27], as molecular compounds[28], and as metallic cations[29]. However, among these observations the only complete mechanistic study is relative to the work of Yang et al.[27]. They investigated the crystallization of amorphous TiO_2 thin films by introducing metal contact layers, such as Ni, between the TiO_2 film and substrate. The crystallization temperature of TiO_2 was found to be lower than possible without contact with the metal. Since part of the Ni atoms was located on the surface of the crystallized TiO_2 film, they concluded that metal diffuses through the lattice of the amorphous material and proposed a reaction-assisted crystallization model, in which an intermediate complex containing Ti-O and Ni-O bonds decomposes to crystallize TiO_2 at a lower temperature.

The above explanation was later considered valid also in apparently analogous cases, in which a lowering effect on the crystallization temperatures of oxides of amorphous materials was observed when in contact with metals.

Oxides for which the effects of MIC have been studied are various: TiO_2, SiO_2, Al_2O_3, some semiconductor oxides such as ZTO, IGZO, IGO and even cathode materials like $LiCoO_2$.

In particular, for titania MIC enables the formation of anatase and rutile phases at temperatures as low as 150°C (compared to 400°C required for conventional calcination). Studies have shown that various metal cations, like gold, cobalt, and nickel, can act as devitrification agents, influencing not only the crystallization temperature but also the crystalline phase[30]. MIC has also been applied using laser, ultrasound, convective heating, and microwave irradiation[31] to achieve phase transitions, significantly reducing crystallization times and temperatures.

In the case of silica, the results consist of the formation of α-quartz tridymite or cristobalite, depending on the cation used and the crystallization conditions. It has been demonstrated that the morphology of amorphous silica can influence the homogeneity of cation distribution and the resulting crystallization behavior[32]. Lowering the temperature has allowed the production of quartz nanomaterials, preserving complex macro and meso-structures, which are otherwise degraded during high-temperature calcination[33].

It appears clear that MIC is a promising and versatile technique for crystallizing semiconductors and metal oxides at lower temperatures, with application in a wide range of fields, offering both energy savings and preservation of material architectures. Future developments may focus on hybrid materials, low-temperature synthesis on thermally sensitive substrates, and optimization of crystallization processes. To achieve this is fundamental to continue research into the mechanisms underlying it.

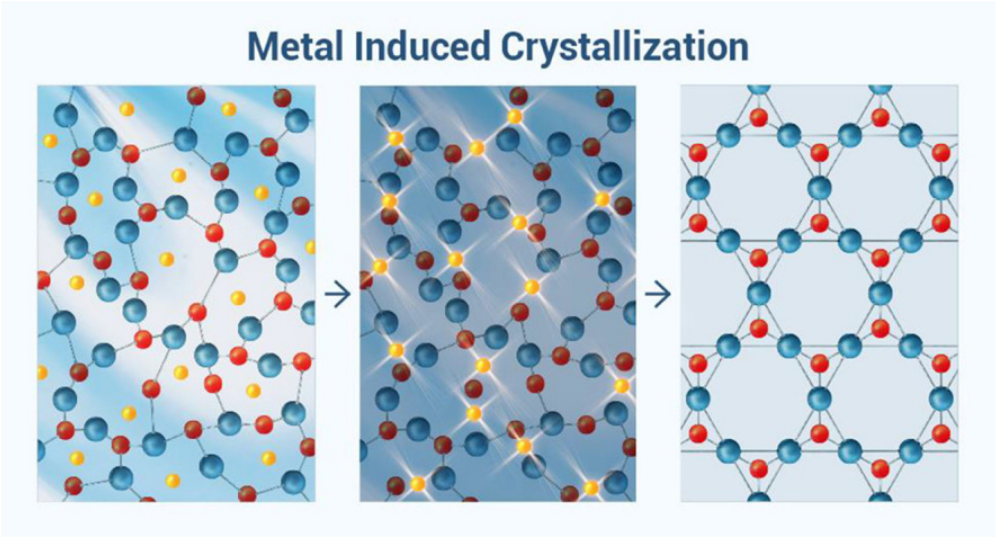

Figure 2.1.3 *Schematic mechanism of MIC, with the transition from amorphous to the crystalline phase, after the addition of metals and thermal treatment.*

As mentioned, the MIC process typically occurs when a metal catalyst is deposited onto an amorphous material like silicon, germanium, or metal oxides like the ones listed above. The interaction with metal facilitates the growth of crystalline phases at temperatures significantly lower than those required for crystallization without the metal presence. It is generally assumed that the metal lowers the activation energy for crystallization, probably by providing a pathway for the diffusion of atoms or by altering the local electronic structure of the material. This process is highly dependent on the selected metal, the type of amorphous material, and the specific conditions under which the MIC is carried out, such as temperature and annealing time.

Studies on the mechanism of MIC believe that the metal diffuses through the oxide structure, temporarily breaking the metal-oxygen bonds and allowing the polyhedra to reorganize and reform bonds with more favourable energy levels, and therefore to crystallize[34,35], without becoming part of the crystal lattice that will form[36]. It is thought that the M−O bond should weaken when a metal cation partially transfers valence electrons to the antibonding orbitals, so that the heat supplied during thermal treatments is then sufficient to break the weakened M−O bonds.

The above explanation, although it may be considered reasonable in the presence of metals in the elemental state or even in the form of cations, may not have a general character. In fact, there are studies that report the catalytic effect obtained by contact of metal halide molecules, which however are too large to diffuse through the solid lattice[28].

It is likely that the precise mechanism by which MIC occurs is not yet fully understood and further investigation is needed. It is essential to continue research into the mechanisms and role of different metals to further expand their applications in science and industry.

The present work aims to take a step in this direction, to study a phenomenon that often sees hypotheses contradicting each other[29,37,38]. Amorphous silica has been selected as a model system on which to test alternative hypotheses on the mechanisms that can lead to this crystallization. Initially, existing literature observations were reproduced, focusing on the use of metal cations. The silica samples were impregnated with solutions of metal compounds and calcinated; then the correlations between the obtained polymorphs and the metal cations used will be analyzed.

2.2 On SiO_2

Silicon dioxide (SiO_2), also known as silica, is a chemical compound which has a fundamental importance in various scientific and industrial domains, such as material science[39], electronics[40], semiconductors[41], and glass manufacturing[42], due to its abundance in nature, and unique physical and chemical properties.

Silicon dioxide makes up about 59% of the Earth's crust by mass, making it the most abundant compound. Its best-known polymorph, quartz, is the second most abundant mineral in the crust after feldspar, making up about 12% of the Earth's crust and playing a major role in geological processes.

The chemical structure of silicon dioxide is characterized by a network of SiO_4 tetrahedra, in which each silicon atom forms covalent bonds with four oxygens, creating a three-dimensional network of high chemical stability. In addition, silica has a highly polymorphic structural behaviour, which leads to different physical characteristics and potential applications in different environmental conditions.

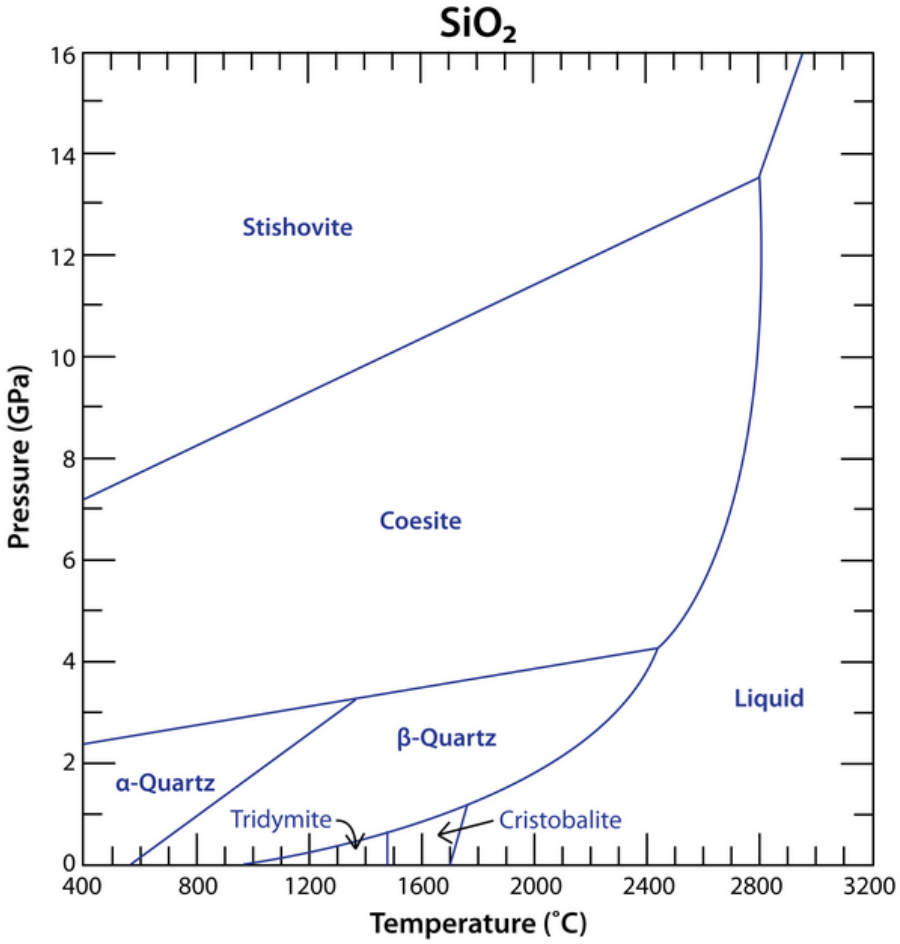

Figure 2.2.1 *Pressure/temperature phase diagram of* SiO_2[43].

SiO_2 occurs in a wide variety of crystalline forms having well-defined lattice structures, visible in the well-known Pressure-Temperature phase diagram reported in Figure 2.2.1. Quartz is the most stable form at ambient conditions, while tridymite and cristobalite are stable at higher temperatures, above 870 and 1470 °C respectively. Coesite and stishovite, other forms of silica, are common at extreme pressures[44], over 2 and 7 GPa respectively, typical of deep crustal and mantle

environments. The transitions between different polymorphs can involve distortive changes of the crystal cell or the complete breaking of bonds followed by their rearrangement. For example, increasing the temperature, quartz first changes from an α phase (low temperature) to a β phase (high temperature), which is a distortive-type transition, and then to other phases through a reconstructive-type transition. It is intuitive that breaking the bonds between Si-O_4 tetrahedra is possible only by providing large amounts of energy, through temperature or pressure. The transformation between these polymorphs is driven by thermodynamic conditions, and the resulting structural changes have direct implications on their physical and chemical characteristics. For instance, quartz exhibits piezoelectric properties, which means the ability of its crystal structure to generate an electric charge when subjected to mechanical stress and it is essential in the production of various technological devices, including semiconductors, telecommunications systems, and precision timing instruments like quartz oscillators, which produce highly stable frequency signals[45].

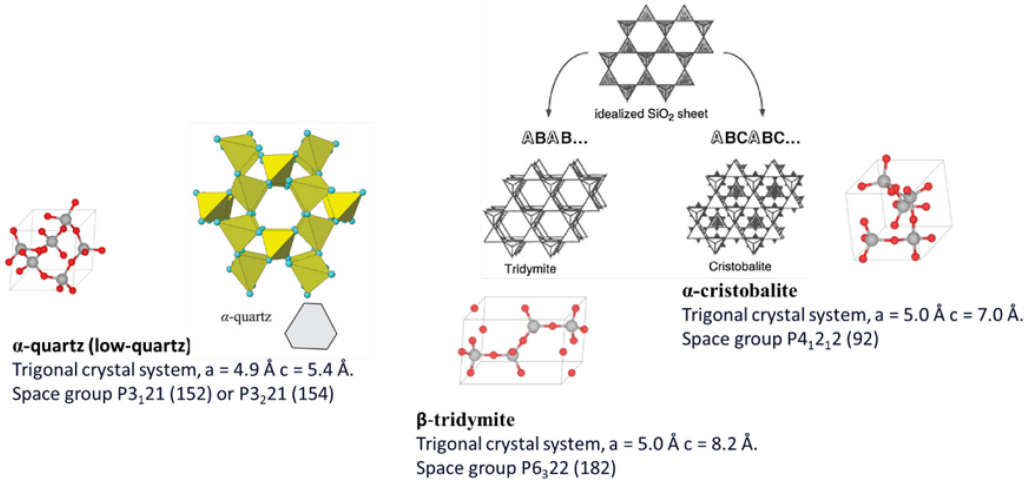

Figure 2.2.2 *Unit cells, cell parameters and space groups of α-quartz, β-tridymite, and α-cristobalite, the three main forms of SiO_2.*

The development of quartz-based technologies accelerated in the late 19th and early 20th centuries, particularly during World War II when quartz crystals became crucial for military communication devices. The demand for high-quality quartz crystals for precision instruments led to extensive research into synthetic

quartz production. One of the earliest breakthroughs in this area occurred in 1909, when Italian engineer and mineralogist Giorgio Spezia pioneered the hydrothermal synthesis of quartz[46]. Spezia's method involved recrystallizing quartz fragments in an autoclave filled with a sodium silicate (Na_2SiO_4) solution. The autoclave was heated on one side and cooled on the other, creating a thermal gradient that facilitated the slow growth of quartz crystals over time. This method laid the groundwork for modern quartz synthesis techniques, which have since evolved to produce synthetic quartz crystals on an industrial scale. Subsequent research by scientists like Walker, Nacken, and Woosters expanded upon Spezia's work, optimizing the hydrothermal process for higher efficiency and better control over crystal growth[47].

The hydrothermal synthesis method remains the most widely used technique for producing synthetic quartz, although other methods have also been explored. For example, quartz nanoparticles, such as Stöber particles, are synthesized using sol-gel processes which involve the hydrolysis of silicon alkoxides in the presence of alcohol and ammonia. These particles have applications in catalysis, drug delivery, and advanced materials[48].

The synthesis and phase behaviour of SiO_2 polymorphs are governed by both thermodynamic and kinetic factors. One challenge in SiO_2 synthesis is the formation of metastable phases at ambient conditions, even when more stable polymorphs are thermodynamically favoured. This phenomenon is consistent with Ostwald's Rule of Stages[49], which states that during phase transitions, a system often passes through intermediate, less stable states before reaching its most stable configuration. For example, cristobalite, a high-temperature phase, may form as a metastable product under ambient conditions if kinetic factors dominate the crystallization process.

Controlling the formation of specific SiO_2 polymorphs is critical for applications where purity and structural integrity are paramount, such as in the semiconductor industry. The SiO_2 phase diagram, which maps the stability of different polymorphs under varying temperature and pressure conditions, serves as a fundamental guide for optimizing synthesis processes. Achieving phase-pure

materials often requires precise control over reaction conditions to avoid the formation of unwanted polymorphs that could compromise material performance. In the present work, it will be shown the study of amorphous SiO_2 crystallization induced by metals exploring the possible tunability of temperature phase transitions (i.e. activation energies) at ambient pressure, thus focusing on quartz, cristobalite and tridymite polymorphs.

2.3 Materials and methods

In the experimental framework, many SiO_2 crystallization attempts have been made in order to investigate in detail MIC driving mechanisms and observe its dependence on key parameters and treatment conditions.

After the evaluation of possible different behaviour of MIC starting from commercial amorphous SiO_2 with respect to synthesized amorphous SiO_2 via sol-gel methods, silica has been impregnated with salt solutions of several alkali and alkaline-earth chlorides or nitrates. In this way, different valence states (fixed to +1 for alkali and +2 for alkaline-earth elements) and ionic radii (from 0.76 Å of Li to 1.74 Å of Cs) of elements have been considered as possibly affecting parameters of MIC, as well as electronegativity character and so on. The salts' solubility has been considered in the choice of tested salts, allowing to compare the results by keeping constant the salt (thus the metal cation source) concentration during the analysis. Further analyses have been performed on halogen salts of potassium (from KF to KI), showing the effect of the anionic counterpart in MIC by keeping the same cation. The impregnated amorphous SiO_2 with salt solutions have been dried at air ambient conditions.

After this preparation, various calcination treatments were conducted on amorphous SiO_2 impregnated with salt in a furnace. The powders were inserted into an alumina crucible, closed with the relative cap, and the treatments have been carried out by varying the target temperature, the duration of treatment, and the cooling ramp.

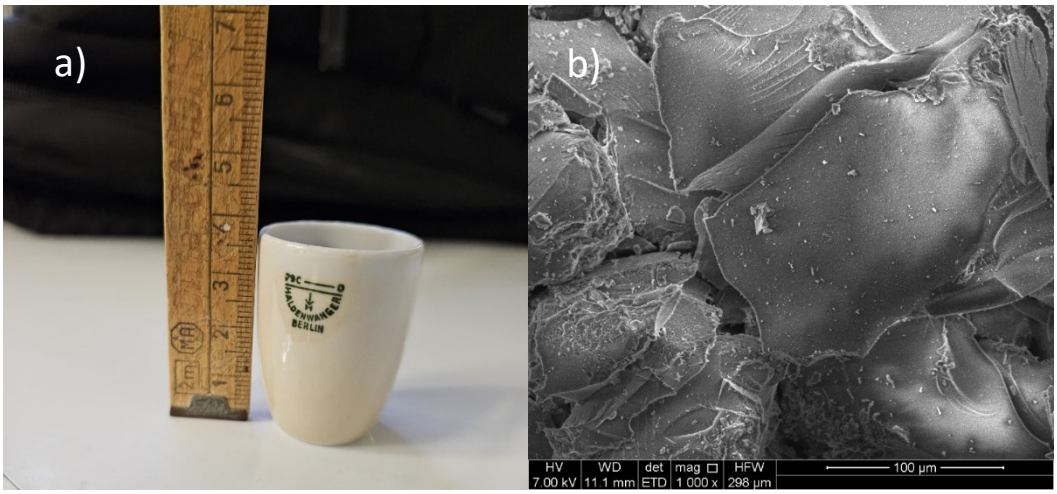

Figure 2.3.1 *a) An alumina crucible used for thermal treatment and b) the starting SiO_2 viewed with scanning electron microscope.*

Unless otherwise specified, the experimental results presented below refer to cooling ramps based on the thermal inertia of the furnace, characterized by an initial rapid cooling rate followed by a gradual slowdown as the temperature approaches room temperature (around 8 hours overall). The heating ramp has been fixed for all the treatment to 3°C/min.

2.3.1 The starting amorphous SiO_2

To explore a wide range of possible parameters which are involved during the MIC process, the contribution of the starting amorphous silica has been evaluated by performing MIC experiments both on a commercial amorphous SiO_2 (MP EcoChrom^{TM} 63-200, particle size 100-200 µm) and a synthesized one via sol-gel method.

The sol-gel process consists of a sequence of chemical and physical transformations through which, starting from a solution of liquid precursors, a solid network is generated. The sol-gel process allows obtaining a wide variety of products (including films, powders, fibres, porous gels, and membranes) with variable shapes, sizes, and porosities using a simple technique that can be applied

at room temperature, with reduced costs and short processing times[50–52]. The transformation from liquid to solid proceeds through the sol and gel states. The sol is a colloidal solution which aggregates to form the gel, a three-dimensional polar amorphous network containing the liquid phase. When the liquid phase evaporates, the structure collapses and a solid known as xerogel is obtained, whereas if the solvent is removed under supercritical conditions, the network retains its morphology, and the resulting polymer is an aerogel, characterized by lower density.

The precursors used in the sol-gel process consist of metals surrounded by reactive groups, generally alkoxides, which donate electron density to the metal, increasing its nucleophilic character. Among the metallic alkoxides $M(OR)_n$, the most used are silicon-based ones such as $Si(OR)_4$, and in particular tetraethoxysilane (tetraethyl orthosilicate TEOS) and tetramethoxysilane (tetramethyl orthosilicate TMOS, as shown in Figure 2.3.2).

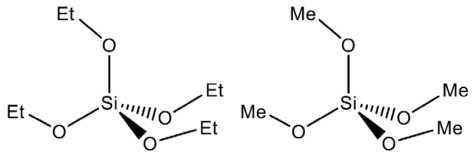

Figure 2.3.2 *Molecules of tetraethoxysilane (left) and tetramethoxysilane (right), better known as TEOS (from tetraethyl orthosilicate) and TMOS (from tetramethyl orthosilicate).*

Some alkoxides are not water-soluble, and to achieve a single phase, it is necessary to add solvents, usually alcohols, which homogenize the precursors.

The sol-gel process can be divided into the following steps:

- *Hydrolysis and condensation sequence*. The liquid precursor is hydrolyzed by water. One or more alkoxide groups -OR are transformed into hydroxyl groups -OH.

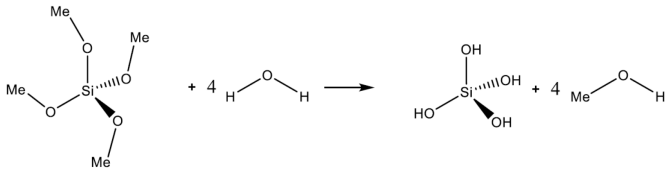

Figure 2.3.3 *Hydrolysis reaction on the silicon atom, the RO- groups are transformed into HO-groups.*

The hydrolyzed precursors condense with each other, forming a network of siloxane bonds Si-O-Si, which contains water and alcohol in its pores, eliminated during the reaction.

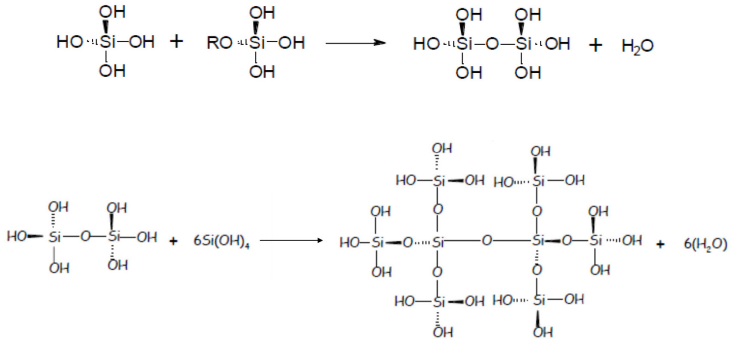

Figure 2.3.4 *Condensation with the formation of a network of Si-O-Si.*

The reaction kinetics are very slow and can be accelerated by using a catalyst, which can be acidic, basic, or fluoride-based.

- *Gelation*. A porous three-dimensional network is created through the aggregation of colloidal particles and condensed silica species. The characteristics of the resulting gel depend on the particle size and the degree of branching before gelation. Viscosity increases over time, slowly at first, until it reaches an asymptotic trend. At this point, called gelation, the fluid solution becomes an elastic solid.

- *Aging*.

- *Drying*. The liquid is removed from the network, which can cause structural inhomogeneities leading to gel fracturing. At the end of the drying process, a xerogel is obtained.

The structure of the gel and its properties are mainly determined during the hydrolysis and condensation phases. The factors influencing them are numerous, such as type of precursors, pH, temperature, reaction time, reagent concentration, nature and concentration of catalysts, type of solvent, the ratio between reagents and water, aging time, and temperature.

In this work, the reagents employed for the sol-gel synthesis of silica are reported in Table 2.3.1. A considerable batch of material was prepared to standardize the starting product.

Sol Gel Formula (60 mL Vtot)		
Precursor	TEOS (Tetraethyl-orthosilicate)	13 mL
Solvent	EtOH (Ethanol)	38 mL
Catalyst	NH_4F 1% sol	1 mL
	H_20	8 mL

Table 2.3.1 *Sol Gel Formula for the preparation of starting amorphous silica.*

Figure 2.3.5 *Batch of sol-gel silica. A considerable reduction in volume can be observed after drying.*

By performing calcination treatments at these conditions on samples impregnated with different salt solutions as a source of metallic cation for MIC,

commercial and sol-gel synthesized SiO_2 exhibited analogous crystallization results. Particularly the same added salt led to equal SiO_2 polymorph and, in case of coexistence of more than one phase, the volume ratio of the two polymorphs, calculated by Rietveld refinement analyses, was consistent between the commercial and sol-gel SiO_2. For this reason, the experimental results, which provide a detailed analysis of the parameters involved and their influence on MIC and are presented later in this thesis rather than discussed here, refer exclusively to commercial SiO_2 to ensure better reproducibility of the preparations. The compatibility of the crystallization products obtained via MIC from the two starting SiO_2 materials is likely related to their similar porosity and/or particle size, fundamental parameters to allow diffusion processes and atomic rearrangement in a new crystalline phase. To support this hypothesis, a more in-depth study of the two SiO_2 samples using Brunauer–Emmett–Teller (BET) analysis is planned, with comparable results expected. Both commercial and sol-gel synthesized SiO_2 did not display any transformation from amorphous to crystalline phase by keeping the same calcination conditions with no addition of salts to induce MIC. As a demonstration, in Figure 2.3.6 the PXRD pattern from calcinated commercial SiO_2 at 1000°C for 4 hours is reported, highlighting the characteristic broad peak proper of non-crystalline materials. On the contrary, in Paragraph 2.4, many examples of crystalline SiO_2 samples obtained by MIC, resulting in very different diffraction patterns from the one reported in Figure 2.3.6, will be shown.

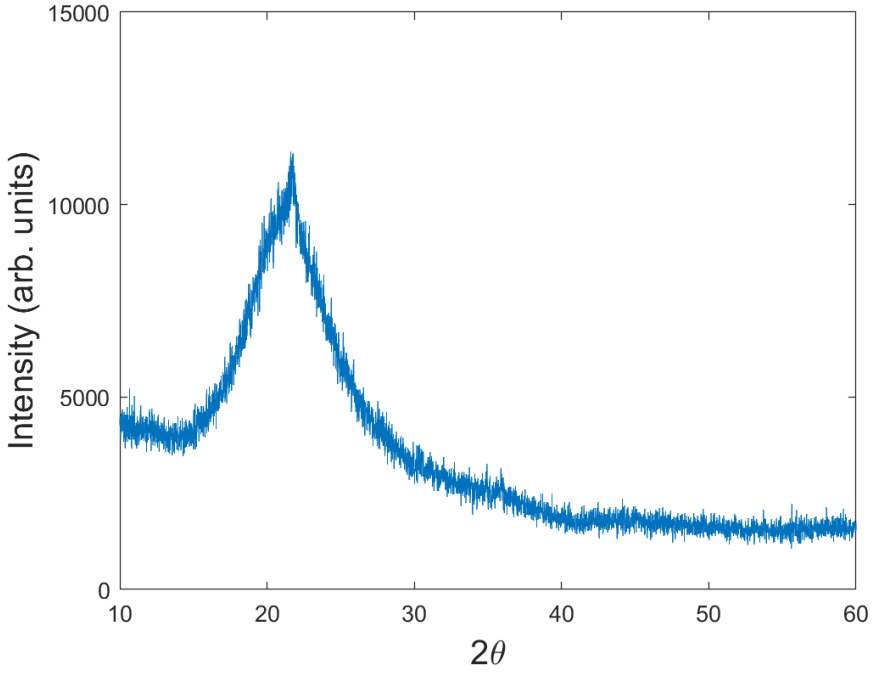

Figure 2.3.6 *PXRD pattern from calcinated commercial SiO_2 at 1000°C for 4 hours without salt impregnation.*

2.3.2 Salts as metallic cation source

Several nitrate and chloride salts from alkali and alkaline-earth elements have been selected as metallic cation sources for MIC. Specifically, $LiNO_3$, $NaNO_3$, KNO_3, $RbNO_3$, and $CsNO_3$ have been employed as sources of +1 oxidation state metals, while $Mg(NO_3)_2$, and $Ca(NO_3)_2$ as donors of +2 valence metals. Correspondingly, LiCl, NaCl, KCl, RbCl, CsCl, $MgCl_2$ and $CaCl_2$ have been used to investigate possible different MIC driving mechanisms related to the anionic counterpart of salts. The salts mentioned above are readily available in most laboratories, relatively inexpensive, and exhibit good solubility. These characteristics make them promising candidates as metal sources for MIC, particularly in terms of practical applicability for large-scale processes.

Tables 2.3.2 and 2.3.3 show the melting point and boiling point of the selected salts for MIC of SiO_2. For the calcination attempts, an intermediate temperature between T melting and T boiling of chlorides has been selected in order to favour the contact area with SiO_2 powder, by performing treatments at 1000°C.

This target temperature has been kept constant also in the case of nitrates, thermal regime in which they decompose.

	T melting (°C)	***T boiling (°C)***
LiCl	610	1382
NaCl	800	1465
KCl	770	1420
RbCl	718	1390
CsCl	646	1297
$MgCl_2$	714	1412
$CaCl_2$	775	1935

Table 2.3.2 *Melting and boiling points of the selected chlorides (anhydrous form) for MIC of SiO_2[53]*

	T melting (°C)	***T decomposition (°C)***
$LiNO_3$	255	600
$NaNO_3$	308	380
KNO_3	334	400
$RbNO_3$	310	310
$CsNO_3$	414	414
$Mg(NO_3)_2$	129	330
$Ca(NO_3)_2$	560	560

Table 2.3.3 *Melting point and decomposition temperature of the selected nitrates (anhydrous form) for MIC of SiO_2[53]. For some nitrates, the decomposition process starts at the melting temperature.*

According to the solubility allowed by each salt, the first explored salt solution concentration has been fixed to 1 mol/L in distilled water. In this way, the molar ratio between the salt and SiO_2 is calculated to be around 1:17. Considering the molar mass of the considered salts, the mass percentage of salts concerning the total mass of salts and silica ranges between 4% (of the lighter LiCl) and 14% (of the heavier CsCl).

2.3.3 X-rays Powder Diffraction (PXRD)

The samples obtained have been characterized in their structural properties by X-rays Powder Diffraction (PXRD). Powder Diffraction (PD) is one of the most important methods to investigate the structural, and even morphological, properties of crystalline solid materials, especially when single crystals cannot be employed. Namely, PD is nowadays a standard technique for compositional and microstructural analyses, such as for the detection of crystalline phases in mixed composition samples, with the possibility to perform quantitative analysis to evaluate the volume fractions of each component. The structural information enclosed within the diffraction pattern is the result of the scattering process between a specific probe, characterized by a wavelength comparable with the interatomic distances, and the crystal lattice of the large number.

Powder X-rays diffraction experiments reported later on have been performed on a Rigaku Smartlab XE diffractometer, available at the Department of Chemistry, Life-Science, and Environmental Sustainability of the University of Parma. The instrument works in the Bragg-Brentano geometry, making use of Cu Kα wavelength ($\lambda = 1.5406$ Å). For standard acquisitions, a Ni filter is used to suppress the K_β contribution, while Soller slits (commonly 5.0°) are used both on the incident and diffracted beam, whose signal is collected using a HyPix3000 detector, acquiring in continuous 1D mode.

In situ PXRD measurements as a function of temperature have been conducted on Empyrean diffractometer (Malvern Panalytical), available at the Department of Applied Science and Technology (DISAT) of Politecnico di Torino.

The system is equipped with a High-Temperature Oven Chamber HTK 1200N (Anton Paar), which allows studies in different atmospheres from room temperature up to 1200 °C.

In general, a monochromatic X-ray beam undergoes a diffraction process with the crystal lattice of the crystallites, describable by Bragg's law:

$$\lambda = 2d_{hkl} \sin \theta_{hkl} \quad (1)$$

Where a series of crystallographic d-spacing, associated with a particular set of Miller indices (hkl), can be measured by moving the detector at different angular positions. The recorded diffraction pattern contains information regarding:

- the unit cell symmetry and size from the peak positions;
- the atomic distribution in the unit cell from the peak intensities;
- the particle size and defects from the peak shapes;
- the diffuse scattering of matrix or amorphous phases, as well as the sample holder, from the background.

In the case of amorphous materials, characterized by a lack of long-range atomic ordering and an intrinsic disorder, it is difficult to extract structural information from PXRD data. Instead, complementary local techniques, such as Nuclear Magnetic Resonance or absorption spectroscopies, could be more effective.

PXRD data reported in the Experimental part have been analysed with GSAS-II[54] software mainly to perform quantitative determination of phase fractions and cell parameters.

2.3.4 Scanning Electron Microscopy

Scanning Electron Microscopy (SEM) has been employed to investigate the morphology and composition of the samples in the powder form. The SEM microscope employed, available at the Chemistry Department of the University of

Parma, is the ESEM Quanta 250 FEG by FEI part of Thermo Fischer Scientific, with relative EDS system by Bruker XFlash 6/30 and Esprit 1.9 software.

SEM uses a beam of electrons, generated from an electron gun (usually a thermionic emitter like a tungsten filament) and accelerated toward the sample by a series of electromagnetic lenses that focus the beam into a fine spot in a vacuum chamber. The focused electron beam scans across the surface of the sample in a raster pattern. As the electrons interact with the sample, various signals are emitted, including secondary electrons, backscattered electrons, and characteristic X-rays. These signals are detected and used to create an image or to determine the elemental composition of the sample in the Energy-Dispersive X-ray spectroscopy (EDS) mode.

2.3.5 Infrared spectroscopy

Infrared (IR) spectroscopy is an analytical technique in molecular characterization, that provides insights into the vibrational modes of chemical bonds within a sample. The technique operates by exposing a sample to infrared radiation (wavelengths ranging from about 700 nm to 1 mm), wherein specific wavelengths are absorbed based on the vibrational frequencies of the molecule's bonds, leading to a distinctive absorption spectrum. These vibrations, which primarily involve stretching (change in bond length) and bending (change in bond angle) motions of covalent bonds, are sensitive to the masses of the atoms involved and the bond strength, making IR spectroscopy a powerful method for identifying functional groups. The resulting spectrum typically represented as a plot of transmittance or absorbance versus wavenumber (cm^{-1}), reveals characteristic peaks that correspond to specific bond vibrations.

For the measurements reported in this work, the instrument used was the Perkin-Elmer FT-IR Spectrum Two spectrophotometer, available in the laboratories of the University of Parma, which allows irradiating the sample at wavelengths corresponding to the infrared range (400-4000 cm^{-1}), using it in attenuated total reflection mode (ATR).

2.3.6 Thermogravimetric analysis

Thermogravimetric analysis (TGA) is an analytical technique used to study the thermal stability and decomposition behaviour of materials by monitoring the mass change of the sample as it is heated in a controlled environment. By analysing weight loss at specific temperature intervals, TGA can identify processes such as dehydration, decomposition, oxidation, and reduction. The key advantages of TGA include its high sensitivity, ability to provide quantitative data on compositional changes, and its applicability in determining kinetic parameters, such as activation energy for thermally induced processes.

The instrument used for the analyses is the TGA 8000 by Perkin-Elmer from the Department of Chemistry at the University of Parma, capable of operating from sub-ambient temperatures up to 900°C.

2.3.7 Inductively coupled mass spectroscopy

Inductively Coupled Plasma (ICP) Spectroscopy is an advanced analytical technique used to detect and quantify elements within chemical samples. The process involves ionizing the sample with a high-temperature plasma, typically generated using argon gas. Argon is ionized by an electromagnetic coil and a Tesla unit, producing a plasma “fireball” with free electrons and argon ions. The sample, usually in aerosol form, is introduced into the plasma's cooler central channel, where it vaporizes, dissociates, and ionizes. These ions are then analyzed spectroscopically to determine elemental composition.

The plasma's temperature is optimized to ionize atoms efficiently, maximizing the detection of elements with high first ionization energies while minimizing excessive ionization for elements with low second ionization energies.

ICP can detect a wide range of chemical elements, including most metals and certain non-metals. For aerosolization, the sample must be in solution, and solid samples require prior solubilization. Silica, the subject of this study, is inert to most solvents. While hydrofluoric acid (HF) can dissolve silica, it is corrosive to

instrumental components. Therefore, a washing procedure using nitric acid (HNO_3) and hydrogen peroxide (H_2O_2) was applied, which does not dissolve silica but effectively solubilizes other compounds in the sample, allowing them to be detected through the analysis.

The instrument used, available at the Department of Chemistry, is an atomic emission spectroscopy (AES), a type of ICP spectroscopy that is based on excited ions releasing electromagnetic radiation at wavelengths specific to a particular element.

2.4 Experimental results and discussion

2.4.1 Structural analysis of calcinated amorphous SiO_2 with alkali salts

PXRD measurements on amorphous SiO_2 treated with alkali chlorides are reported in Figure 2.4.1. As clearly visible from the reference patterns reported for α-quartz (COD code 9012600), tridymite (COD code 5910147), and cristobalite (ICSD code 75300), all the calcinated samples crystallize in one or a mixture of two of these SiO_2 polymorphs. Despite the non-negligible mass percentage of salts added in the samples, which should be clearly detected by PXRD, the diffractograms does not display any reflection peak compatible with the starting salt in crystalline phase for all the measured samples. Only in the SiO_2-CsCl system a weight fraction of 1.8% has been calculated from Rietveld refinement, which is however very far from the expected value of added salt about 14% wt. The lack of crystalline salts contribution to PXRD patterns could be related to a phase transformation during the calcination treatment to an amorphous state, non-visible with PXRD due to the absence of a long-range atomic arrangement. The possibility to have a disordered phase is consistent considering the target temperature for calcination treatments, thermal condition in which the salts are in their liquid phase. However, an amorphous phase quantitatively present in 4-14% weight percentage (i.e. totally related to the salt amount) should probably contribute more to the patterns background of Figure 2.4.1, despite its presence is visible as a broad

asymmetric peak around 21°, especially for the heavier elements. From PXRD patterns, no silicates seem to be formed during the treatments, excluding a chemical reaction between salt and silica. However, few reflections have not been indexed and may belong to silicon dioxide compounds characterized by off-stoichiometry values or different crystallographic systems. Particularly, the main non-indexed peaks, visible at 2-theta angles about 21°, 27°, and 38°, could be attributed to an orthorhombic SiO_2 (COD 9006301), but, for its uncertainty, this phase has not been considered in the following quantitative analysis.

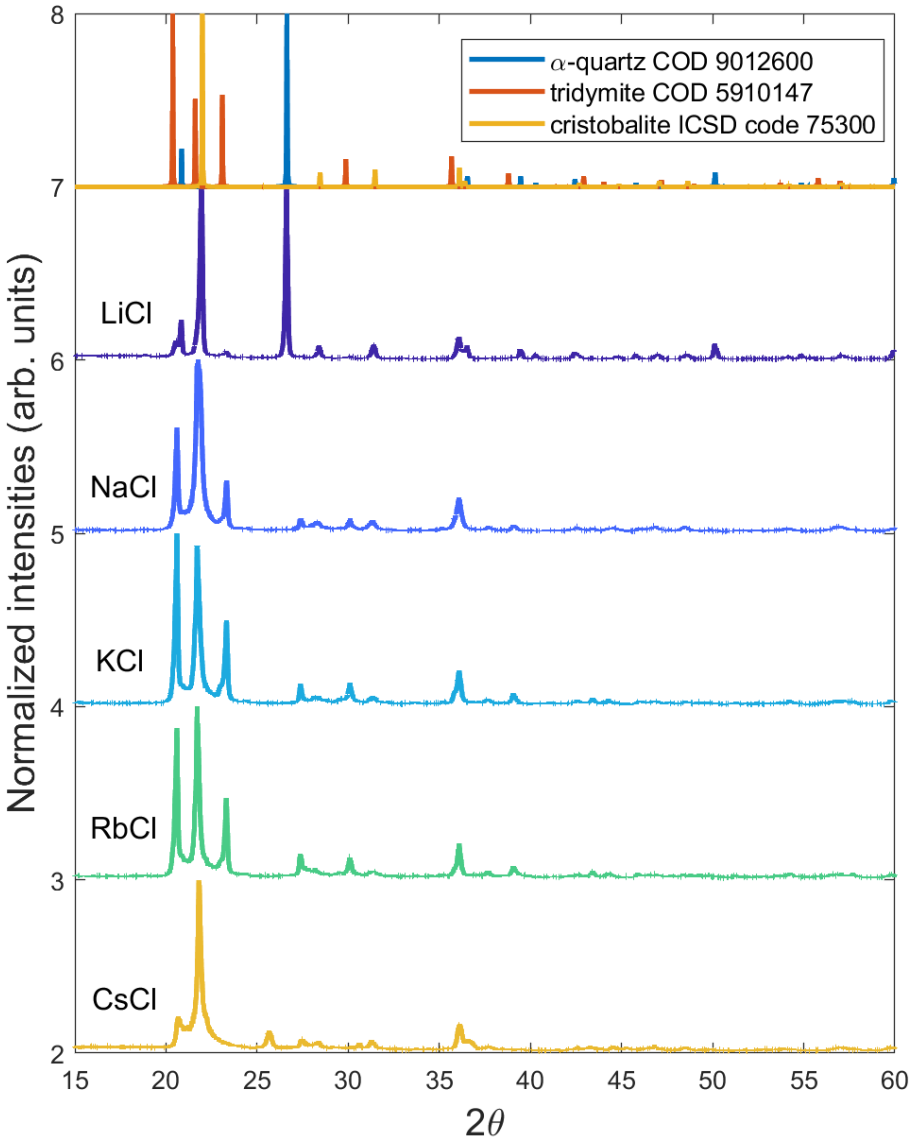

Figure 2.4.1 *PXRD patterns of calcinated SiO_2 with different chlorides at 1000°C-4h. Top: reference patterns for α-quartz, tridymite, and cristobalite.*

Despite the partial indexing of the diffraction peaks, Rietveld refinement of the experimental data has been carried out to estimate the lattice parameters and the quantitative amount of SiO_2 polymorphs. The amorphous contribution has been modelled as a background peak during the refinement process. The fit quality is significantly affected by this approximation and results in quite high values for R_{wp}, around 20 for the whole dataset. Nevertheless, the information obtained by Rietveld refinements represent a qualitative analysis of the crystallized SiO_2 samples by MIC. Particularly, in Figure 2.4.2 the contribution of the detected polymorphs as weight fraction percentage values is shown for each of the salts employed. Quartz is present in a significant amount only in SiO_2 treated with LiCl, while for the other alkali chlorides a mixture of tridymite and cristobalite occurs. CsCl seems to favour silica crystallization in its cristobalite polymorph, reaching 87% weight fraction. No particular trend of the relative cristobalite/tridymite amount is observed from LiCl to CsCl.

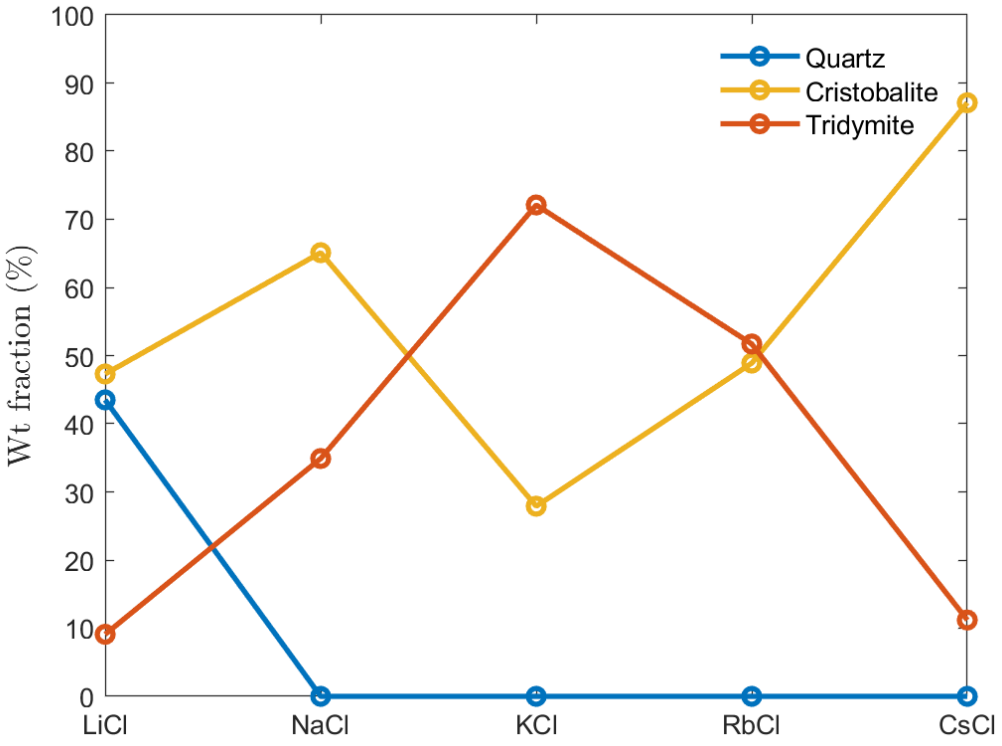

Figure 2.4.2 *Weight fraction percentage values for α-quartz (blue), cristobalite (yellow), and tridymite (red) polymorphs detected in SiO_2 calcinated with different alkali chlorides.*

In Figure 2.4.3 *a* and *c* lattice parameters calculated from Rietveld refinement of both tridymite (a-b) and cristobalite (a-c) phases are reported for all the considered alkali chlorides. Although these results are affected by a certain error degree equal for all the refinements due to the amorphous contribution, not perfectly modelled by a background peak, they suggest that the calcinated SiO_2-salt system crystallizes mainly in a mixture of tridymite and cristobalite polymorphs whose cell parameters seems to be influenced by the kind of alkali metal employed.

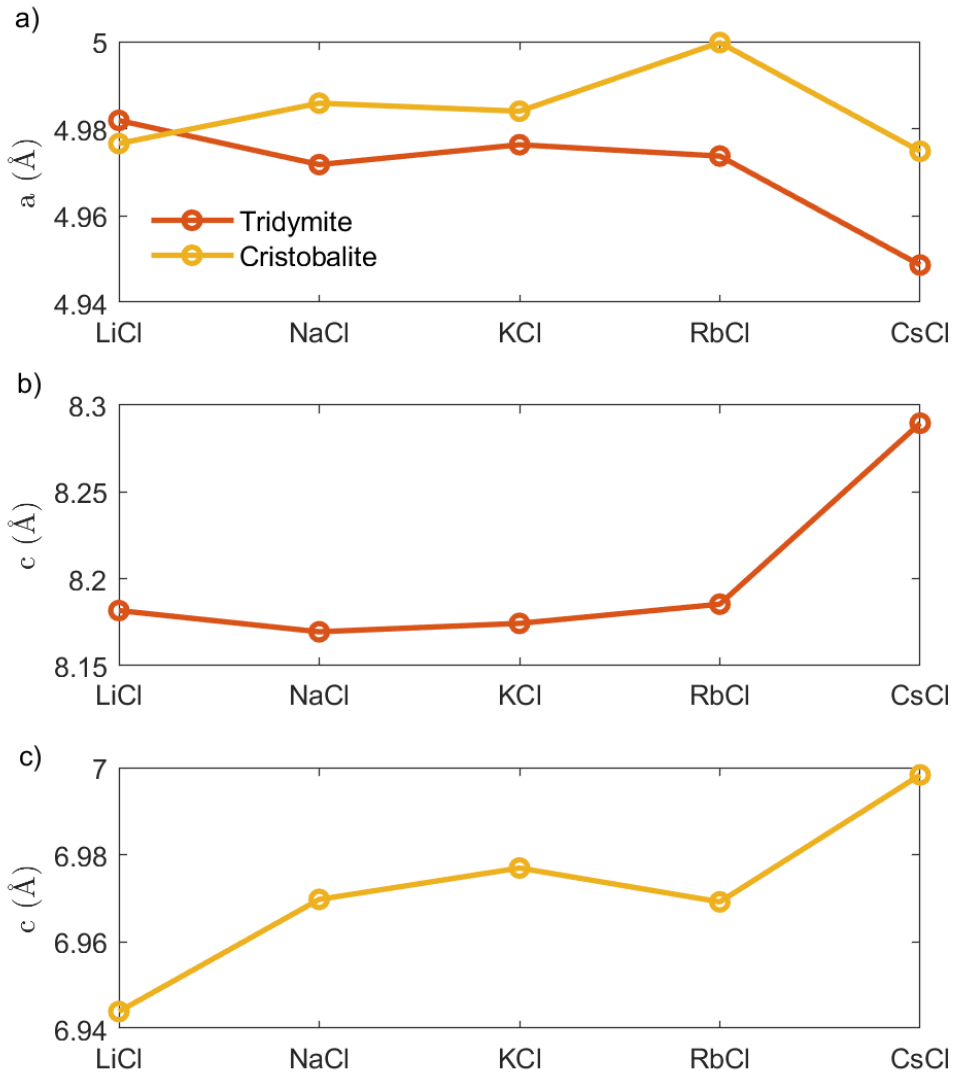

Figure 2.4.3 *Lattice constants trend of both tridymite (a (a) and c (b) parameters, red dots) and cristobalite (a (a) and c (c) parameters yellow dots) phases refined for each alkali chloride used for SiO_2 crystallization.*

Specifically, along the *a* direction tridymite crystal structure displays a slight contraction from LiCl to CsCl, of about 0.03 Å, while no variations have been

calculated for cristobalite *a* constant. A more significant deviation is reported for *c* lattice parameters, which exhibit an increase of its value from LiCl to CsCl for both tridymite and cristobalite polymorphs, around 0.1 Å and 0.06 Å respectively. By considering the different chemical properties of the alkali series Li-Cs, these results suggest that the increase of the ionic radius and/or the decrease of electronegativity and the electronic affinity of the chlorides' metal cation are linked to volume changes observed in the crystallized SiO_2 polymorphs.

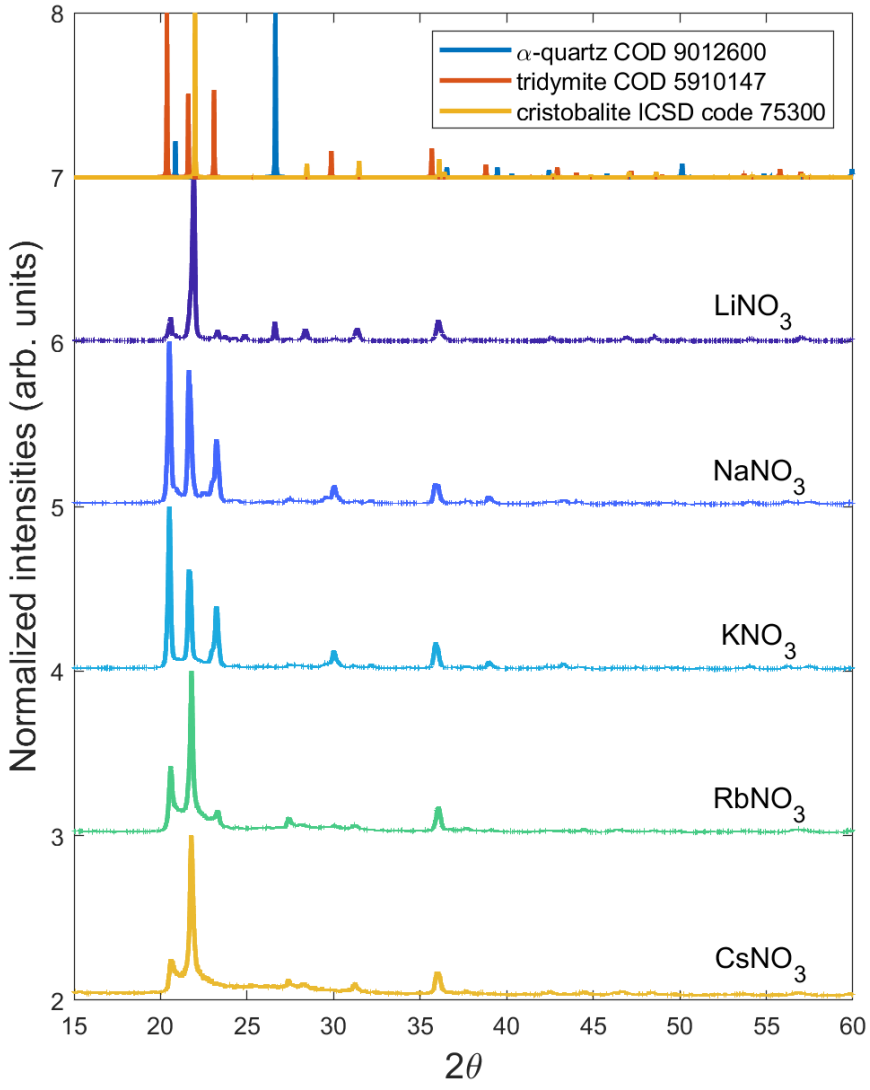

Figure 2.4.4 *PXRD patterns of calcinated SiO_2 with different nitrates at 1000°C-4h. Top: reference patterns for α-quartz, tridymite, and cristobalite.*

PXRD measurements on SiO_2 treated with alkali nitrates are reported in Figure 2.4.4. In analogy with the previously presented results on chlorides, all the calcinated samples crystallize in one or a mixture of two/three of SiO_2 polymorphs among α-quartz, tridymite, and cristobalite. As for chlorides, Rietveld refinement of the experimental data has been carried out to estimate the cell parameters and a quantitative analysis of SiO_2 polymorphs, with resulting R_{wp} values around 15 for the whole dataset.

The diffractograms does not display any reflection peak compatible with the starting salt in crystalline phase for all the measured samples. It is known that nitrate radical NO_3 can decompose thermally (see Table 2.3.3), depending on the environment, producing nitrogen dioxide NO_2. Following this consideration, alkali oxides as a decomposition product could also be present during the calcination process. However, these compounds are not visible in a crystalline form in PXRD patterns.

A small quantity of silicates has been detected for lithium ($Li_2O_5Si_2$, COD 2003027), sodium (Na_2O_3Si, COD 2310858), and potassium ($K_6O_7Si_2$, COD 8103706), respectively around 7.4% wt, 1% wt, and 3% wt. On the contrary, for heavier cations no silicates characteristic reflections have been indexed, while the amorphous content, again modelled with a background peak in the refinement process, seems to be present in a larger amount than in the case light element salts. This disordered contribution is clearly visible as a broad peak in the patterns below tridymite and cristobalite main peaks, especially for silica treated with $RbNO_3$ and $CsNO_3$.

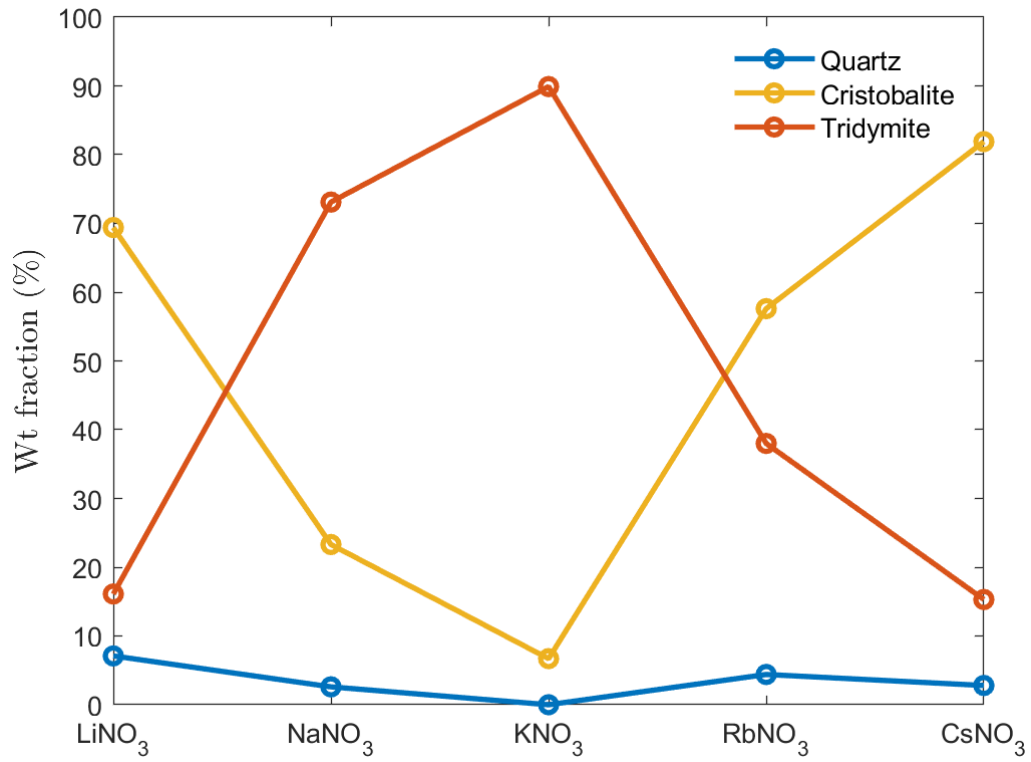

Figure 2.4.5 *Weight fraction percentage values for α-quartz (blue), cristobalite (yellow), and tridymite (red) polymorphs detected in SiO_2 calcinated with different alkali nitrates.*

In Figure 2.4.5 the weight fraction percentage values of the detected silica polymorphs are shown for each of the nitrate employed. Quartz crystallization seems not to be favoured during the calcination treatment, reaching its maximum quantity of around 7% wt in $LiNO_3$, while for the other alkali nitrates a mixture of tridymite and cristobalite occurs as in the case of chloride salts. Despite the small presence of silicates, KNO_3 promotes the formation of tridymite, achieving a 90% of weight fraction. Again, no particular trend of the relative cristobalite/tridymite amount is observed from $LiNO_3$ to $CsNO_3$ along the series.

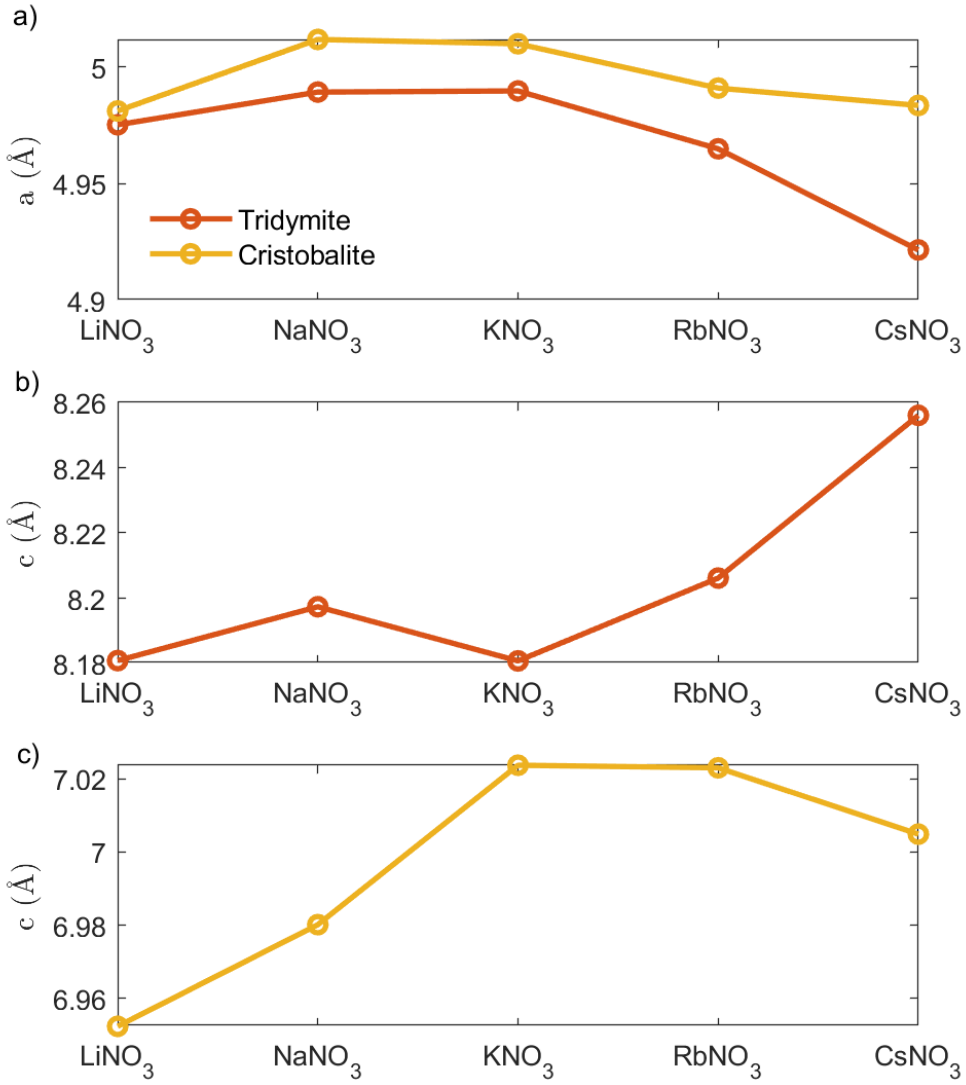

Figure 2.4.6 *Lattice constants trend of both tridymite (a (a) and c (b) parameters, red dots) and cristobalite (a (a) and c (c) parameters yellow dots) phases refined for each alkali nitrates used for SiO2 crystallization.*

In Figure 2.4.6 *a* and *c* lattice parameters calculated from Rietveld refinement of both tridymite (a-b) and cristobalite (a-c) phases are reported for all the considered alkali nitrates. Herein, quartz results have been excluded since they refer to a very low phase amount (i.e. only one or two peaks ascribable to this polymorph are clearly visible in the patterns) and are thus characterized by a low reliability. The trend of these lattice constants by varying the alkali nitrate is very similar to the previously reported one from the respective chloride. Particularly, *a* lattice parameter of tridymite crystal structure slightly decrease from $LiNO_3$ to

$CsNO_3$, of about 0.04 Å, while no differences are evidenced for cristobalite *a* constant, near 5 Å for the whole dataset.

A more significant deviation is reported for *c* lattice parameters, which exhibit an increase of its value from $LiNO_3$ to $CsNO_3$ for both tridymite and cristobalite polymorphs, around 0.08 Å and 0.07 Å respectively. These values are comparable with the one previously calculated for SiO_2-alkali chlorides calcination, suggesting again an increased cell elongation along the c axis for tridymite and cristobalite structures by increasing the ionic radii of the alkali series.

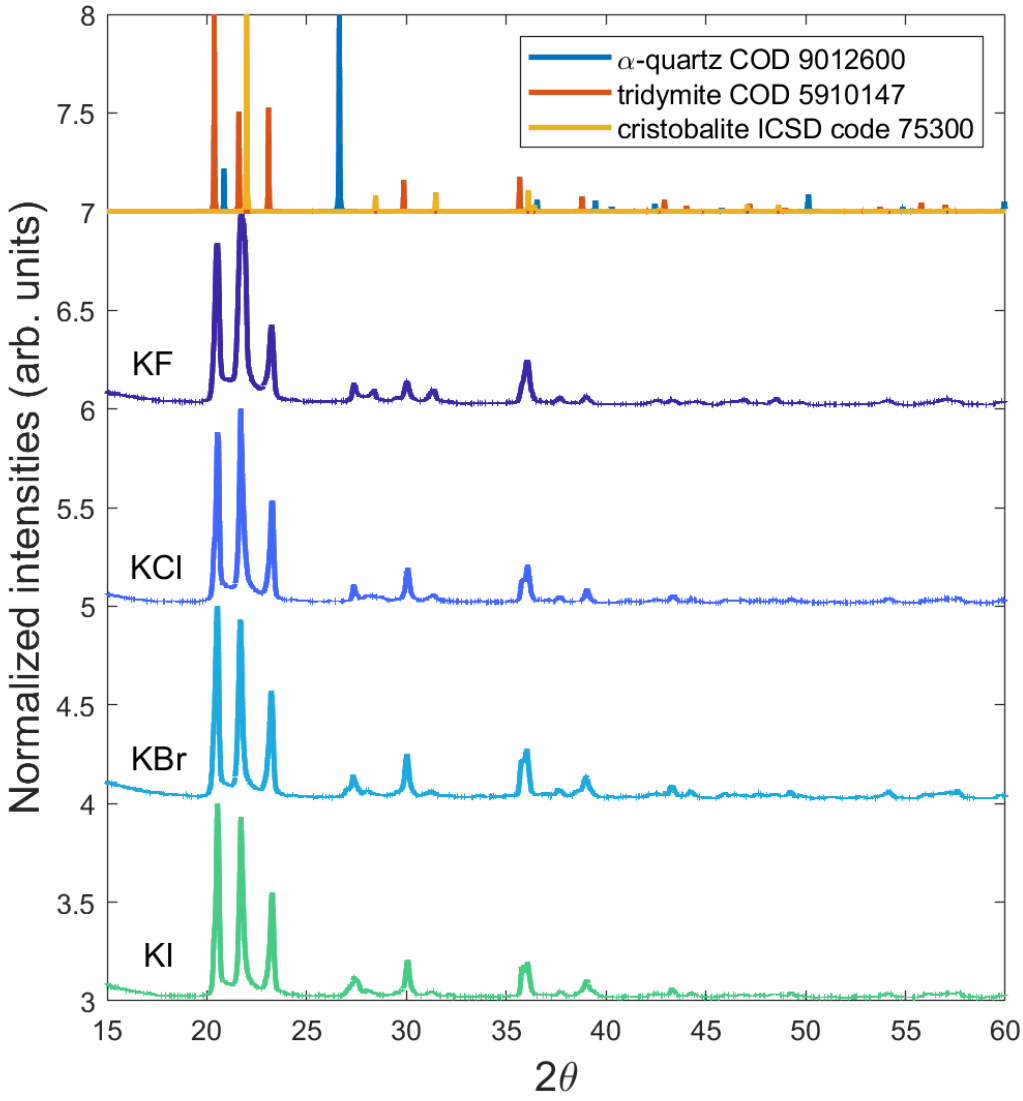

Figure 2.4.7 *PXRD patterns of calcinated SiO_2 with different potassium salts at 1000°C-4h. Top: reference patterns for α-quartz, tridymite, and cristobalite.*

The analogous results obtained on alkali chlorides and alkali nitrates underline the predominant contribution of metal cations instead of the anionic counterparts on SiO_2 crystallization, as reported in literature examples on MIC processes. To emphasize more this prominent effect, further calcination treatments have been carried out with impregnation of KF, KCl, KBr, and KI, thus fixing potassium as metal source while varying the associated anion. The PXRD patterns of calcinated silica with the above-mentioned salts are shown in Figure 2.4.7. The diffractograms are very similar to each other. In fact, in all the samples tridymite, cristobalite and quartz polymorphs coexist in fractions close to (65-25-10) % wt respectively from Rietveld refinement analysis, without significant modifications of the relative ratio by varying the anionic counterpart. No potassium silicates have been identified, while an amorphous component, whose amount is consistent for the entire dataset, is present as a broad peak around 21 degrees.

As suggested by this analysis, the anionic contribution to silica crystallization is not influent as much as the type of alkali ion. The latter strongly affects the polymorph type formation, while the first one seems to modify mildly only their relative ratio, confirming the crucial role of metal cation for the induced crystallization process.

Instead, an elongation along the c-axis was observed in the tridymite and cristobalite structures, correlated with the increase in ionic radius of the metallic cation used, in both chloride and nitrate forms. This seems to suggest possible incorporation of the element into the silica crystal lattice.

2.4.2 Salts concentration effects on silica crystallizations

The effect of salt concentrations on silica crystallization via calcination treatment has been evaluated in the case of KNO_3. Different samples have been prepared by impregnation of amorphous SiO_2 with salt solutions at 1M, 0.6M, 0.2M, and 0.08M. The same calcination treatment at 1000°C-4h has been carried out and the PXRD measurements on the final products are reported in Figure 2.4.8. All the patterns display a complete crystallization in a mixture of silica polymorphs.

Particularly, the samples are mainly composed by cristobalite and tridymite phases, which vary as a function of salt concentration. High KNO_3 concentrations promotes the tridymite polymorph over cristobalite, with a maximum of 89.9% of tridymite in the 1M sample (see Figure 2.4.4), while reducing salt concentration the relative amount of the two polymorphs gradually switches in favour of cristobalite, reaching a calculated 83% weight fraction in calcinated silica with salt solution at 0.08M of KNO_3. Small quantities of quartz are present in case of low concentrations, whose weight fraction has been estimated from refinement to be around 5% at the most. Potassium silicate ($K_6O_7Si_2$, COD 8103706), which was previously considered for the indexing the diffractogram of the sample at 1M (see Figure 2.4.4), is present as impurity also in the sample prepared at 0.6M, while for lower concentrations its contribution is no more discernible.

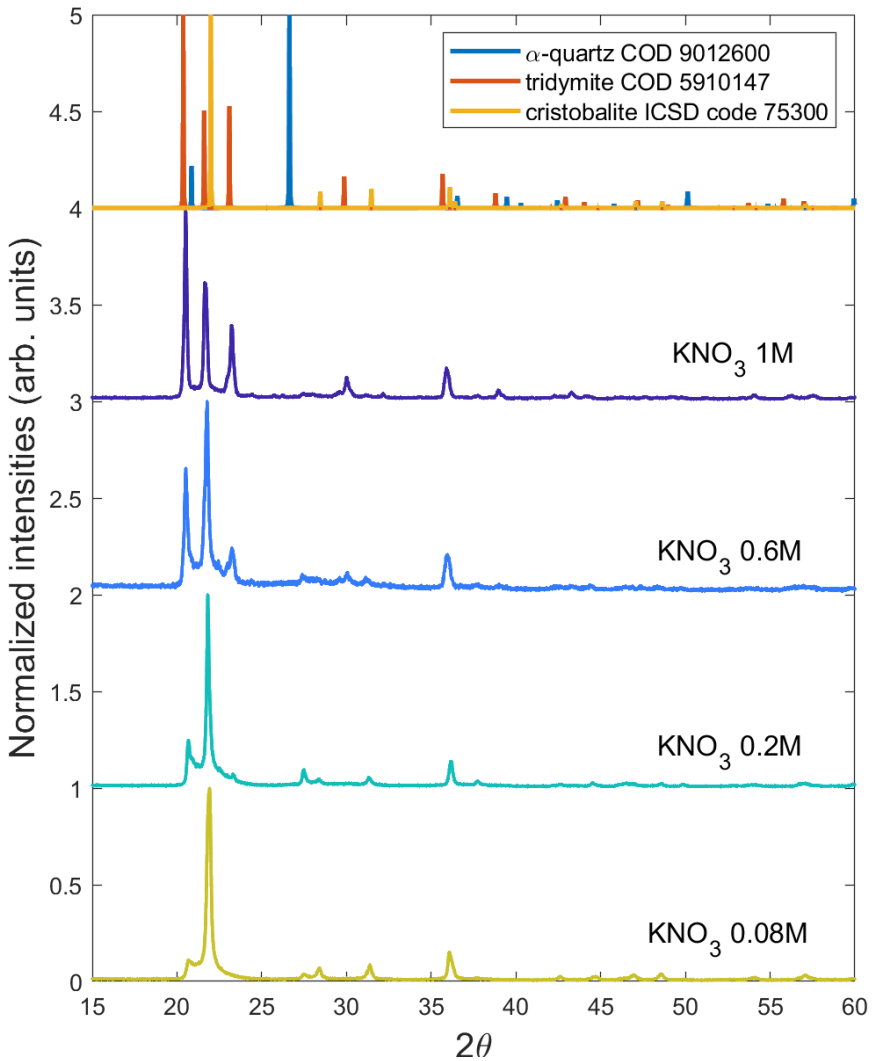

Figure 2.4.8 *PXRD patterns of calcinated SiO_2 with potassium nitrate at different concentrations at 1000°C-4h. Top: reference patterns for α-quartz, tridymite, and cristobalite.*

Considering this study in principle extendable for the whole salt series explored, these results pointed out that, by keeping constant the thermal condition of the calcination process, high salt concentrations facilitate tridymite crystallization, thus the SiO_2 polymorph metastable till 1400°C. On the other hand, low salt concentrations tend to stabilize cristobalite, which, from the phase diagram (see Figure 2.2.1) can be found above 1400°C. These considerations are coherent with what observed in the literature, where various works report on tridymite to be obtainable only with the presence of impurities or flux of carbonates, otherwise cristobalite crystallizes in the same thermal conditions[55,56]. In this way, by using high concentration of salt properly chosen and finely tuning the target temperature of calcination, it should be possible to selectively crystallize silica in its tridymite phase, study not yet investigated in literature as far as known.

2.4.3 Thermal evolution of SiO_2-alkali salt systems

Given the various observations made regarding the results of silica crystallized products, a deeper investigation of the crystallization induced mechanism has been carried out by performing in situ X-ray diffraction experiments as a function of temperature. In this way, the calcination process has been reproduced on the starting amorphous silica treated with some of the previously studied salts by heating the system from room temperature up to the target temperature, evaluating the evolution of the starting material till the product. Based on some evidence from the previously presented results, SiO_2 samples impregnated with RbCl and $NaNO_3$ have been selected as representative cases. Respect with the calcination treatment conducted with no in situ studies, the heating and cooling ramp and the calcination duration have been slightly modified due to instrumental requirements, but the thermal evolution of the two protocols can be considered quite well consistent.

The measurement protocol started with an initial data collection at room temperature (RT). Subsequently, a temperature ramp of 5°C per minute has been applied, and several diffraction patterns have been acquired maintaining a constant temperature, specifically every 100°C up to 300°C, then from 300°C to 1000°C,

selected as the target temperature, at 50°C intervals. At 1000°C the temperature was kept constant for a variable time for the selected salts due to practical compromises, whose value will be indicated later by presenting the results. After the treatment at high temperature, a cooling curve of 60°C/min has been set, and a PXRD pattern has been acquired at RT on the final product.

For all samples a series of figures reporting the PXRD patterns have been created to highlight different features of the temperature evolution. Specifically, a vertical plot from RT to 1000°C, useful for evaluating the peak shifts at different temperatures, a 3D plot, which better clarify the evolution of intensities and the alternation of different phases, and a plot of the most significant patterns collected, where the characteristic phases are more clearly observed, are reported in the following paragraphs.

Starting with RbCl-SiO_2 in situ experiments (Figure 2.4.9), the RT pattern displays only the presence of amorphous material, as a combination of silica and salt components. On the contrary, in the subsequent patterns from 100°C RbCl characteristic reflections appear (COD 9008707), displaying the distinctive shift of peaks positions to lower angles while arising the temperature up to 600°C. Beyond this temperature, the salt gradually loses its crystalline form, replaced with an amorphous broad peak observed up to 800°C. At 850°C, reflection peaks ascribable to crystalline silica phases appear, which can be indexed by cristobalite polymorph (main peak at around 22°) with a minor content of tridymite (main peak at around 21°). The reflections of this latter phase become more intense as the temperature and reaction time increase, meaning that its fraction becomes larger in the whole sample.

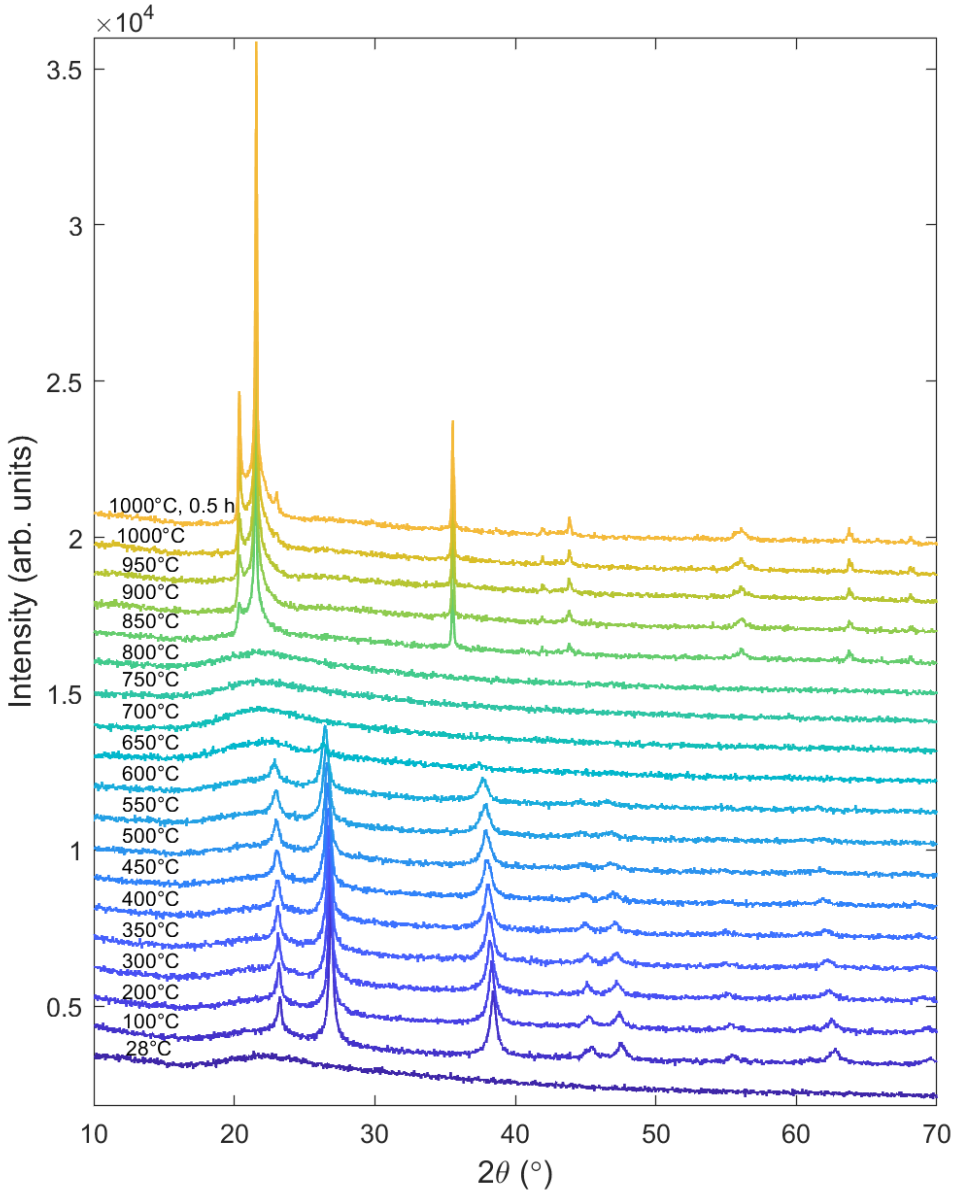

Figure 2.4.9 *Vertical plot of in situ X-ray powder diffraction data at various temperatures during the heating ramp for SiO_2 impregnated with RbCl.*

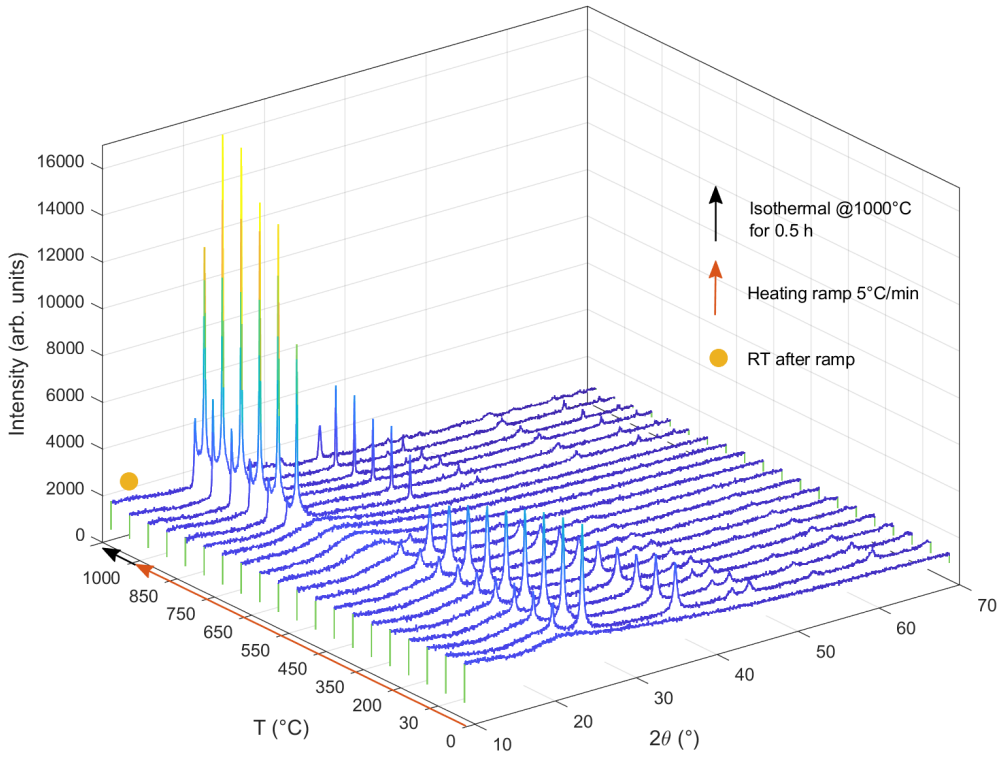

Figure 2.4.10 *3D plot of in situ X-ray powder diffraction data at various temperatures during the heating ramp (red arrow) for SiO_2 impregnated with RbCl. The maximum temperature achieved has been kept constant for 0.5 hours (black arrow). The room temperature data after the heating ramp is marked with the yellow dot.*

It is clear from the 3D plot reported in Figure 2.4.10 that the high temperature favours the crystallization of silica phases, while a reduction of diffraction peaks intensity, and thus of crystallinity, occurs when the powder is restored to room temperature conditions.

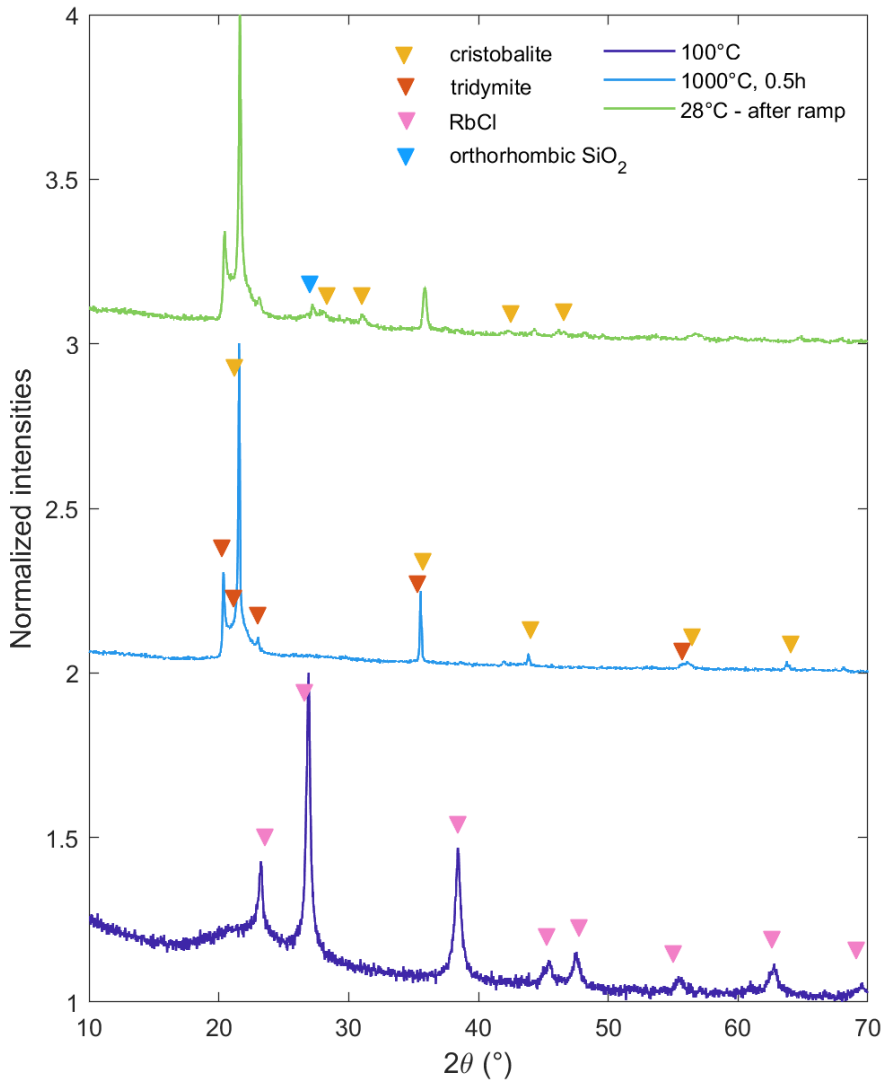

Figure 2.4.11 *In situ X-ray powder diffraction data at crucial temperatures during the heating ramp for SiO_2 impregnated with RbCl, with indexed identified phases.*

In Figure 2.4.11 the most significant PXRD patterns are summarizing, with the indexing of different identified phases. As previously described, RbCl crystallizes at 100°C and its characteristic peaks (blue line, pink triangles) index the whole pattern. The disappearance of salts' peaks at 650°C could be associated with a disorder of this phase, which could enter in an amorphous or liquid state, since this thermal regime is not far from the expected melting temperature (Table 2.3.2). At 1000°C (light blue pattern) the crystallization of silica, which already started at

850°C, reaches its completion in a mixture of cristobalite (yellow triangles) and minorly tridymite (red triangles). Releasing the heating and cooling down the system to RT after the thermal treatment (green pattern), traces of a minor phase of crystalline silica have been detected, ascribable to the orthorhombic phase previously indexed for the calcinated samples in Figure 2.4.11 (COD 9006301, blue triangle), and the presence of less intense cristobalite peaks becomes clearer.

The final product of this in situ thermal treatment is consistent with the calcination process previously presented for SiO_2-RbCl (Figure 2.4.1), in which a mixture of cristobalite and tridymite was detected. From the Rietveld refinement of the in situ data at RT after the thermal treatment, the calculated amount of cristobalite, tridymite and the orthorhombic SiO_2 has been estimated to 56%, 34%, and 9%, respectively. The differences between ex-situ and in situ experiments on the relative ratio of the two polymorphs and the presence of a small quantity of quartz in the latter case could be attributed to different reaction time (i.e. 4 hours for standard calcination vs 1 hour for in situ XRD while heating) or a different cooling rate ramp. Particularly, a longer calcination treatment favours the stabilization of the thermodynamically more stable polymorph, which is tridymite in this thermal condition (over 870°C). Analogously, slower cooling ramp gives to the system sufficient time to experience a partial reconstructive transformation from cristobalite to α-quartz, the stable phase at ambient conditions. This experimental evidence has been confirmed by performing further calcination treatments by varying the cooling ramp after, keeping constant all the other parameters involved.

In Figure 2.4.12 a PXRD pattern related to amorphous silica calcinated with RbCl impregnation and a slow linear cooling ramp of about 80 hours is shown. Comparing this result with the one presented previously (Figure 2.4.1) from a faster cooling ramp (oven inertia, around 8 hours), the salt favours the reconstructive transformation to quartz for longer cooling ramps, as pointed out by the increased intensity of its main reflection peak.

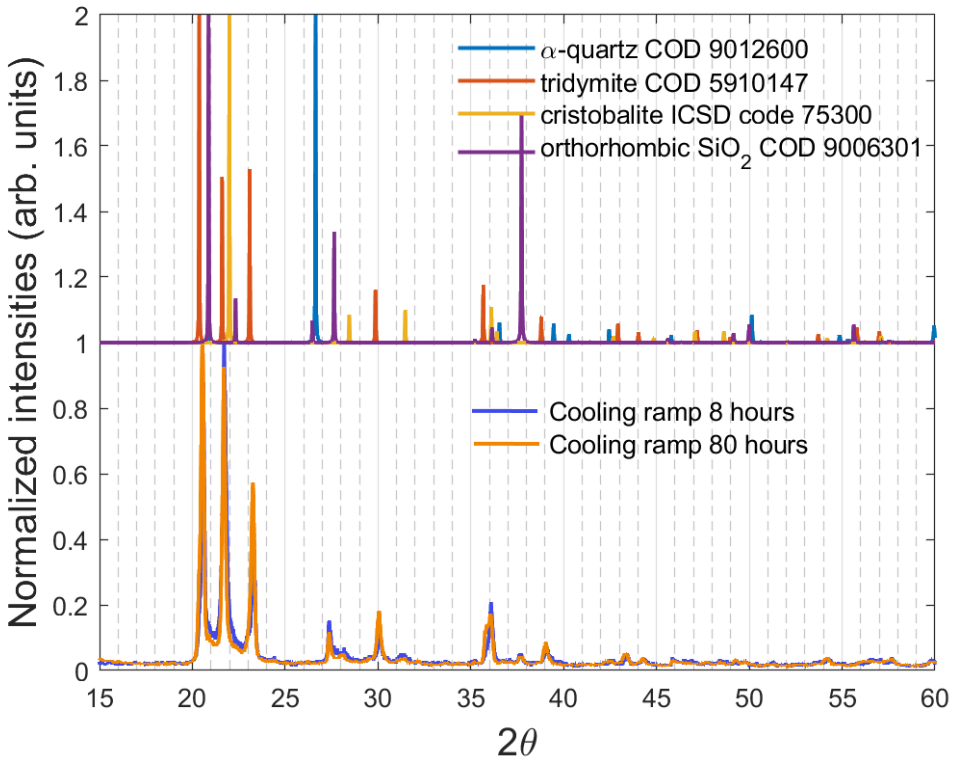

Figure 2.4.12 *Comparison between PXRD data from SiO_2-RbCl system calcinated at 1000°C-4h with a cooling ramp of around 8 hours (blue) or about 80 hours (orange). In the upper part, the references for the crystalline silica phases are reported.*

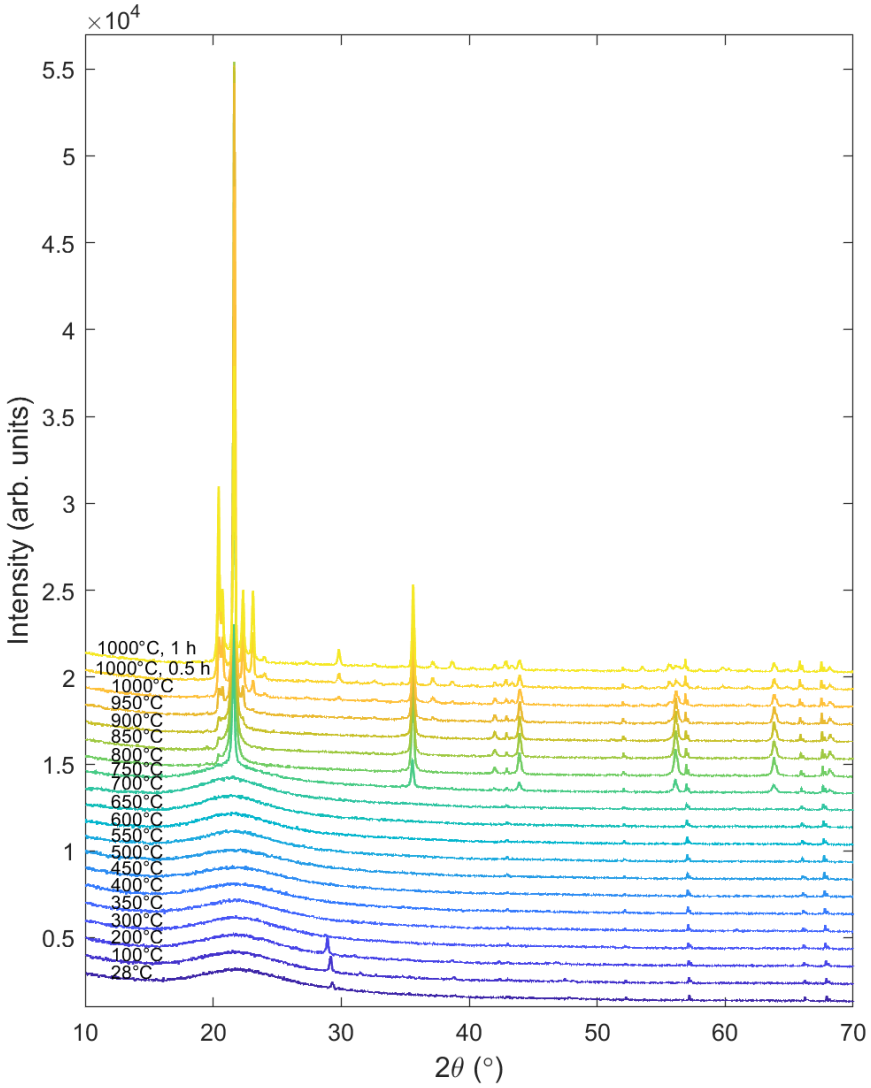

Figure 2.4.13 *Vertical plot of in situ X-ray powder diffraction data at various temperatures during the heating ramp for SiO_2 impregnated with $NaNO_3$.*

Moving to the case of nitrates, Figures 2.4.13 and 2.4.14 show the temperature trend of PXRD patterns for SiO_2 treated with $NaNO_3$. The presence of $NaNO_3$ in a crystalline form (COD 2310364) is visible from RT up to 200°C. Its crystalline phase is no longer detectable from 400°C upwards, where the entire material remains amorphous, or at least does not display long-range structural order, up to 700°C. At 750°C, the appearance of reflection peaks due to the crystallization of silica into cristobalite is observed, which initially increase in intensity as the temperature rises, then decrease as the tridymite phase becomes more abundant (above 800°C). In the whole dataset, diffraction peaks related to the Al_2O_3 (COD

1011280) are visible, contribution ascribable to the sample holder used in the high temperature chamber.

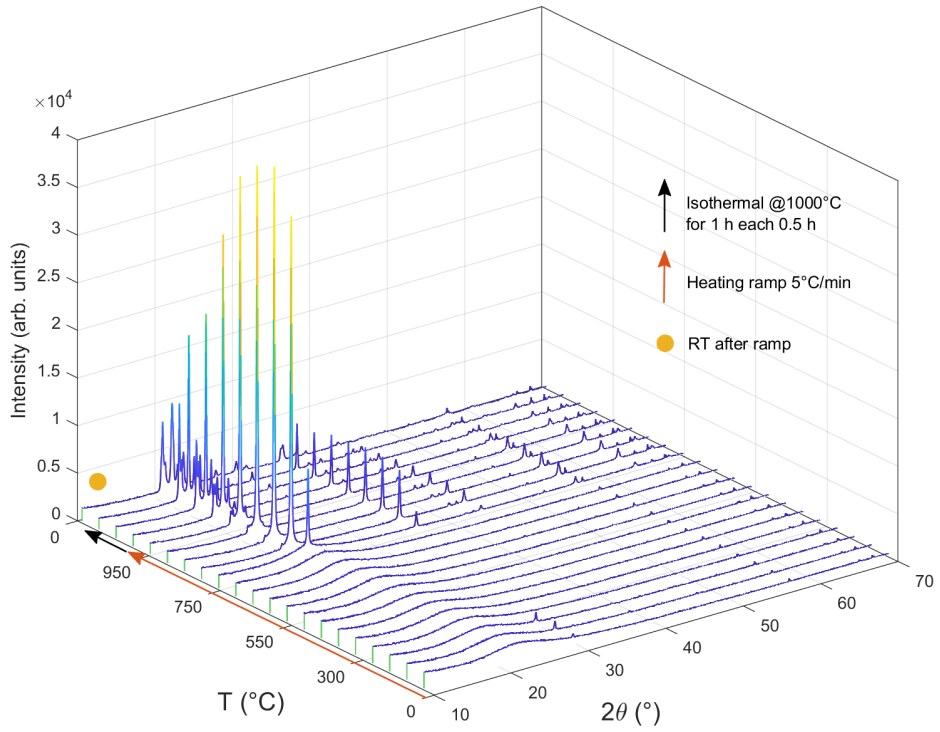

Figure 2.4.14 *3D plot of in situ X-ray powder diffraction data at various temperatures during the heating ramp (red arrow) for SiO_2 impregnated with $NaNO_3$. The maximum temperature achieved has been kept constant for 1 hour (black arrow). The room temperature data after the heating ramp is marked with the yellow dot.*

In Figure 2.4.15, the XRD patterns that best highlight the presence of certain phases are summarized and normalized. In addition to the patterns in which the maximum crystallinity for $NaNO_3$ (blue line, green triangles) and cristobalite (light blue line, yellow triangles) is achieved, the final data before releasing the heating and back to RT are reported. At 1000°C (green pattern) the presence of a tridymite component becomes clearer (red triangles), whose reflection peaks arise in intensity at RT, indicating that the system partially transform from cristobalite to tridymite after the cooling ramp. Few extra and weak diffraction peaks, not ascribable to silicates, nitrates, or sodium compounds, are detected back to RT after ramp, which

are compatible with an orthorhombic phase of silica (COD 75664). Al_2O_3 reflections, characterized by a very narrow profile peak shape, are due to the sample holder contribution and marked in the patterns (purple triangles).

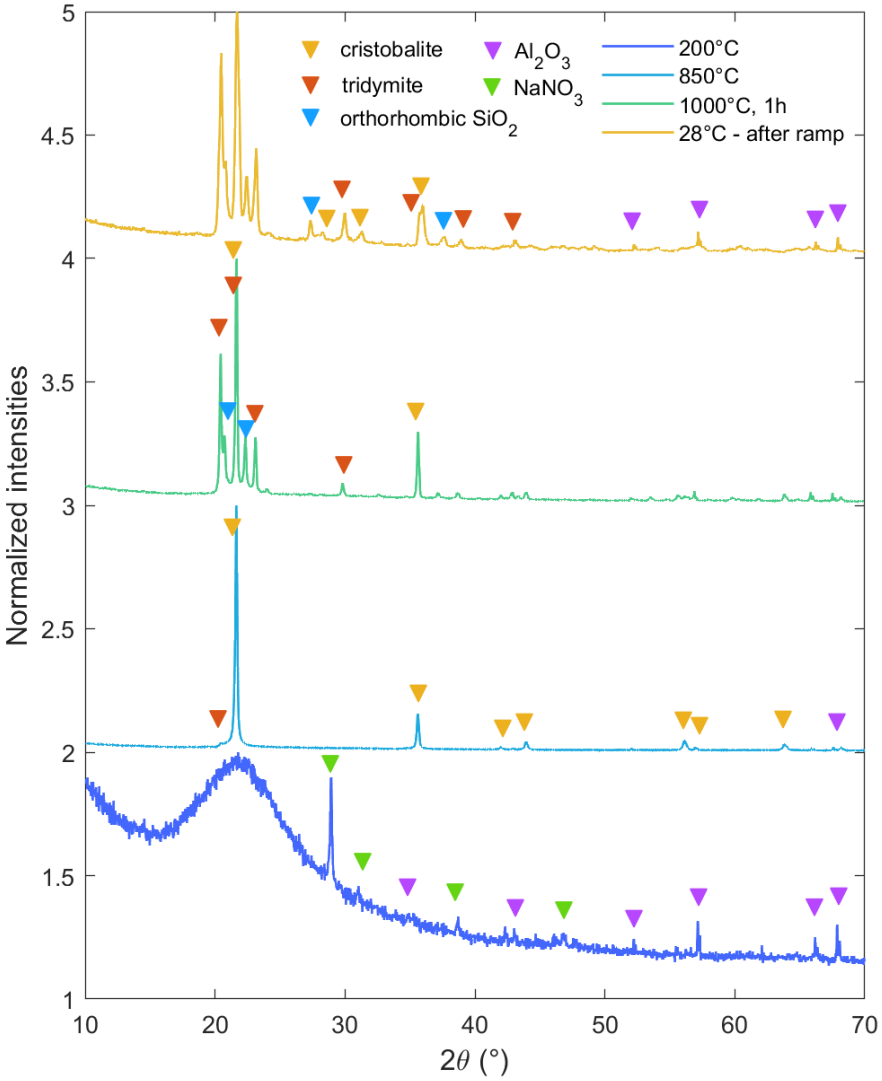

Figure 2.4.15 *In situ X-ray powder diffraction data at crucial temperatures during the heating ramp for SiO_2 impregnated with $NaNO_3$, with indexed identified phases.*

Unlike ex situ XRD patterns, where the peaks were entirely attributable to silica phases, the in situ measurements highlight the existence of temperature ranges in which the presence of crystalline salts is observed. Specifically, the patterns at RT show a total (in the case of SiO_2-RbCl system) or almost total (for SiO_2-$NaNO_3$)

amorphous phase, as the salt is still partially dissolved due to the presence of water. As the temperature increases, the water begins to evaporate, causing supersaturation of the solute, which precipitates and crystallizes, as clearly seen from the 200°C measurement onward. In the case of rubidium chloride, the presence of the associated peaks remains clear up to 600°C, beyond which the reflections are no longer visible. Contrarily, in the sample with sodium nitrate, the salt peaks disappear as early as the 300°C pattern. Considering the tabulated melting temperatures, reported to be 718°C and 308°C for RbCl and $NaNO_3$ (see Tables 2.3.2 and 2.3.3) respectively, their values are slightly higher than the temperatures at which the crystallinity of the two salts is lost. However, some aspects should be taken into account regarding the environment in which these reactions take place. As previously specified in the Paragraph 2.3, the silica used is a mesoporous material with pores ranging from 6 to 20 nm in diameter. When impregnated with an aqueous solution, the liquid is adsorbed and penetrates the pores due to capillarity. As the water evaporates, the salts precipitate forming small highly dispersed crystals, confined within the mesoporous matrix and partially on their external surface. The size of the salt crystallites, therefore, depends directly on the pores size in which they are segregated. The Debye-Scherrer equation relates the crystallite diameter D to the full-width at half maximum of a specific diffraction peak β as follows:

$$D = k\lambda/\beta cos\theta \quad (2)$$

where k is the shape factor (it varies with the actual shape of the crystallite, but has a typical value of about 0.9, as in this case), λ the radiation wavelength, and θ the Bragg angle at which the peak falls. Applying this equation on the PXRD patterns acquired in situ it has been possible to estimate the crystallite sizes for RbCl and $NaNO_3$ to be 25 nm and 35 nm, respectively. It is evident that these are very different length-scale conditions from the bulk state, referred to in the literature when reporting material properties, which can influence the thermal properties[57]. At the nanoscale materials have a high surface-to-volume ratio and, consequently, high surface energy. This phenomenon is the basis for the disappearance of the salts' crystalline peaks observed at lower temperatures, most likely corresponding to their melting.

The thermogravimetric analysis, reported below, represents the weight loss as a function of temperature for silica impregnated with RbCl (Figure 2.4.16) and $NaNO_3$ (Figure 2.4.17) samples.

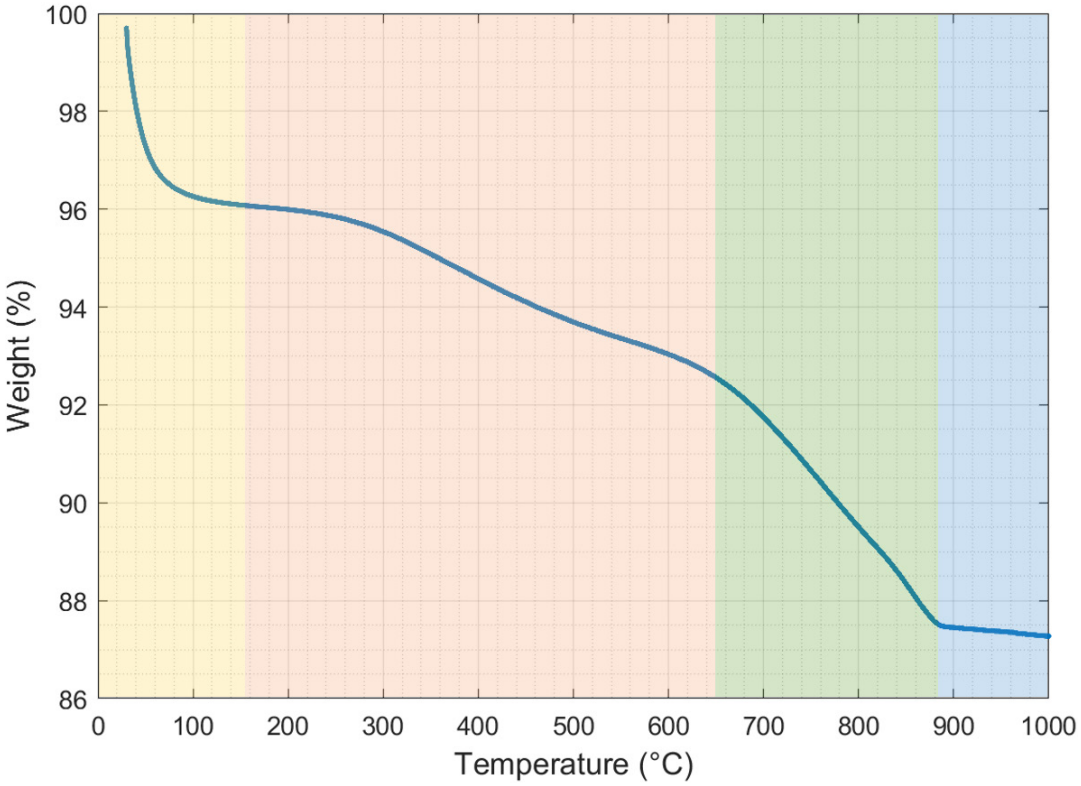

Figure 2.4.16 *Thermogravimetric analysis of SiO_2-RbCl system from room temperature up to 1000°C.*

On the SiO_2-RbCl sample, an initial weight loss, around 4%, is observed from RT to 150°C (yellow region), corresponding to the evaporation of surface physisorbed water. As the temperature increases, a relatively constant mass reduction to about 7% is present up to approximately 650°C (orange area), which is likely related to the progressive loss of chemisorbed water. Above this temperature, the weight loss becomes more pronounced as the salt exceeds its melting point in RbCl-SiO_2 system, as previously described, and begins to partially evaporate (green area), thus the system reduces its weight to around 87% of the starting amount. Beyond 850°C (blue region), the mass loss stabilizes, matching the formation temperature of the first crystalline phases of silica. This result suggests that the salt becomes unavailable for further evaporation, possibly due to its

incorporation into the silica crystal lattice, coherently with the lattice elongations calculated from PXRD analysis which differs with particular trends by varying the metal cation (see Figure 2.4.3). This incorporation may not be the consequence of SiO_2 crystallization, but, on the contrary, its real cause.

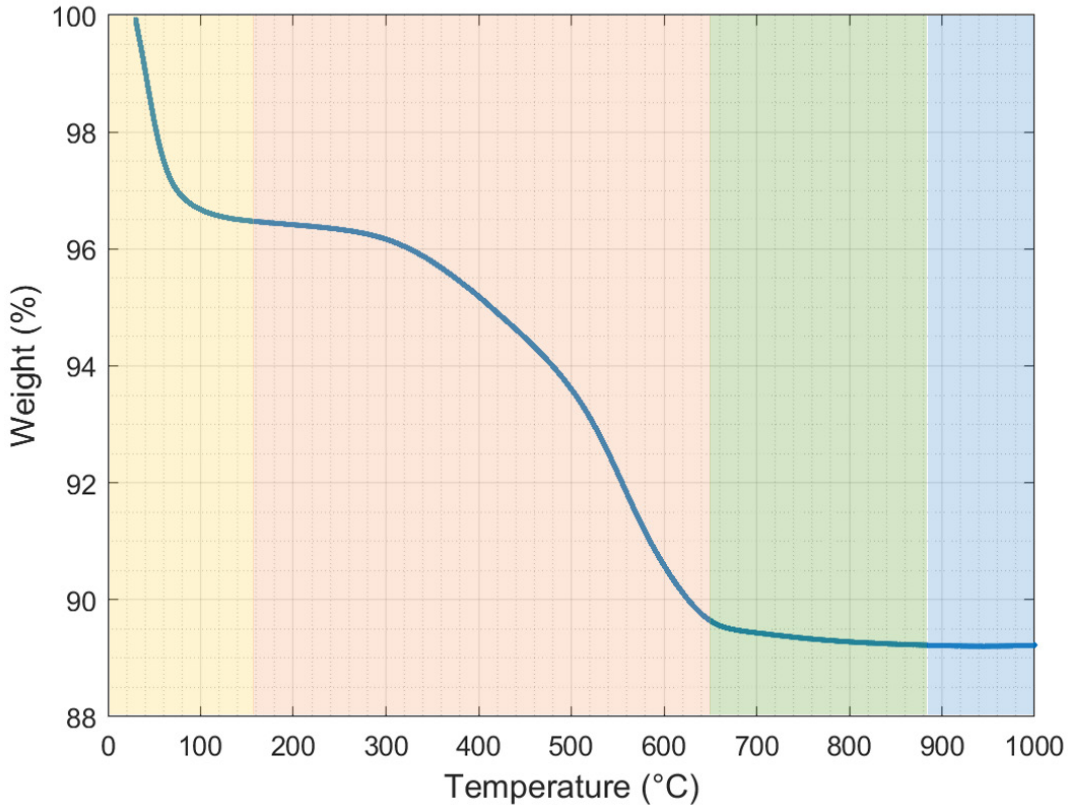

Figure 2.4.17 *Thermogravimetric analysis of SiO_2-$NaNO_3$ system from room temperature up to 1000°C.*

As for the SiO_2-$NaNO_3$ sample, an initial weight loss of about 3.5% can be observed from RT to 150°C (yellow region), due to the evaporation of surface water. From 350 to 650°C there is a weight loss regime, which could occur for multiple reasons. Particularly, one component is associated with the dehydration of silica, while concomitantly the melting of $NaNO_3$ takes place, with a possible partial evaporation and decomposition into $NaNO_2$, with loss of O_2. Above this temperature (blue region), the mass loss decreases drastically until it stops around 11%, thermal regime of the beginning of silica crystallization.

2.4.4 IR spectroscopy on SiO_2-alkali system

Silicon dioxide (SiO_2) has characteristic vibrational infrared-active modes, thus visible with infrared (IR) spectroscopy. The primary contribution arises from vibrations in the Si-O bonds within the silica network. The exact positions and intensities of these peaks can vary slightly depending on whether the SiO_2 is amorphous or crystalline and, if so, between the different polymorphs.

In the Figures 2.4.18 and 2.4.19, the IR spectra of SiO_2 samples impregnated with 1M solutions of alkali metal chlorides and nitrates and calcined at 1000°C for 4h are reported.

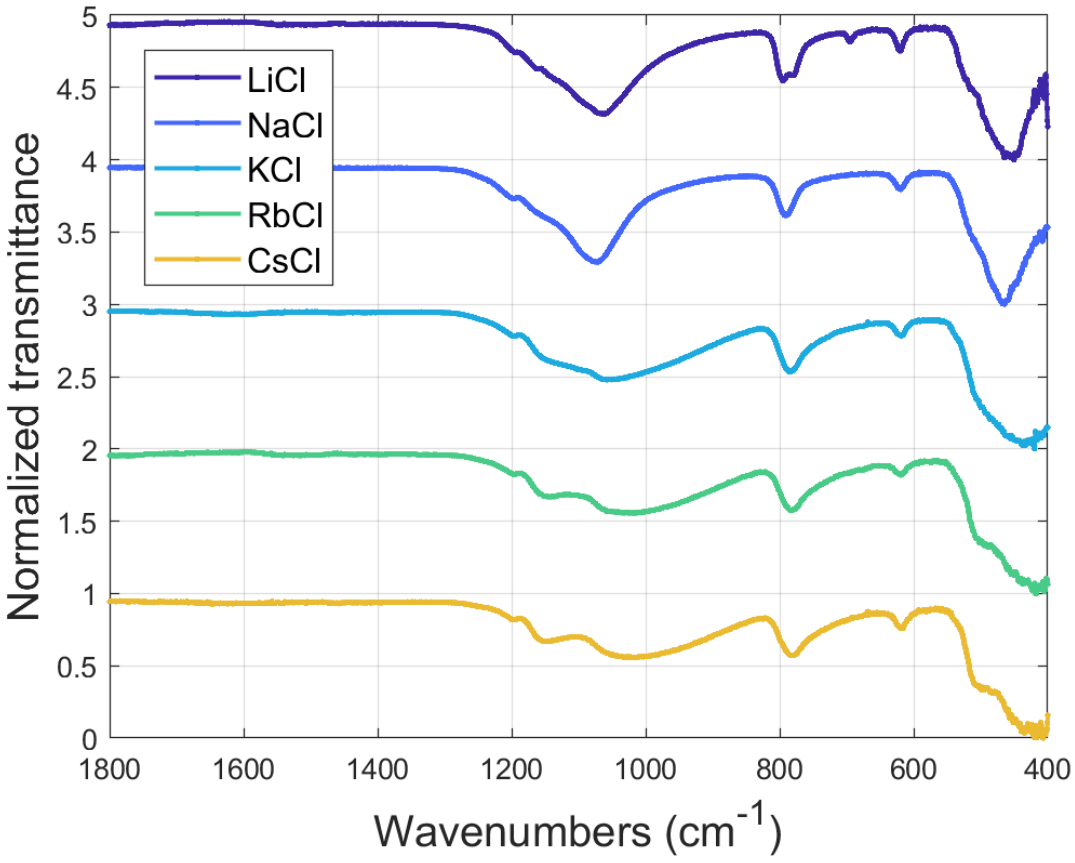

Figure 2.4.18 *Infrared spectra of calcinated SiO_2 with different alkali chlorides at 1000°C-4h.*

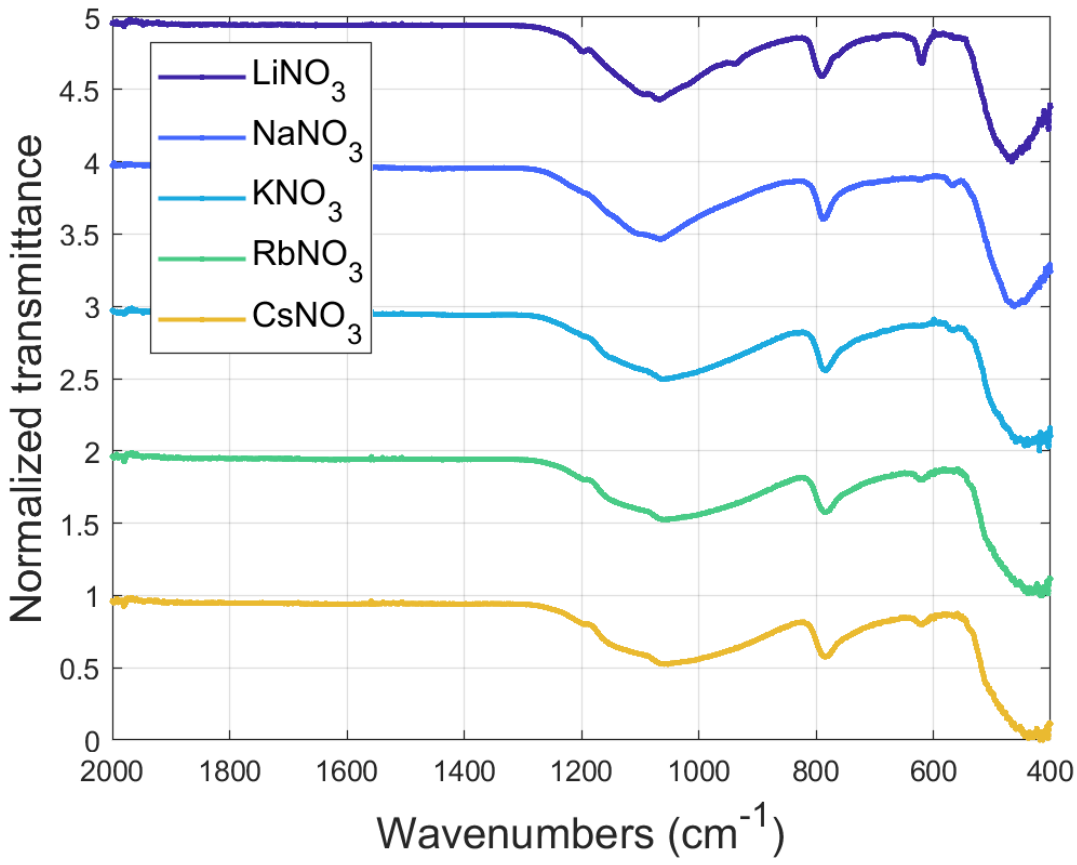

Figure 2.4.19 *Infrared spectra of calcinated SiO_2 with different alkali nitrates at 1000°C-4h.*

Some specific bands are commonly present in all the acquired IR. Particularly, the most prominent peak is around 1000-1100 cm^{-1} and arises from the asymmetric stretching of Si-O-Si bonds. At lower wavenumber, around 780-800 cm^{-1}, the peak corresponding to the symmetric stretching of the Si-O-Si bonds is visible. The bending vibrations in the O-Si-O bonds can be associated with the IR peak around 450 cm^{-1}. However, this region is very close to the minimum limit of instrumental detection, therefore the peak shape is affected by the noise due to the low energy of the signal.

The low intensity band at 950 cm^{-1}, visible only in $LiNO_3$, can be assigned to the dangling Si-O stretching mode. Another distinct peak is observed at 620 cm^{-1}, characteristic of cristobalite. It appears in all spectra but is particularly weak in samples containing $NaNO_3$ and KNO_3, which indeed exhibit low levels of this silica phase, as pointed out from PXRD analysis.

The peak at 1100 cm^{-1} progressively broadens, moving from the lithium- to the cesium-salts series. Taking into account the information provided by PXRD pattern in Figures 2.4.1 and 2.4.4, no correlation between this peak shape trend and the silica polymorphs present in the sample can be pointed out.

On the other hand, the peak around 800 cm^{-1}, which represent the symmetric stretching of the Si-O-Si, shows no apparent shape differences within chlorides and nitrates series, except for the sample containing LiCl. In that case the peak is split, and this feature is characteristic of quartz (additionally to a second vibration band at 695 cm^{-1}), effectively detected in LiCl-SiO_2 system from PXRD. What is noted instead is a progressive shift of the band position towards lower wavenumbers moving from Li to Cs series. This evidence is present in both chlorides and nitrates samples and can be visualized in Figure 2.4.20 as a function of the ionic radius of the considered cations.

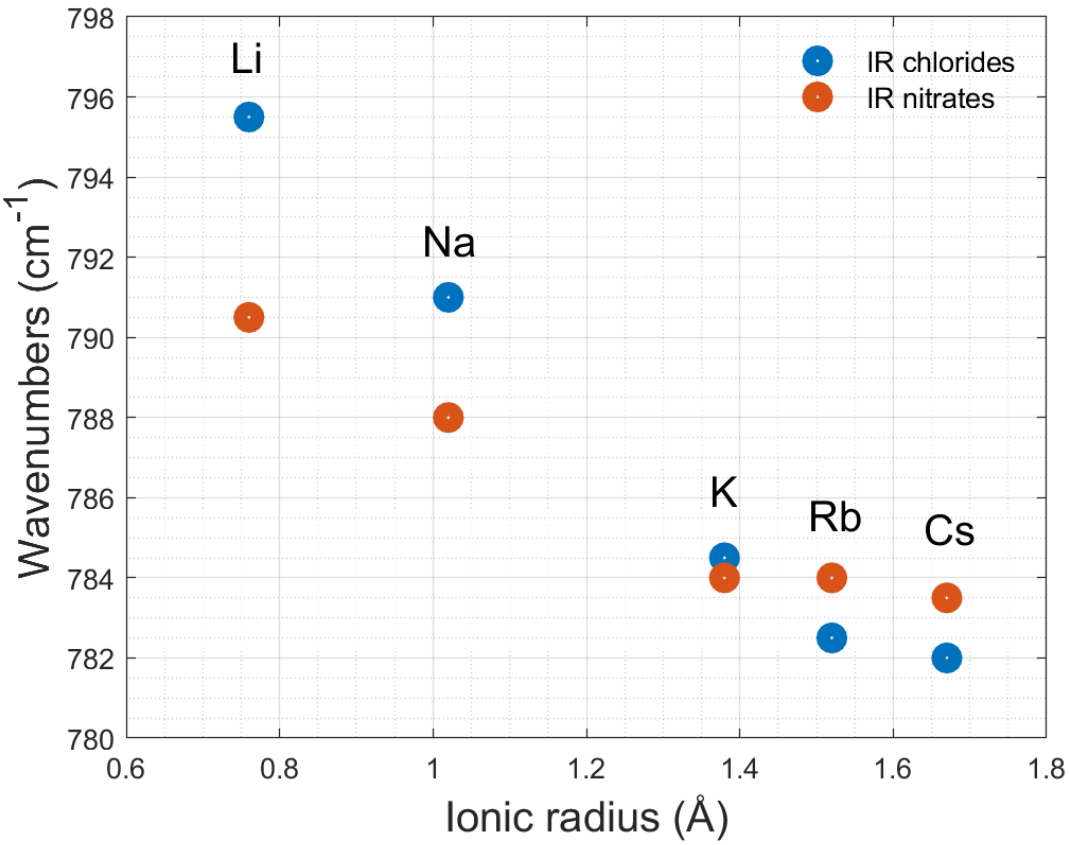

Figure 2.4.20 *Si-O-Si stretching mode wavenumber form IR spectra of alkali chlorides (blue) and nitrates (red) as a function of ionic radius of the metal cation.*

Once again, as for the peak at 1100 cm^{-1}, there is no connection with the silica polymorphs present in the samples, observed by XRD, and the noted shift. Instead, the analysis reveals a pseudo-linear correlation between the wavenumber shift and the ionic radius of the alkali metal cation. For both chlorides and nitrates, the wavenumber associated with the symmetric stretching of Si-O-Si decreases progressively from lithium to cesium sample. Chlorides show a maximum shift of approximately 14 cm^{-1}, while nitrates exhibit a smaller variation of approximately 7 cm^{-1}. Despite this gap, both salt types display a consistent trend, suggesting that the key role belongs to the metal cation.

As pointed out from the IR spectra investigation, the presence of the metal cation during the calcination treatment influences the vibrational motions of the resulting crystallized silica. Particularly, a shift of the peaks towards lower frequencies (and energies) for the band associated with the symmetric stretching of the Si-O-Si bonds and a broadening of the band corresponding to the asymmetric stretching of the Si-O-Si bonds seems to be the major observable modifications, in a manner dependent on the radius of the employed cation. These variations may be attributed to an increase in bond lengths or the presence of local structural disorder within the material[58]. This suggests that the cation might be partially incorporated into the crystal lattice, causing slight distortions in the lattice structure. Such incorporation could lead to changes in bond distances, as previously indicated by the structural analysis of the cell parameters (see Figures 2.4.3 and 2.4.6), and potentially disrupt the regular arrangement of atoms.

SEM measurements were performed on some samples, evaluating material morphology and elemental compositional EDX analysis. Few images and EDX maps will be reported below as explicative examples. It should be noted that silica is a low-conductivity material, which by its nature limits the potential for high magnification and the full capabilities of this electron microscopy technique. Nonetheless, attempts were made to obtain useful information for understanding the objects of this study.

The Figure 2.4.21 show the morphology of the silica sample impregnated with KCl and subjected to heat treatment.

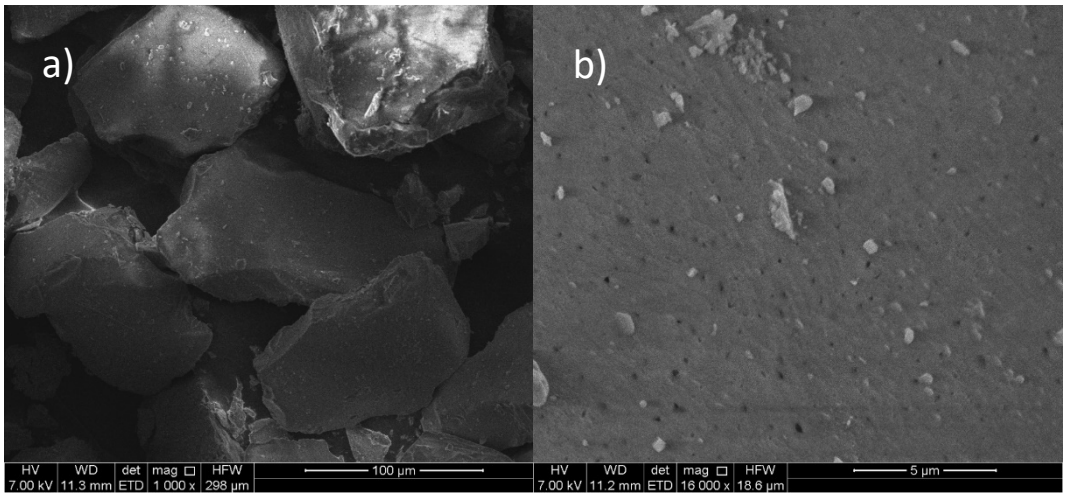

Figure 2.4.21 *SEM images of SiO_2-KCl sample at a) low and b) high magnification.*

At low magnification, no significant differences are observed compared to the starting silica, shown in the Figure 2.3.1b. Upon magnification, the surface appears similarly compact and uniform, but small pores, on the order of hundreds of microns, are noticeable as darker spots.

For samples treated with $NaNO_3$ and RbCl, a different approach of investigating the morphology has been proposed. The final powders were embedded in an epoxy resin and polished to flatten the surface, as a way to observed in section silica grains. EDX maps were collected and are shown in the Figures 2.4.22 and 2.4.23.

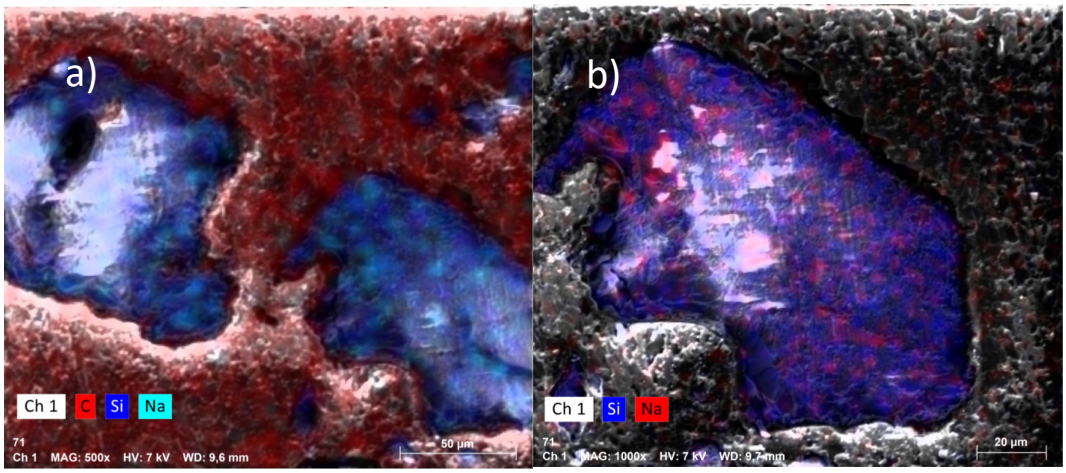

Figure 2.4.22 *EDX maps of SiO_2-$NaNO_3$ sample embedded in epoxy resin a) in red and b) in dark grey.*

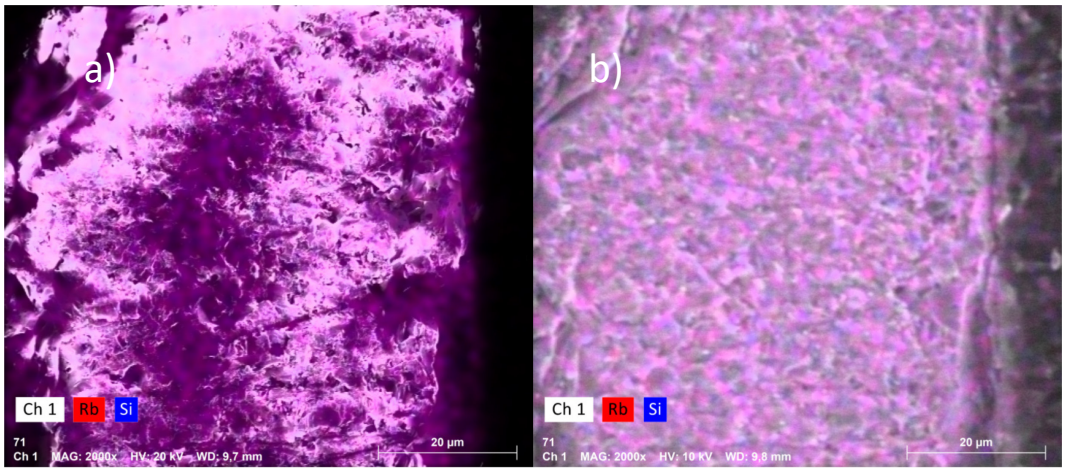

Figure 2.4.23 *EDX maps of SiO_2-RbCl sample embedded in epoxy resin (represented by the dark parts on the sides).*

The surface irregularities and the significant thickness of the insulating material complicate the acquisition of accurate quantitative values, so the considerations will be limited to a qualitative analysis of the images provided. As can be seen, the presence of the additive element is clearly visible, though it is not locally distinguishable from the silica matrix. Conversely, both sodium and rubidium appear uniformly distributed across the sample (the checkered pattern in Figure 2.4.22 of SiO_2-$NaNO_3$ is an artifact), suggesting these cations diffuse into and remain incorporated within the silica matrix.

2.4.5 Structural analysis of calcinated amorphous SiO_2 with alkaline earth salts

In analogy with the study presented in the previous paragraphs on the series of alkali chlorides and nitrates, amorphous silica crystallization induced by alkali-earth metal in form of chlorides or nitrates (i.e. $MgCl_2$, $CaCl_2$, $Mg(NO_3)_2$, and $Ca(NO_3)_2$) will be discussed here below. The same experimental conditions for the calcination treatment have been employed, thus keeping constant the heating/cooling ramps, the target temperature to 1000°C and the duration to 4 hours.

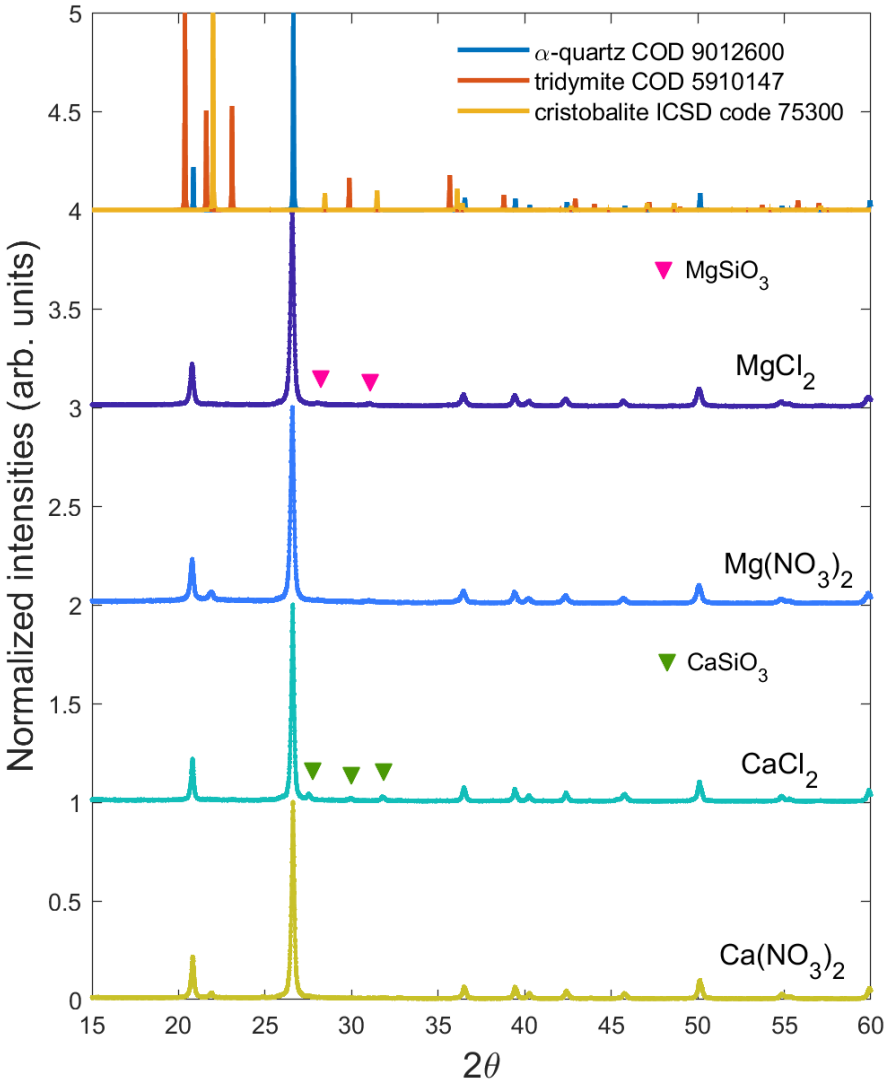

Figure 2.4.24 *PXRD patterns of calcinated SiO_2 with Mg- and Ca- based chlorides and nitrates at 1000°C-4h. Spurious phases of silicates are indicated with triangles. Top: reference patterns for α-quartz, tridymite, and cristobalite.*

From PXRD patterns reported in Figure 2.4.24, it is evident that all the tested salts favour the crystallization of silica into α-quartz polymorph, contrarily to alkali chlorides and nitrates which promote cristobalite and tridymite formation. However, a small amount of cristobalite has been detected for $Mg(NO_3)_2$ and $Ca(NO_3)_2$, in whose patterns only the main peak is visible. Rietveld refinement of the datasets calculated a weight fraction percentage of quartz greater than 90% for all the samples, with a maximum of 96.8% in SiO_2-MgCl system, while the higher

cristobalite amount was reported for $Mg(NO_3)_2$ as equal to 6.7% wt. Moreover, a very small quantity of cristobalite has been calculated in $CaCl_2$ to be 0.6%, although this value is too low to reliable. Nevertheless, some small reflections not indexable by any silica polymorph phase are present in PXRD patterns of calcinated samples with $MgCl_2$, $CaCl_2$, and $Ca(NO_3)_2$. Indeed, these peaks were attributed to magnesium or calcium silicates, as protoenstatite $MgSiO_3$ (COD 1548549) and wollastonite or pseudowollastonite $CaSiO_3$ (COD 9005778 and 9002179 respectively). The whole amount of silicate has been estimated from refinement to be 3% wt for $MgCl_2$, 9% wt for $CaCl_2$, and 1.5% wt for $Ca(NO_3)_2$. This quantitative analysis pointed out that the formation of silicates, thus a chemical reaction between amorphous SiO_2 and alkali-earth salts during the calcination treatment, is more favoured in case of chlorides. However, a selective crystallization of quartz is here promoted, contrarily to the case of nitrates in which a minor phase of cristobalite is present.

In Figure 2.4.25 the calculated values obtained from Rietveld refinement for a and c lattice constants of quartz, the predominant polymorph detected, are reported for all the tested alkali-earth chlorides and nitrates. The two lattice parameters display the same trend for the different salts, thus also the cell volume of quartz follows this evolution. However, considering the maxima and minima values for a and c parameters, thus those of $Mg(NO_3)_2$ and $Ca(NO_3)_2$ respectively, the maximum change of cell constants estimated by varying the salt is $\Delta a = 0.007$ Å and $\Delta c = 0.004$ Å. These values are consistent with the error that can be assumed for the refinement calculation of cell parameters and, consequently, all the values can be considered compatible. This behaviour is different from the case of alkali salts, in which the cell parameters displayed particular evolutions and more significant deviations for different alkali metals, with calculated values for Δa and Δc around 10 times higher for the whole dataset respect with the alkali-earth metals.

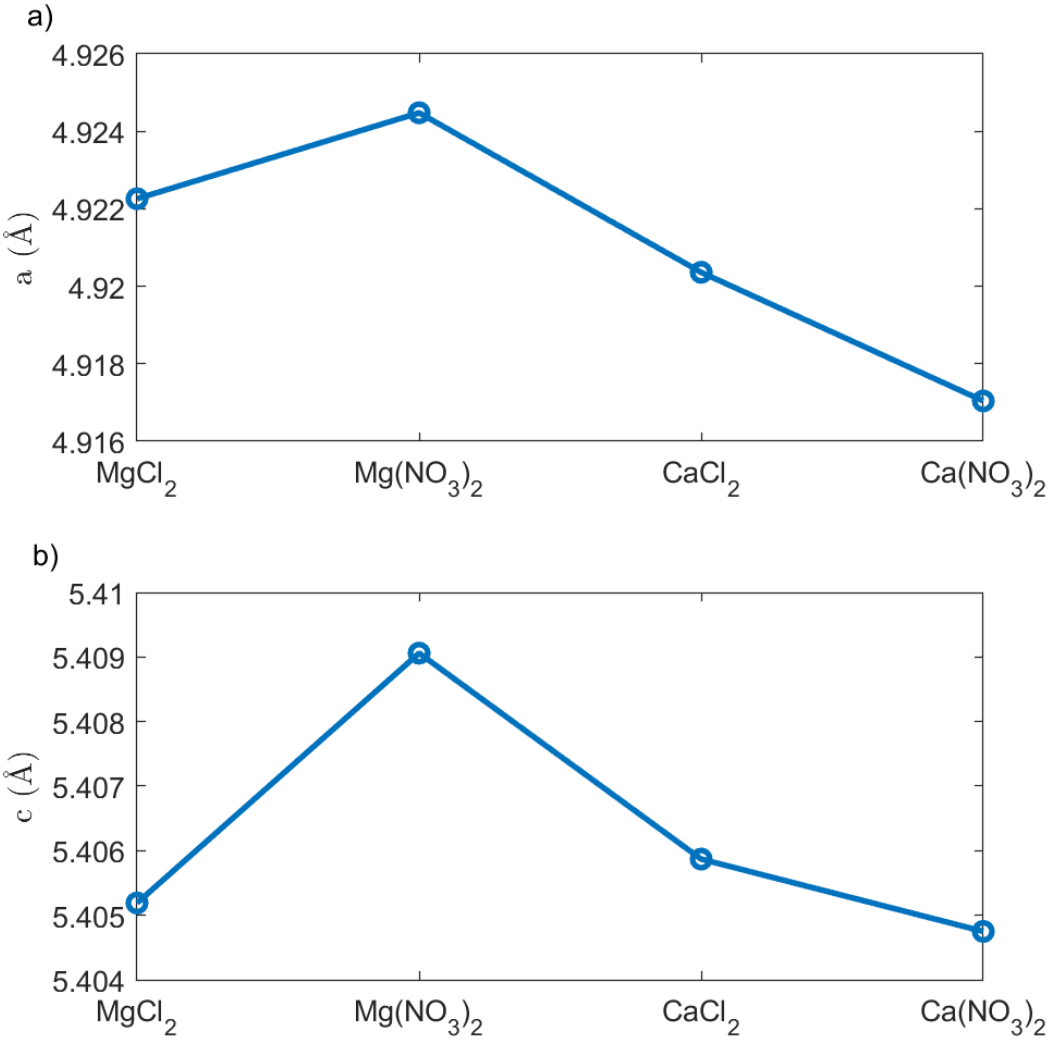

Figure 2.4.25 *Lattice constants a (a) and c (b) trend of quartz calculated from Rietveld refinement of different alkali-earth chlorides and nitrates used for SiO_2 crystallization.*

2.4.6 Thermal evolution of SiO_2-alkaline earth salts systems

To better understand the evolution of amorphous silica to its crystalline form during the calcination process also in the case of alkali-earth salts as MIC source, in situ experiments on SiO_2-$CaCl_2$ system as a function of temperature have been conducted. As for alkali metals, the starting impregnated sample has been heated from room temperature up to 1000°C with a heating ramp of 5°C/min. The simulated calcination has been carried out for 2 hours, and then the system has been cooled down with a cooling ramp of 60°C/min. PXRD patters have been acquired

during the whole treatment and report here as a vertical plot (Figure 2.4.26) and a 3D plot (Figure 2.4.27). Additionally, in Figure 2.4.28 the most significant patterns for the comprehension of the evolution are highlighted.

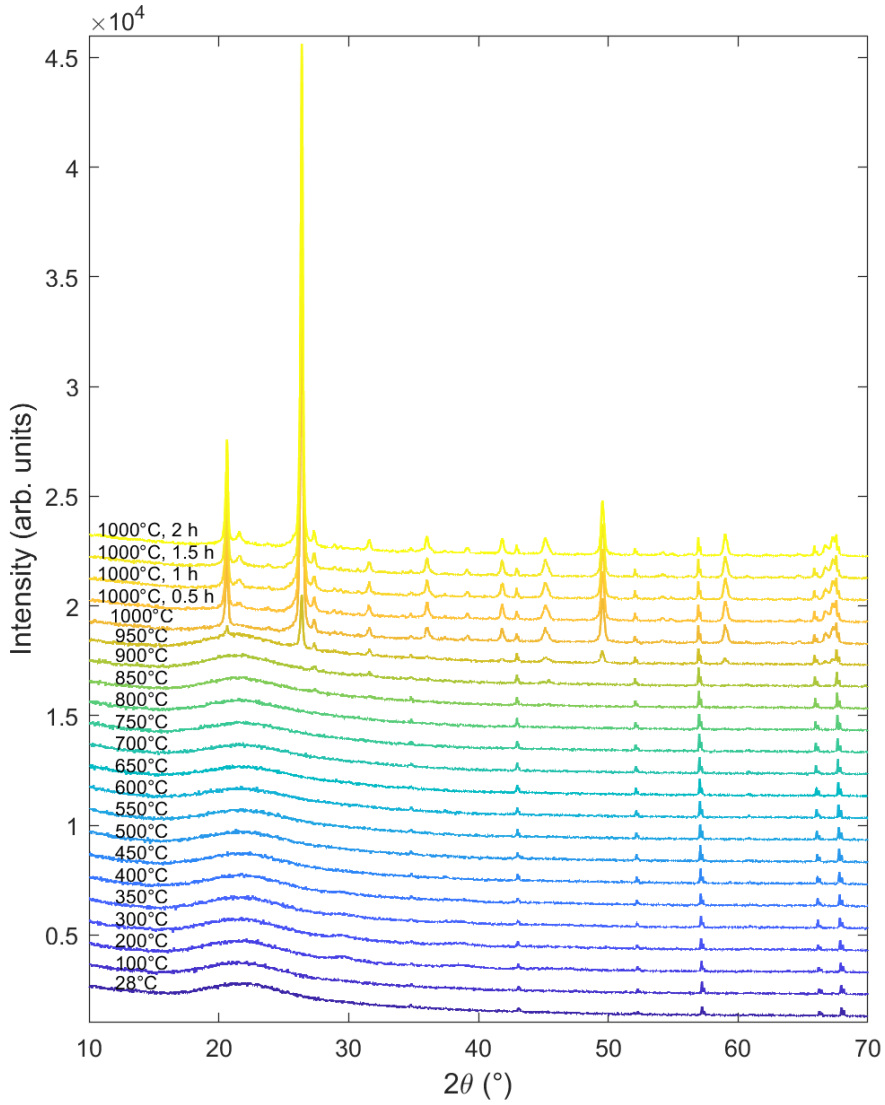

Figure 2.4.26 *Vertical plot of in situ X-ray powder diffraction data at various temperatures during the heating ramp for SiO_2 impregnated with $CaCl_2$.*

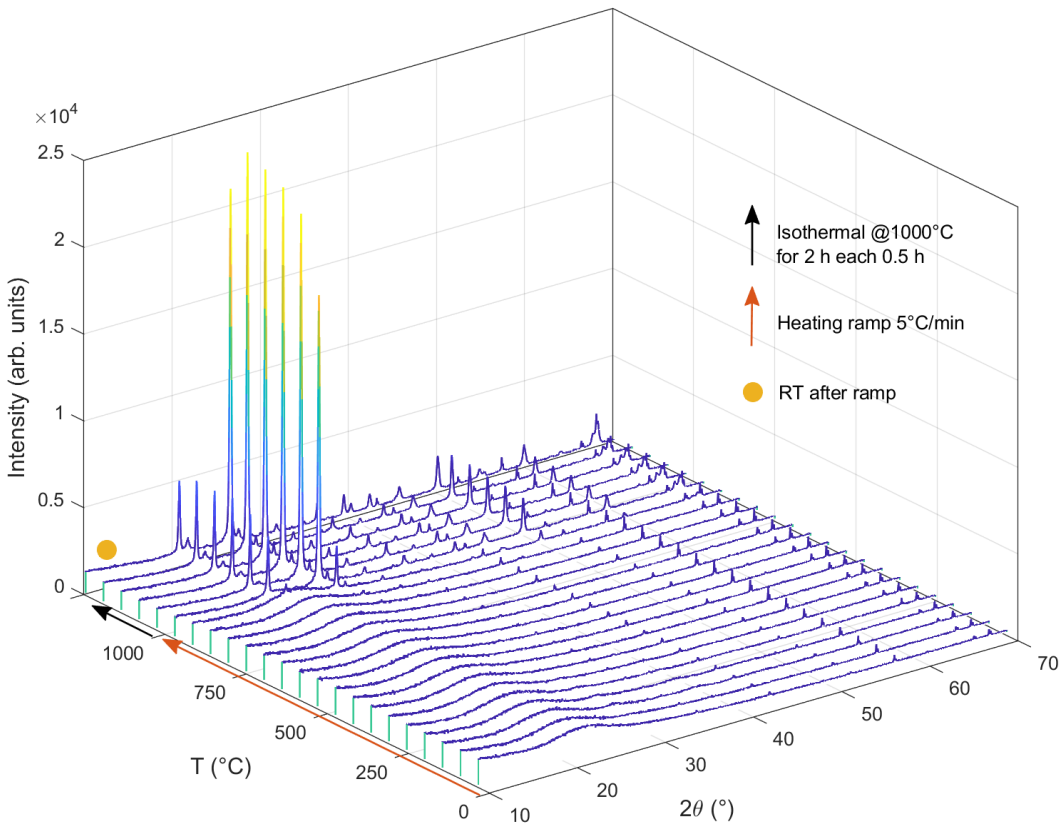

Figure 2.4.27 *3D plot of in situ X-ray powder diffraction data at various temperatures during the heating ramp (red arrow) for SiO_2 impregnated with $CaCl_2$. The maximum temperature achieved has been kept constant for 2 hours (black arrow). The room temperature data after the heating ramp is marked with the yellow dot.*

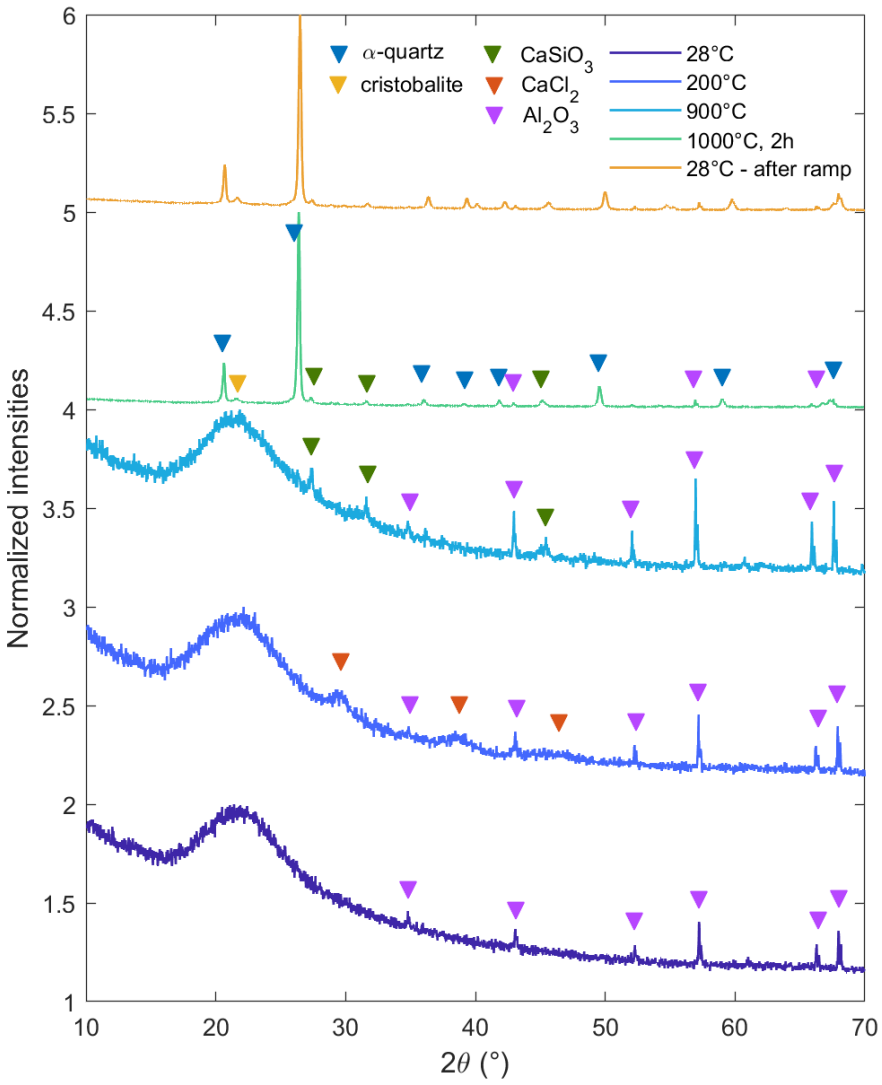

Figure 2.4.28 *In situ X-ray powder diffraction data at crucial temperatures during the heating ramp for SiO_2 impregnated with $CaCl_2$, with indexed identified phases.*

Following the patterns reported in Figure 2.4.28 at room temperature (dark blue line) the diffraction pattern shown the characteristic broad peak, centred around 21°, ascribable to an amorphous phase. The aluminium oxide sample holder contributes with low intense and very narrow peaks (purple triangles), whose will be present in all the acquired patterns. From 100°C few broad peaks compatible with $CaCl_2$ reflections (COD 1011280) appear, displaying their major intensity at 200°C (blue line), till 450°C, where they cannot be distinguished from a global

amorphous diffractogram. From 850°C (light blue line) $CaSiO_3$ reflections are visible, preceding quartz crystallization which starts after 100°C. The main peak of cristobalite can be seen in all the subsequent patters, attributing at this component only a very small fraction of the sample, predominantly crystallized in quartz structure.

The thermogravimetric analysis reported in Figure 2.4.29 represents the weight loss as a function of temperature increase for silica treated with $CaCl_2$.

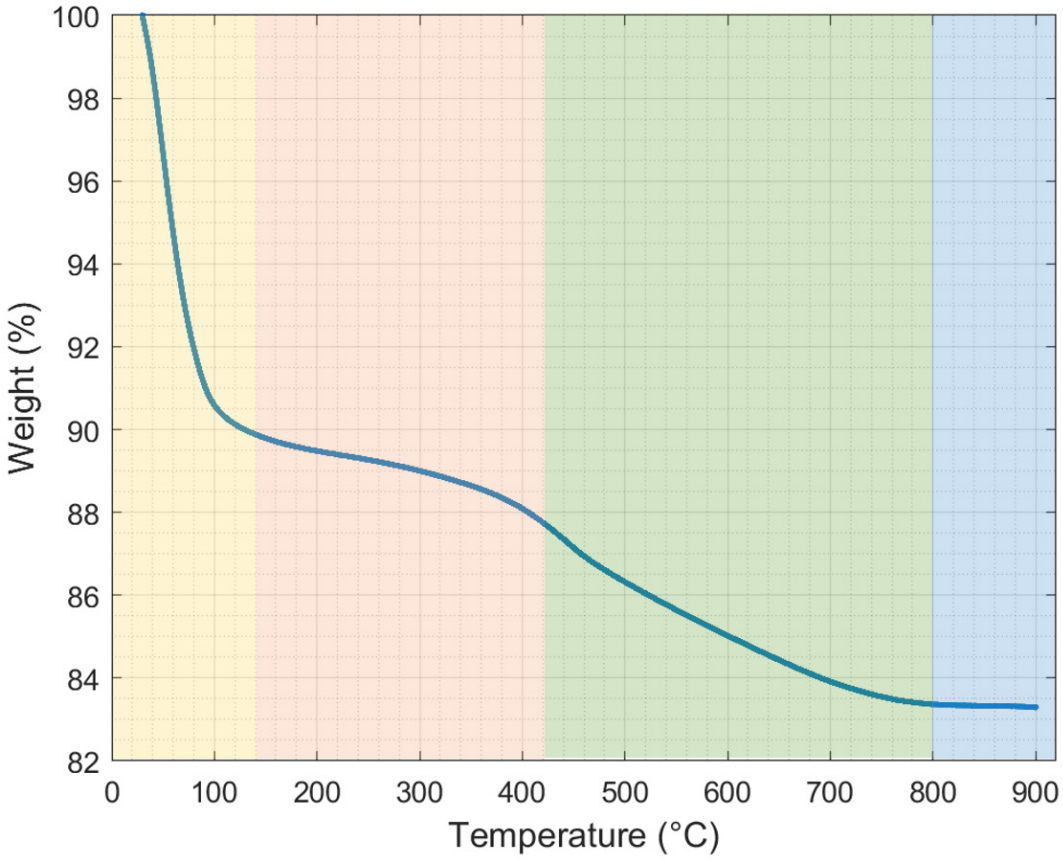

Figure 2.4.29 *Thermogravimetric analysis of SiO_2-$CaCl_2$ system from room temperature up to 900°C.*

In SiO_2-$CaCl_2$ sample, a considerable weight loss of over 10% is immediately observed from room temperature to about 150°C (yellow region), corresponding to the loss of surface water from the silica, but also to the dehydration of the $CaCl_2$, which progressively loses at least 4 of the initial 6 H_2O molecules of hydration. As the temperature increases, a relatively constant mass reduction is

present up to approximately 400°C (orange area), which is likely related to the progressive loss of -OH from the silica and the totally dehydration of $CaCl_2$[59]. Above this temperature (highlighted in green), the weight loss rate becomes more intense. This could coincide with the start of the decomposition of $CaCl_2$ or even their partial evaporation[59]. In fact, as can be observed from the PXRD patterns (Figure 2.4.28), $CaCl_2$ is characterized by very broad peaks, which should mean very small crystallite sizes. As mentioned above for the case of alkali salts, lowering the dimensions to the nanoscale can significantly reduce the melting temperatures and increase the reactivity of a compound. Beyond 800°C (blue region) further mass losses are no longer visible, nearly in correspondence of the initial formation temperature of the calcium silicate, as previously shown in PXRD (Figure 2.4.28).

2.4.7 IR spectroscopy on SiO_2-alkaline earth system

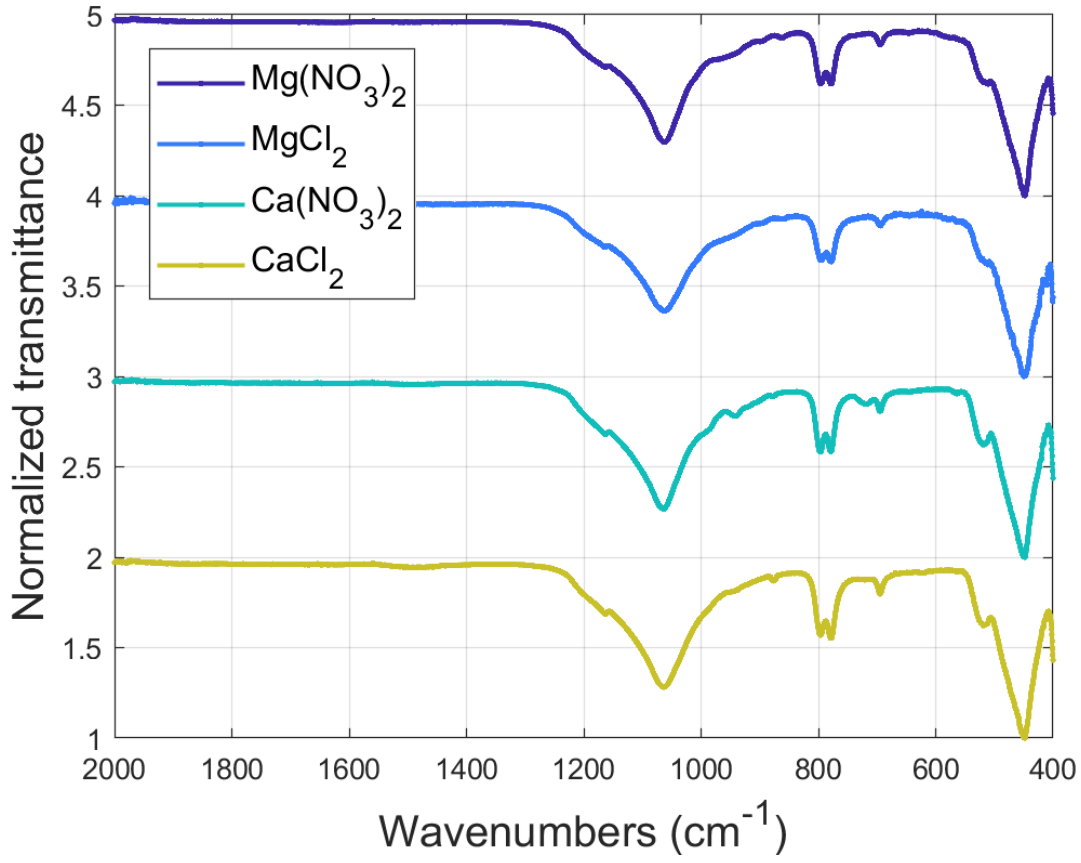

Figure 2.4.30 *Infrared spectra of calcinated SiO_2 with different alkaline earth salts at 1000°C-4h.*

Infrared spectra of calcinated SiO_2 with different alkaline earth salts are reported in Figure 2.4.30. The absorption peaks of all the samples look very similar. This feature reflects the very close crystalline nature of SiO_2-alkaline earth salts systems, which predominantly crystallize in quartz polymorph and consequently are characterized by the same vibrational modes between Si and O atoms. Contrarily to alkali salts, no correlations can be observed considering the vibration mode wavenumbers and the metal cation, or the anionic counterpart. The absence of absorption bands shifts by varying the alkaline earth salt is coherent with the considerations on the calculated lattice parameters of quartz for calcinated sample, in which again no changes have been detected with SiO_2 impregnated with Mg- or Ca- chlorides or nitrates. These results suggest that alkaline earth does not affect the lattice of quartz at the local level, without causing cell distortions and/or stretching modes, coherently with what observed from PXRD analysis (Figure 2.4.25) in which no particular correlation of lattice parameters have been observed by varying the metal cation source of MIC.

2.4.8 Searching for additives

ICP spectroscopy has been performed on silica with alkali chlorides and $Ca(NO_3)_2$ after calcination. The required acid wash, described in Materials and methods paragraph, does not alter SiO_2 crystallized phase, with no dissolution of lattice. On the contrary, the treatment allows only what the acid can solubilize to be brought into solution, in this case, salts or their derivatives containing alkaline earth elements. As explained earlier, the analysis is effectively able to detect only the cations. To intuitively evaluate the amount of metal found, each mole of the element is considered to correspond to one mole of the salt (e.g., 1 mol Mg = 1 mol $MgCl_2$). Therefore, knowing how many moles of salt were initially used, it was possible to make a comparison with the moles found.

In Table 2.4.1 the percentage values of the moles found with ICP spectroscopy of respect with the moles of salts added during silica impregnation are reported for the measured SiO_2-salts calcinated systems.

Salts	Moles found/moles added
$MgCl_2$	73%
$CaCl_2$	81%
$Ca(NO_3)_2$	63%

Table 2.4.1 *IPC spectroscopy results for $MgCl_2$, $CaCl_2$, and $Ca(NO_3)_2$.*

The high percentage values of alkali metals detected from ICP spectroscopy means that these amounts of material are solubilized by the acid solution and can be removed from the samples, suggesting a possible aggregation of these compound on silica grain boundaries or at least non-insertion of the metal/salt inside SiO_2 crystal structure. This contrasts with what suppose for alkali salts, in which MIC could be induced by insertion of the alkali metal inside the structural cavities of SiO_2 polymorphs, underlining a possible different driving mechanism for MIC on silica treated with alkali-earth salts.

After the ICP treatment, the acid-insoluble solid residue dried and further PXRD measurements have been carried out. In Figures 2.4.31, 2.4.32 and 2.4.33 the diffraction patterns of SiO_2-salts systems before and after the ICP treatment are reported, with the reference reflections of indexed phases on the top panel.

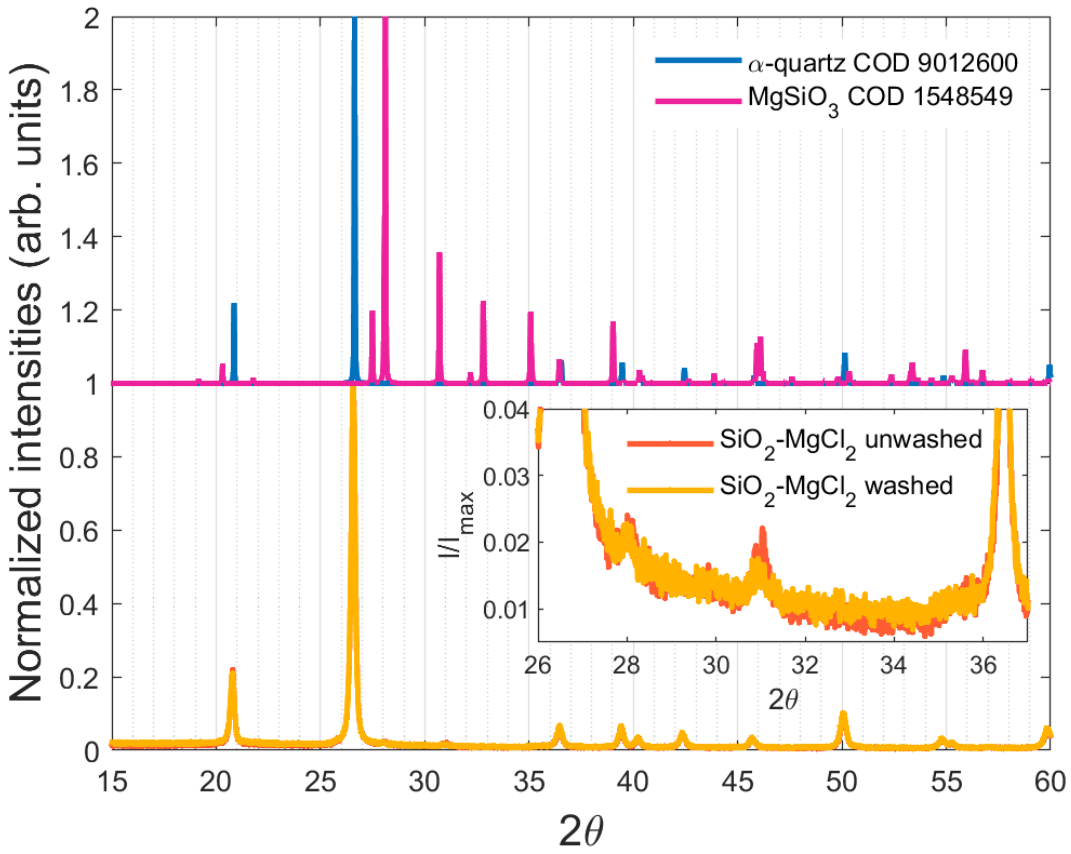

Figure 2.4.31 *X-ray powder diffraction patterns of calcinated SiO_2 with $MgCl_2$ before (red line) and after acid wash (orange line). Inset: zoom in 2theta range 26°-37°. Top: reference patterns for α-quartz (blue line) and $MgSiO_3$ (pink line).*

Although the PXRD patterns seem to be identical, some differences can be observed in the inset of each figure, where the crucial 2theta range related to silicates impurities has been zoomed in. Indeed, the diffraction peaks previously ascribed to $MgSiO_3$ or $CaSiO_3$ pseudowollastonite and wollastonite polymorphs, whose major peaks fall between 26° and 35°, on unwashed samples display a significant intensity lowering, with a complete disappearance in the sample calcinated with $CaCl_2$ (Figure 2.4.32). To quantitatively evaluate the differences in relative phase fraction, a Rietveld refinement of the datasets has been conducted and the results on the weight percentages of each identified component are reported in Table 2.4.2.

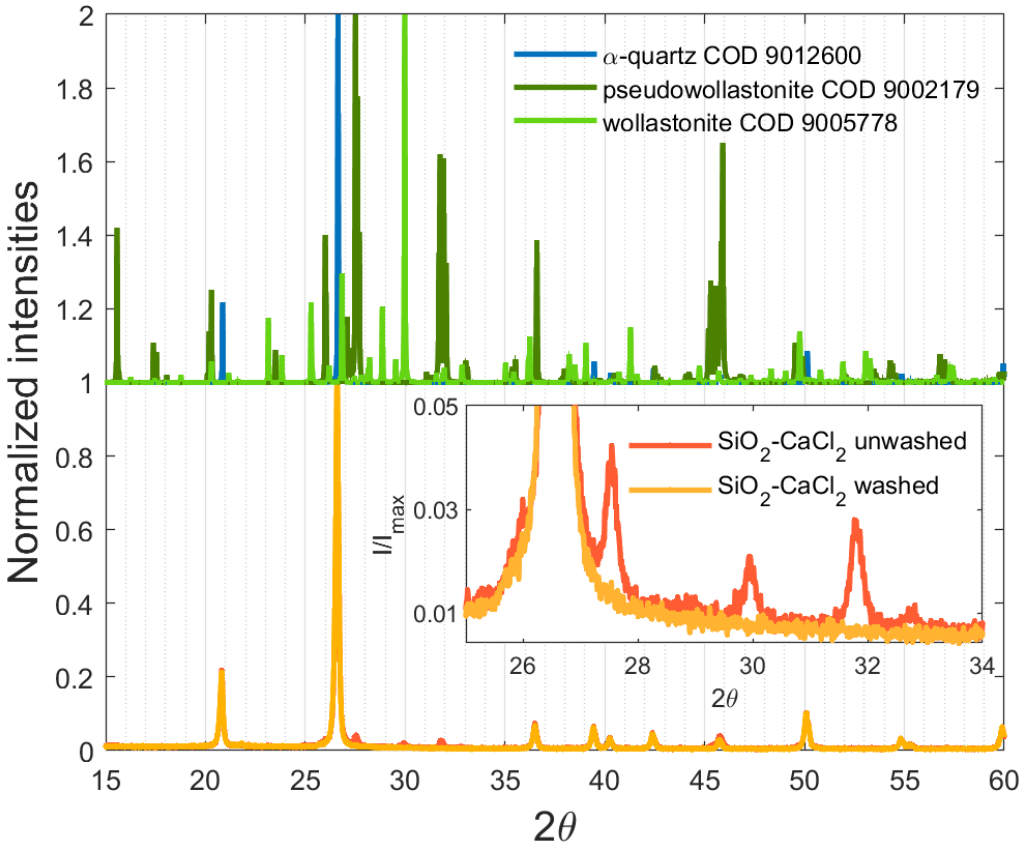

Figure 2.4.32 *X-ray powder diffraction patterns of calcinated SiO_2 with $CaCl_2$ before (red line) and after acid wash (orange line). Inset: zoom in 2theta range 25°-34°. Top: reference patterns for α-quartz (blue line) and $CaSiO_3$ pseudowollastonite and wollastonite polymorphs (green lines).*

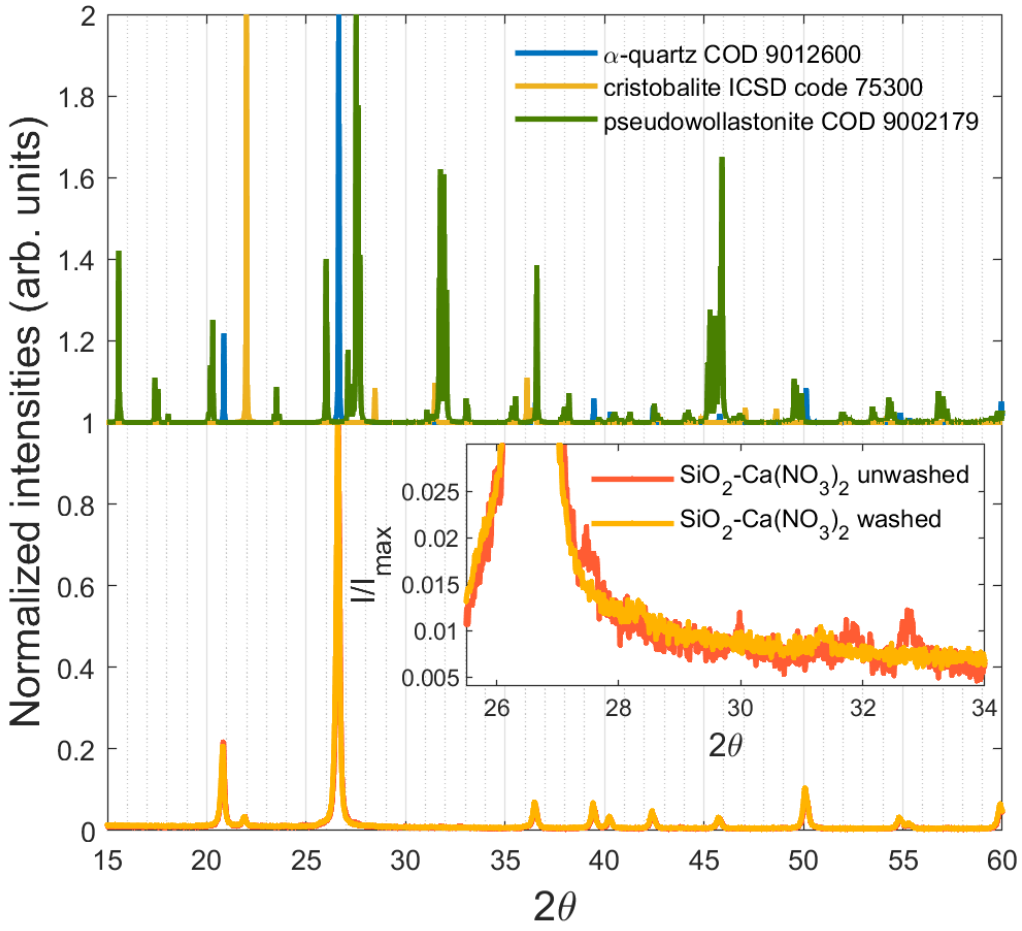

Figure 2.4.33 *X-ray powder diffraction patterns of calcinated SiO_2 with $Ca(NO_3)_2$ before (red line) and after acid wash (orange line). Inset: zoom in 2theta range 25°-34°. Top: reference patterns for α-quartz (blue line), cristobalite (yellow line) and $CaSiO_3$ pseudowollastonite (green line).*

	α-quartz	**cristobalite**	**Silicates**
SiO_2-$MgCl_2$ unwashed	96.8%	-	3.2% $MgSiO_3$
SiO_2-$MgCl_2$ washed	97.9%	-	2.1% $MgSiO_3$
SiO_2-$CaCl_2$ unwashed	90.4%	0.6%	5.9% pseudow., 3.1% woll.
SiO_2-$CaCl_2$ washed	99.7%	0.3%	-
SiO_2-$Ca(NO_3)_2$ unwashed	96.5%	2.1%	1.4% pseudowollastonite
SiO_2-$Ca(NO_3)_2$ washed	97.5%	2.3%	0.2% pseudowollastonite

Table 2.4.2 *Quantitative results of phase weight fraction from Rietveld refinement of PXRD pattern of different silica calcinated with salts before and after acid wash.*

From the calculated phase weight fractions, it is evident that the acid wash treatment of ICP spectroscopy allows to remove a considerable amount of silicates from the samples, particularly in case of Ca- salts, in which are almost absent. The very small phase fraction of cristobalite estimated in SiO_2-$CaCl_2$ system, combined with the deletion of $CaSiO_3$ silicates with washing, leads to obtain an almost absolute crystallization of silica in quartz, reaching a calculated weight percentage of 99.7%. In this way, it is thus possible to crystallize amorphous SiO_2 selectively in quartz polymorph by MIC with $CaCl_2$ following a quite simple calcination treatment.

As explained in Paragraph 2.2, industrial quartz synthesis is typically carried out via hydrothermal methods, which require high pressures and extended times (approximately 100 hours), as well as expensive equipment. However, these costs are offset by the production of large quantities of material. In a standard chemical laboratory, replicating this process is challenging and potentially hazardous due to the high pressures involved. Although the required temperatures are modest (around 400°C), the long processing times result in significant energy consumption, particularly when using a conventional muffle furnace. A more practical alternative involves melting silica (T > 1700°C) followed by slow cooling to enable the formation of quartz, the most stable phase at low temperatures. Nonetheless, this method is also time-consuming and costly.

As described in this work, the addition of salts—specifically $CaCl_2$—facilitates the production of high-purity quartz through heat treatments conducted at lower temperatures and within shorter times, thereby significantly reducing energy consumption. While a direct comparison with industrial methods is difficult due to differences in scale, optimizing this setup could render this approach highly promising.

SEM measurements were conducted on various alkaline-earth salts-silica samples, investigating the morphology and elemental composition as in the case of alkali salts. The Figure 2.4.34 shows a typical morphology observed for these samples, particularly the one related to $Ca(NO_3)_2$ - SiO_2 after thermal treatment.

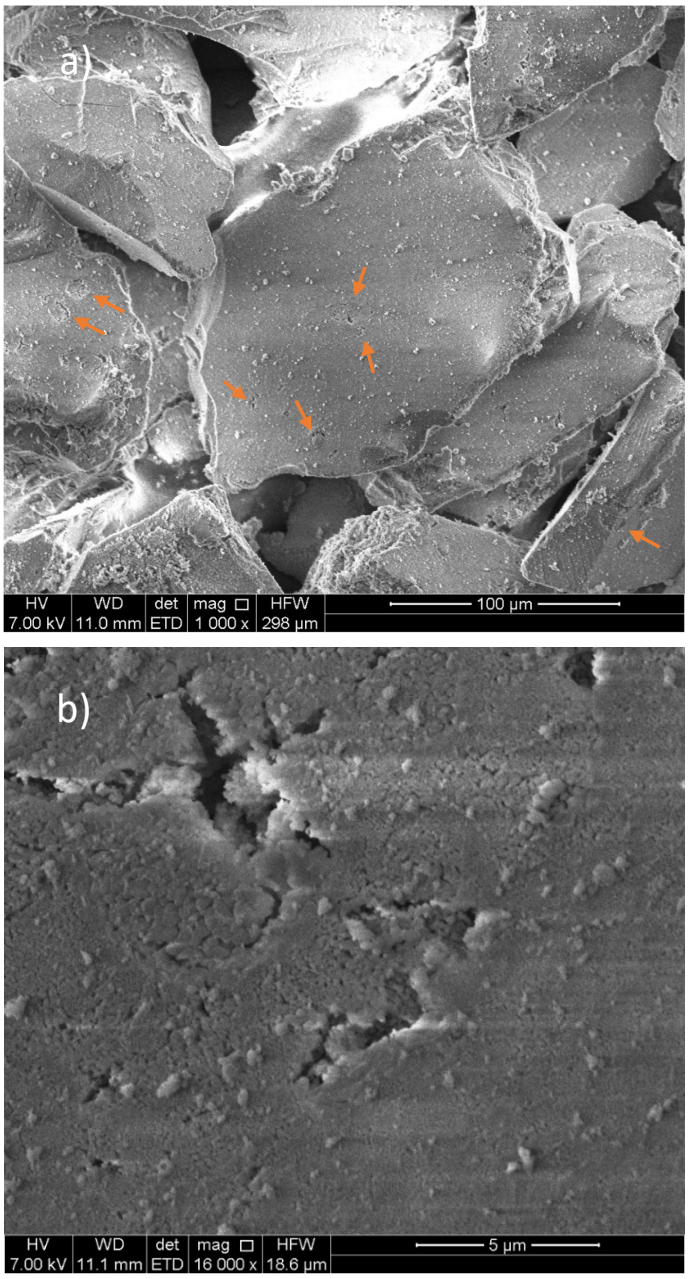

Figure 2.4.34 *$Ca(NO_3)_2$-SiO_2 sample morphologically analyzed by SEM. In a) cracks and holes are highlighted with orange arrows.*

Even at low magnification, cracks on the surface are visible, some with a semicircular shape as highlighted in the Figure 2.4.34a. In the image acquired on $CaCl_2$-SiO_2 sample (Figure 2.4.35), these formations are much more prominent, with the presence of actual small craters surrounded by concentric rings, more or less marked, across the surface.

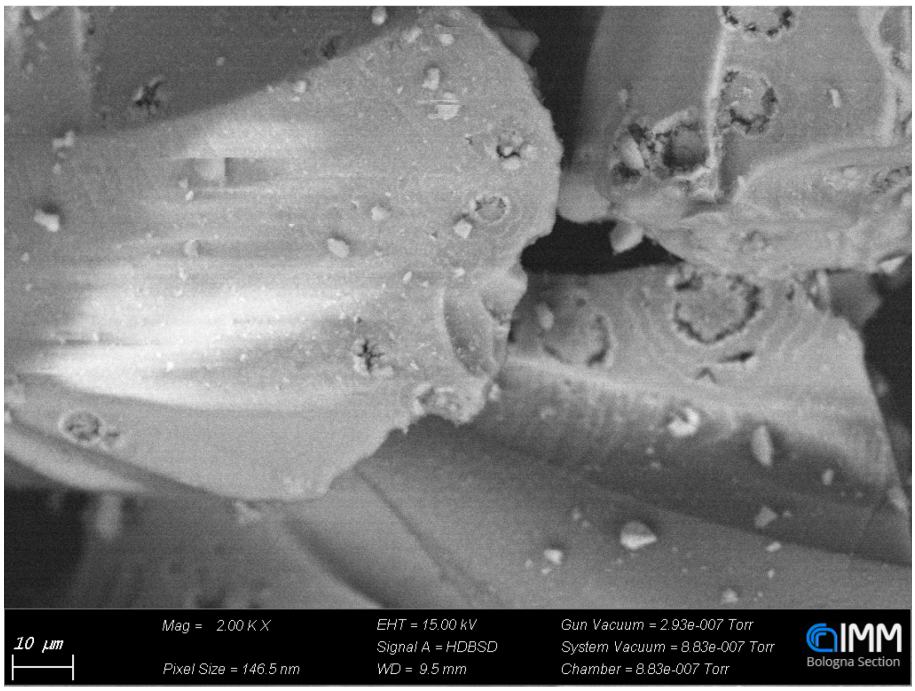

Figure 2.4.35 *$CaCl_2$-SiO_2 sample morphologically analyzed by SEM.*

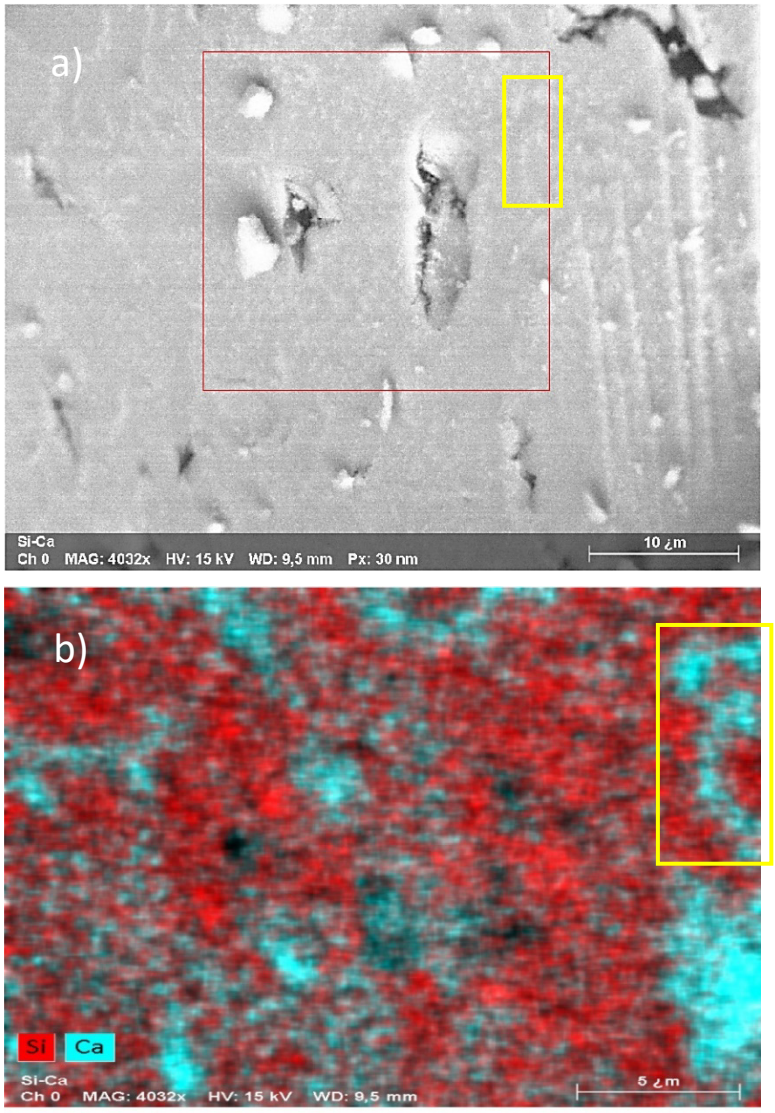

Figure 2.4.36 *EDX mapping of SiO_2-$CaCl_2$ sample. The marks on the surface of the sample coincide with areas of high calcium concentration (easily observable in the yellow box, highlighting the same area in a) and b)).*

EDX analysis indicates that these morphological features are attributable to the presence of the salt, which is not evenly distributed throughout the sample, contrarily to alkali salts, but instead forms localized high-concentration clusters.

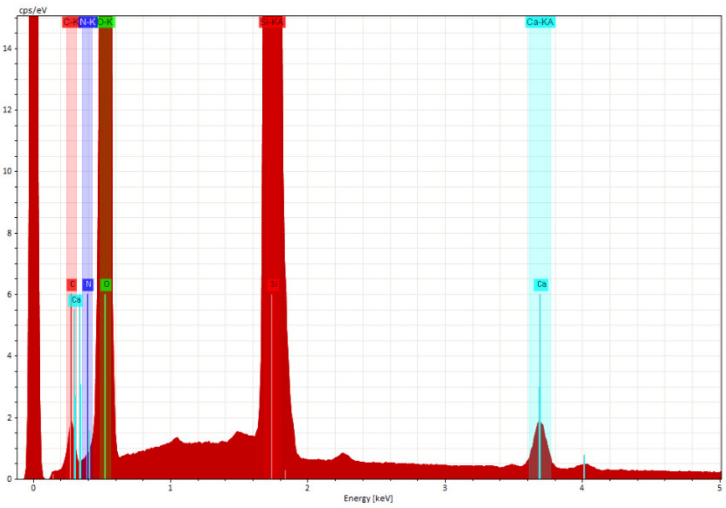

Element	At. No.	Line s.	Netto	Mass [%]	Mass Norm. [%]	Atom [%]	abs. error [%] (1 sigma)	abs. error [%] (2 sigma)	abs. error [%] (3 sigma)	rel. error [%] (1 sigma)	rel. error [%] (2 sigma)	rel. error [%] (3 sigma)
Carbon	6	K-Serie	20221	5,66	4,11	6,35	0,75	1,50	2,25	13,25	26,51	39,76
Nitrogen	7	K-Serie	7116	1,46	1,06	1,40	0,24	0,48	0,72	16,45	32,91	49,36
Oxygen	8	K-Serie	1095080	82,30	59,78	69,33	8,57	17,14	25,71	10,41	20,83	31,24
Silicon	14	K-Serie	1936685	46,57	33,82	22,35	1,96	3,91	5,87	4,20	8,40	12,60
Calcium	20	K-Serie	42731	1,70	1,23	0,57	0,08	0,15	0,23	4,50	8,99	13,49
			Sum	137,68	100,00	100,00						

Figure 2.4.37 *EDX quantitative analysis on SiO_2-$CaCl_2$ sample.*

A quantitative analysis was also performed (Figure 2.4.37), revealing the presence of 1.2% calcium in mass percentage. However, it should be noted that the material is not perfectly flat and is poorly conductive, which may lead to errors in the quantification of elements, such as the volume of primary excitation which is not confined to the surface but extends through the bulk for 1-5 µm depending on the type of material.

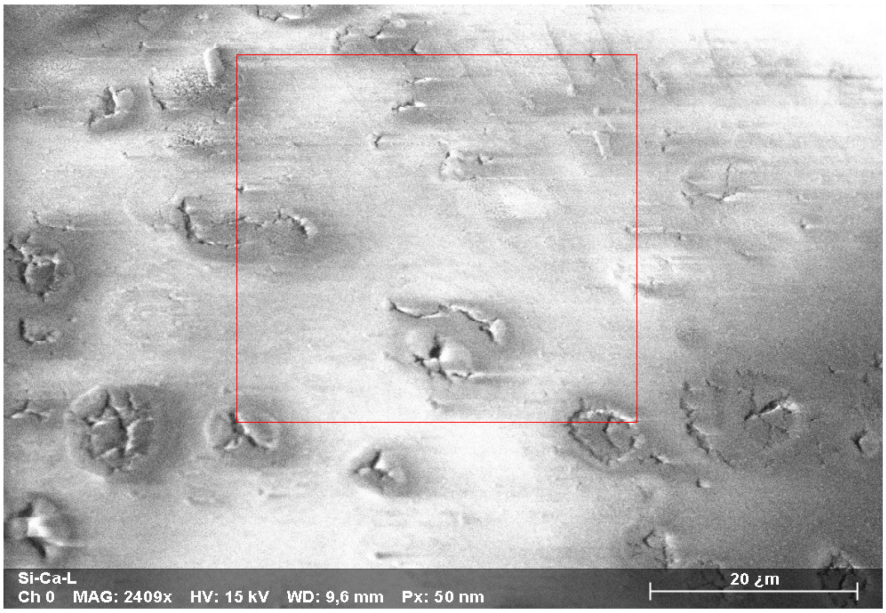

Element	At. No.	Line s.	Netto	Mass [%]	Mass Norm. [%]	Atom [%]	abs. error [%] (1 sigma)	abs. error [%] (2 sigma)	abs. error [%] (3 sigma)	rel. error [%] (1 sigma)	rel. error [%] (2 sigma)	rel. error [%] (3 sigma)
Carbon	6	K-Serie	51161	11,82	10,76	16,78	1,42	2,83	4,25	11,98	23,96	35,94
Nitrogen	7	K-Serie	6035	1,13	1,03	1,38	0,20	0,39	0,59	17,36	34,71	52,07
Oxygen	8	K-Serie	781388	50,16	45,70	53,49	5,27	10,54	15,80	10,50	21,00	31,51
Silicon	14	K-Serie	2810790	46,66	42,51	28,34	1,96	3,92	5,88	4,20	8,40	12,60
			Sum	109,76	100,00	100,00						

Figure 2.4.38 *Results of EDX quantitative analysis on SiO2-$CaCl_2$ sample after acid wash.*

After an acid wash (post-ICP analysis), this sample was reanalyzed with SEM. While morphology remained unchanged with observable holes and cracks (Figure 2.4.38), quantitative measurement no longer detected any calcium. This absence suggests that the calcium additive was likely situated in a superficial and weakly bound position within the sample, making it susceptible to removal by the acid wash process.

A quantitative analysis via EDX was also performed on the $MgCl_2$-SiO_2 sample, both before and after the acid wash (Figures 2.4.39 and 2.4.40).

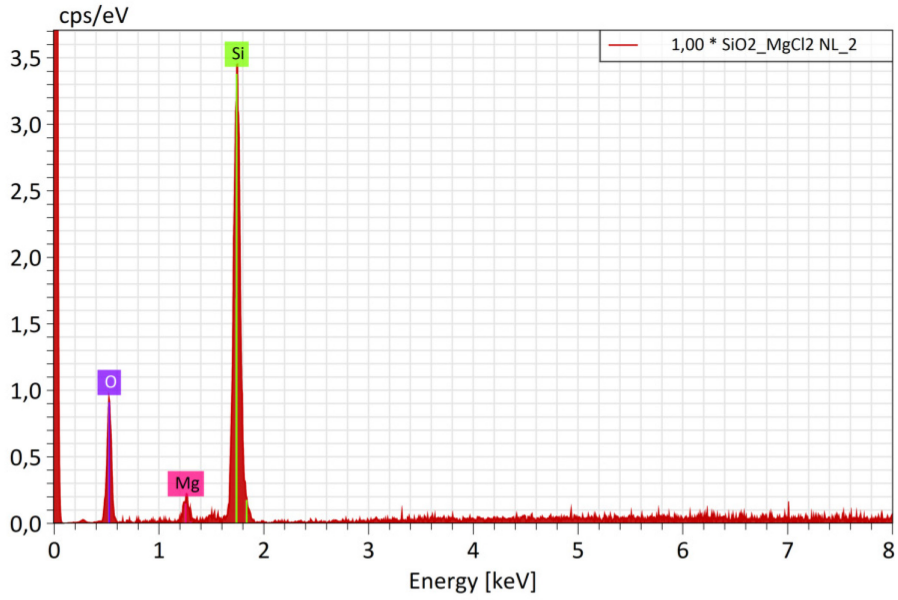

SiO2_MgCl2 NL_2

Element	At. No.	Line series	Net	Mass [%]	Mass Norm. [%]	Atom [%]	abs. error [mass%] (1 σ)	abs. error [mass%] (2 σ)
Silicon	14	K	7800	52,75	50,08	36,95	6,94	13,89
Oxygen	8	K	1323	48,79	46,32	59,98	2,79	5,57
Magnesium	12	K	330	3,79	3,60	3,07	0,67	1,33
			Sum	**105,34**	**100,00**	**100,00**		

Figure 2.4.39 *EDX quantitative analysis on SiO_2-$MgCl_2$ sample.*

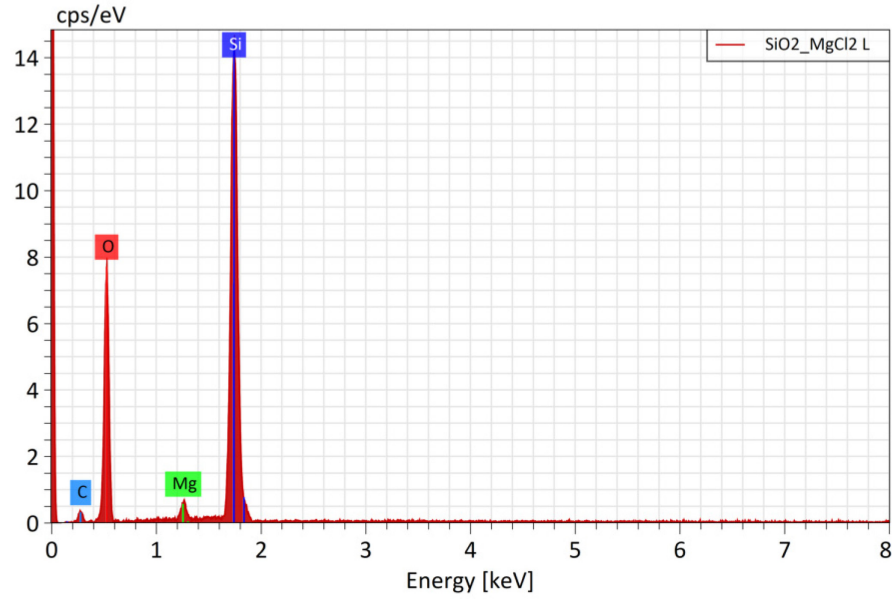

SiO2_MgCl2 L

Element	At. No.	Line series	Net	Mass [%]	Mass Norm. [%]	Atom [%]	abs. error [mass%] (1 σ)	abs. error [mass%] (2 σ)
Oxygen	8	K	11526	49,91	56,34	63,79	2,44	4,88
Silicon	14	K	34344	29,24	33,01	21,29	1,86	3,71
Carbon	6	K	419	8,11	9,15	13,81	0,64	1,28
Magnesium	12	K	944	1,33	1,50	1,12	0,13	0,26
			Sum	**88,59**	**100,00**	**100,00**		

Figure 2.4.40 *EDX quantitative analysis on SiO_2-$CaCl_2$ sample after acid wash.*

In this case, the presence of the metal is still detectable after processing, but its quantity decreases considerably, from approximately 3.8% to 1.3%.

As explained, the reported values cannot be considered entirely reliable, nevertheless a notable consistency is observed with the trends previously identified through quantitative measurements using the Rietveld method on PXRD patterns of the acid-washed samples (see Table 2.4.2). In both instances, the sample containing $CaCl_2$ shows the complete disappearance of calcium-containing phases, while that with $MgCl_2$ exhibits a significant reduction.

As seen, the samples containing salts of alkaline earth elements, especially in the case of calcium, show the presence of the cation only on the surface, and not diffused in the silica matrix, as in the case of alkali metals. SEM and EDX analyses confirm that the superficial calcium clusters are easily removable by acid washing, leaving the silica structure intact.

2.5 Conclusions on SiO_2 project

The optimization of industrial processes for material production, with a focus on reducing energy consumption and environmental impact, is fundamental for a sustainable future. In this context, crystallization, a key process in various industrial sectors, often requires high temperatures and significant energy input. This Ph.D. project investigates metal-induced crystallization (MIC) mechanisms as a promising, though not yet completely understood, method for obtaining crystalline materials at lower temperatures, leading to energy savings. In this study, silicon dioxide (SiO_2) was chosen as a model system to explore the mechanisms behind MIC. Silica, an abundant and versatile material, exists in various crystalline forms, each with unique properties and specific applications. Understanding the mechanisms driving the formation of different SiO_2 polymorphs is then of great fundamental and practical interest.

The experimental investigation involved impregnating amorphous SiO_2 with solutions of alkali (Li, Na, K, Rb, Cs) and alkaline-earth (Mg, Ca) metal salts in chloride or nitrate forms. The impregnated samples underwent thermal treatment at 1000°C for 4 hours, simulating an industrial calcination process. Structural analysis of the products using X-ray powder diffraction (PXRD) revealed substantial differences in the behavior of the two groups of metallic cations, with additional characterization techniques highlighting distinct aspects of these behavioral variations.

For samples containing alkali metals, crystallization products analyzed through PXRD showed the formation of mainly cristobalite and tridymite, two

high-temperature-stable SiO_2 polymorphs. Their presence at lower temperatures than typically required for formation from the amorphous precursor suggests a catalytic role of alkali cations in the process. Interestingly, diffraction patterns showed no peaks attributable to the starting salts in crystalline phase. This could be due to the transformation of the salts into an amorphous state during calcination, or to their incorporation into the SiO_2 structure. Rietveld analysis of PXRD patterns revealed an increase in the c lattice parameter of cristobalite and tridymite with increasing ionic radius of the alkali cation. This observation suggests that alkali cations, with their larger ionic radii, induce a distortion in the crystalline structure of SiO_2, leading to a stretching along the c-axis. Infrared spectroscopy provided further insights into the interaction between alkali cations and the silica lattice. Specifically, a shift to lower frequencies in the symmetric stretching band of Si-O-Si bonds was observed with increasing ionic radius of the alkali cation. This shift indicates a weakening of the Si-O-Si bond, likely due to the interaction between alkali cations and oxygen atoms in the silica lattice. Morphological and compositional analysis showed a uniform distribution of alkali cations within the silica matrix. This suggests that the alkali cations integrate into the SiO_2 structure during crystallization, supporting the hypothesis of a direct incorporation mechanism.

Moving to samples with alkaline earth metals, PXRD analysis revealed a substantial difference compared to alkali cations: alkaline earth cations predominantly promoted the formation of quartz, the thermodynamically stable SiO_2 phase at room temperature. This result suggests a crystallization mechanism distinct from that observed with alkali cations, where alkaline earth cations may act as catalysts without direct incorporation into the quartz structure. Rietveld analysis of PXRD patterns showed that the quartz weight fraction exceeded 90% in all samples, reaching a maximum of 96.8% in the SiO_2-$MgCl_2$ system. Small amounts of cristobalite were detected in certain samples, particularly with $Mg(NO_3)_2$ and $Ca(NO_3)_2$. Another significant difference from alkali cations was the formation of silicates as an intermediate phase during calcination. Diffraction peaks corresponding to $MgSiO_3$ (protoenstatite) and $CaSiO_3$ (wollastonite and pseudowollastonite) were observed in PXRD patterns. Quantitative analysis estimated that the total silicate formation was slightly higher in chloride-treated

samples than in those treated with nitrates. Inductively coupled plasma analysis, conducted after an acid wash to remove salts not incorporated into the SiO_2 structure, demonstrated that a significant portion of alkaline earth cations could be removed from the samples. This result supports the hypothesis that alkaline earth cations are not structurally incorporated into the final quartz but rather act as catalysts through intermediate silicate formation. Morphological analysis revealed cracks and holes on the surfaces of the samples. This feature has been associated, thought compositional analysis, with higher calcium concentrations, suggesting non-uniform salt distribution, forming localized aggregates.

Summarizing the experimental results, it has been pointed out that alkali cations play an active role in the crystallization of amorphous SiO_2, promoting cristobalite and tridymite formation at lower temperatures than those typically required to overcome high activation energies. The dependence of the c-lattice parameter increment on cation size, the shift to lower frequencies of the symmetric Si-O-Si stretching band, and the homogeneous distribution of these elements within the silica matrix provide evidence for the incorporation of alkali metal cations within the silica structure. This phenomenon likely underlies the crystallization of amorphous SiO_2 at temperatures otherwise impossible without the addition of these metal elements. On the contrary, the experiments conducted on alkaline earth cations suggest a possible two-phase crystallization mechanism: the metals react with SiO_2 to form intermediate silicates during calcination and subsequently these silicates promote quartz nucleation and growth. Unlike the phenomenon observed in alkali metals, alkaline earth cations are not incorporated into the final quartz structure and can be removed by acid washing. In this latter case a detailed understanding of the crystallization mechanism induced by alkaline earth cations opens new pathways for the controlled synthesis of high-purity quartz. In particular, the use of $CaCl_2$ followed by acid washing proved effective in obtaining quartz with a weight fraction of 99.7%, thus with a very high selectivity of the production of this polymorph. Analogously, it should be possible to find the proper conditions (i.e. type of cation and concentration, thermal treatment conditions, etc.) to obtain selectively also cristobalite and tridymite phases by metal induced crystallization, proposing alternative and low energy consuming processes also for the applicative point of view.

It can thus be stated that this study has successfully advanced comprehension of the crystallization mechanism of amorphous silica induced by metal use. However, further and possibly decisive steps are required to fully elucidate this process, specifically in understanding the chemical processes enabling metals to catalyze crystallization. Additional analyses and data are necessary to establish a complete and accurate model.

In this framework, a study has been proposed on SiO_2 crystallized powders via MIC at 1000°C-4h with KCl, RbCl, and $CaCl_2$ salts (1M saline solution) using X-ray Absorption Fine-structure Spectroscopy (XAFS) at the XAFS beamline of Elettra Synchrotron (Trieste, Italy) (proposal n. 20245278, accepted and scheduled in February 2025). XAS is a powerful technique providing critical insights into local structural distortions, making it highly complementary to XRD, which primarily reveals long-range structural order. While XRD alone can provide valuable information on the average structure, it lacks the sensitivity to detect subtle local changes in atomic environments. XAS, by contrast, is especially suitable for probing these local distortions, making it essential to fully understand the mechanisms underlying metal-induced crystallization in SiO_2. Particularly, this technique will be able to observe the coordination of cation with silica oxygens, expected to be distinct compared to their original coordination in salts in the case of a cation occupancy of SiO_2 cavities. Furthermore, in situ XAFS measurements are proposed as a function of temperature to replicate the calcination process of SiO_2 with RbCl. This approach aims to monitor the thermal evolution of Rb coordination, transitioning from its initial salt form to its final arrangement within the SiO_2 polymorph. The use of this local technique will be crucial to unravel the complex mechanism behind metal-induced crystallization.

3 Studies on direct synthesis of nanostructured metals at the Hall-Petch limit

3.1 Nanostructured materials. Why should we care?

Nowadays nanostructured materials represent one of the most advanced topics in materials science. The notable academic and innovative technological interest surrounding them is driven by their unique electronic[60], thermoelectric[61], magnetic[62], optical[63], chemical[64], thermodynamic[65], and mechanical properties[66], which significantly distinguish them from their macroscopic counterparts.

A nanomaterial is defined as a material with any external dimension in the nanoscale or having internal structure or surface structure in the nanoscale, thus with a length range approximately from 1 nm to 100 nm. Many examples of nanomaterials can be found in nature, both in inorganic compounds, such as the naturally photonic opal crystals, and in biological and organic systems, like the "spatulae" on the bottom of gecko feet, colloids such as blood, corals, etc. Learning from natural systems, scientists have demonstrated for several decades the possibility to synthesize, engineer, and manufacture many kinds of nanomaterials.

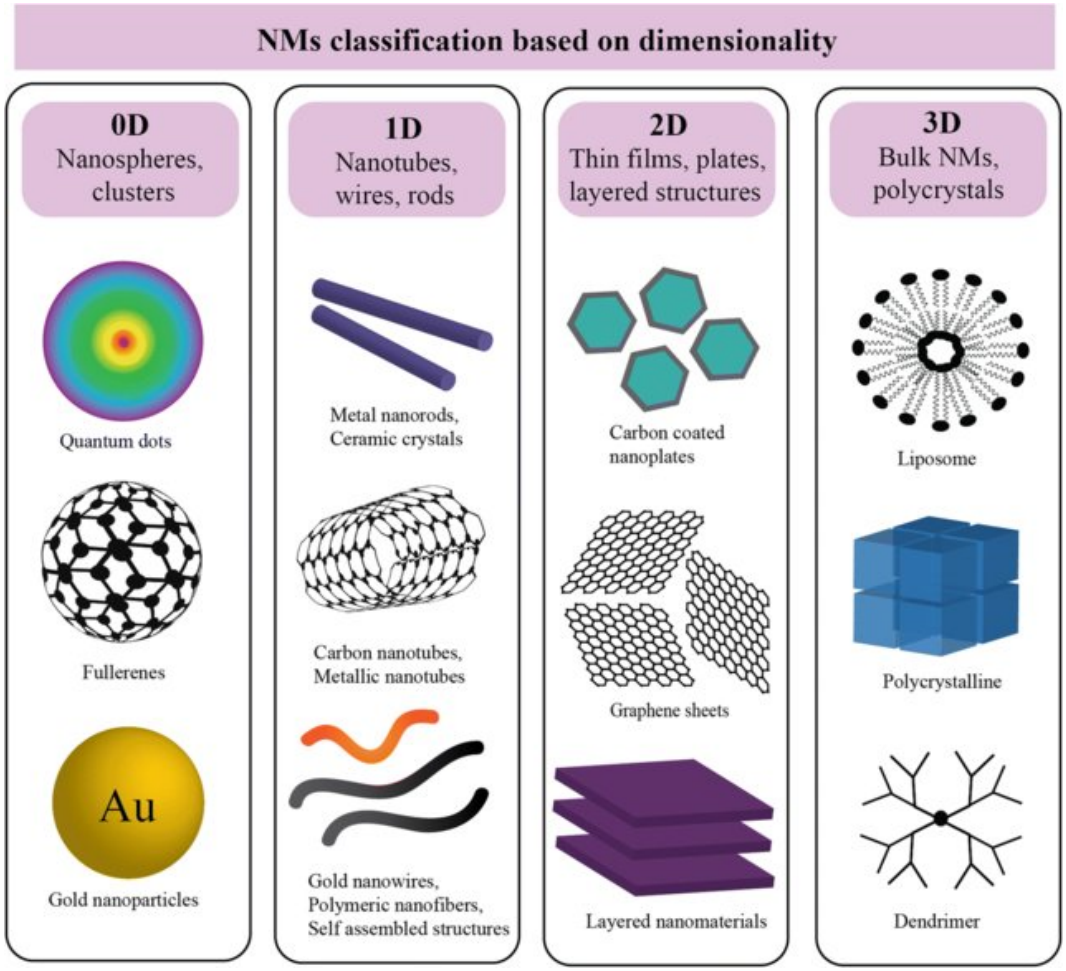

Figure 3.1.1 *Nanomaterials classification based on dimensionality*[67].

Considering how many of their dimensions fall into the nanoscale, it is possible to classify different types of nanostructures. Specifically, if a nano-object has one, two, or all three external dimensions in the nanoscale, it is defined as a nanosheet, a nanofiber, or a nanoparticle, respectively. These elements can be arranged in nanostructured materials such as nanocomposites, nanofoam, nanoporous materials, or nanocrystalline materials, the latter characterized by a significant fraction of crystal grains in the nanoscale[68,69].

The peculiar physical and chemical properties of nanostructures constitute the result of their particular atomic arrangement. Contrarily to macroscopic matter, nanoscale materials are characterized by a high surface-to-volume ratio, which means that a significant number of atoms are located on the surface rather than in the bulk and display consequently an increased surface energy. These features alter, for instance, their thermodynamical properties, responsible of the melting-point

decreasing often observed in nanoparticles[70,71]. Moreover, the exposure of a large amount of atoms on the surface can enhance the catalytic activity of such materials by increasing the probability of interacting with reactants[72].

Additionally, in nanomaterials atomic interactions can display significant changes which can result in deviation from the periodic atomic arrangement of their bulk counterparts due to the dominance of surface dangling bonds, defects, and dislocations[73]. This leads to improvements in mechanical properties, such as the hardness in nanocomposites[74], or the decreasing of electrical conductivity[75]. This latter mechanism is also associated with quantum confinement effects[76]. At the nanoscale, the dimensions of materials can approach near the de Broglie wavelength of electrons[77], leading to the formation of discrete energy levels, which alter electronic, optical, and magnetic properties. For instance, quantum dots exhibit size-dependent optical properties because the bandgap energy increases by decreasing the particle size[78].

Such exotic properties emerge in materials characterized by a length-scale below a critical dimension, which is generally on the order of tens or a few hundred nanometers, with the exact value being specific to the property in question and the material studied. Nanometric-scale phenomena such as plasmonic resonances, photoluminescence of quantum dots, stabilization of exotic phases under ambient conditions, increased surface reactivity, and interactions with biological systems have led to the widespread use of nanomaterials across various research fields and applications, including optics[79,80], photonics[81,82], sensing[83,84], drug delivery[85,86], and catalysis[87,88].

Regarding nanocrystalline metals, among the most relevant and directly applicable properties are increased hardness, tensile strength, fatigue resistance, and self-healing.

3.1.1 Increased strength of nanocrystalline metals

Mechanical properties constitute a crucial fingerprint of nanomaterials, among the most critical attributes in technological applications, although they are frequently underemphasized or dismissed as "non-functional". Instead, enhanced mechanical properties affect directly their performance and applicability, but also the effective efficiency of the overall manufacturing process. Specifically, they could enable the reduction of device weight, facilitating novel applications such as flexible electronics for neural implants and wearable fabrics. Improved mechanical performance contributes also to greater energy efficiency during production—requiring less material for equivalent functionality—and reduces energy consumption in transportation. Furthermore, superior mechanical properties lead to decreased wear, lower failure rates, and reduced friction[89], the latter of which accounts for approximately 30% of global energy.

The previous discussion is valid for nanomaterials in general, but it is even more applicable to metals, which dominate structural applications precisely because of their mechanical properties. The exceptional machinability of metals, which enables reproducible processes and uniform properties, their mechanical strength, their plasticity over a wide temperature range, and their durability are just a few of the attributes that have made metals indispensable in numerous sectors and ubiquitous in the modern world. Nanostructured metals have shown improvements in mechanical properties from 30% to 200% beyond existing conventional products[90]. These considerations highlight the importance of optimising promising high-performance mechanical nanomaterials, paving the way for novel applications and advanced technologies.

The superior mechanical properties of nanostructured metals can largely be explained by the Hall-Petch model, which attributes hardening to the high number of grain boundaries and the absence of defects[91,92]. In coarse-grained metals, ductility is due to the presence of dislocations—one-dimensional defects that can slip within the grains under sufficient force, thereby facilitating plastic deformation in the metal. According to the Hall-Petch model, grain boundaries act as barriers to dislocation motion. Specifically, a grain boundary is a type of homo-phase interface

that separates crystals of the same composition but different orientations. As the size of crystallites in a polycrystalline metal decreases, the volumetric fraction of grain boundaries increases, which limits dislocation movement, thereby reducing ductility and increasing hardness. Therefore, there is an inverse proportionality between the yield stress (i.e., the load or stress required to induce plastic deformation in the metal) and the square root of the grain size, as described by the Hall-Petch equation:

$$\sigma_y = \sigma_0 + kD^{-1/2} \tag{3}$$

where σ_y is the yield stress, σ_0 is a material constant for the starting stress for dislocation movement (or the resistance of the lattice to dislocation motion), k is the strengthening coefficient proper of the material, and D is the average grain diameter.

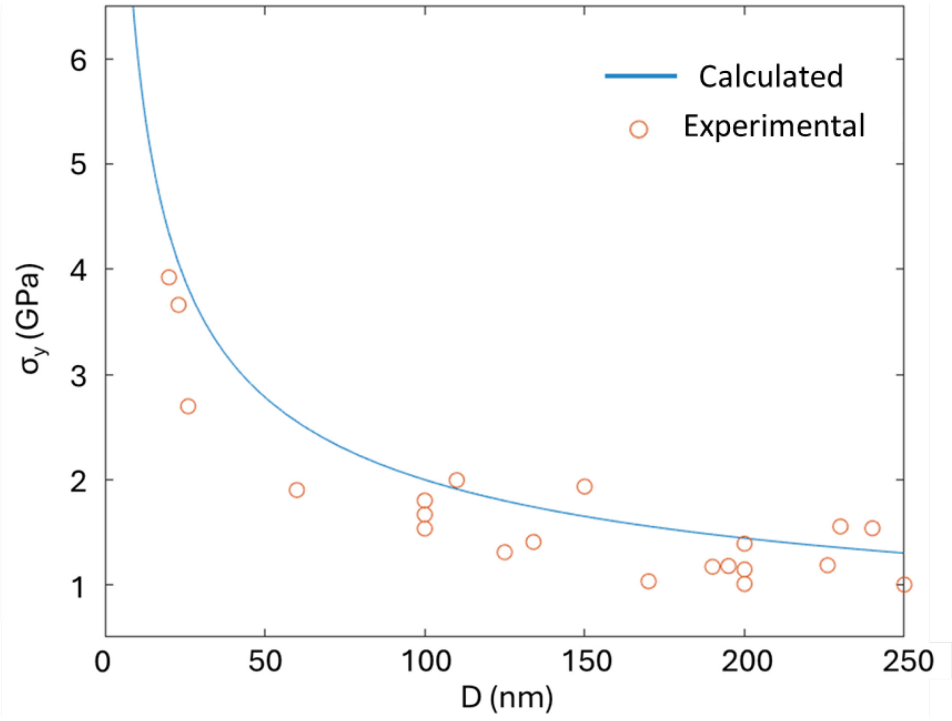

Figure 3.1.2 *Graphical representation of Hall-Petch equation for iron. Experimental data from Dangwal et al.[93] and calculation from Takeda et al.[94].*

Figure 3.1.2 shows the experimental and calculated trend of iron nanoparticle yield stress as a function of its nanometric grain size. This example illustrates how Equation (3) diverges as grain size decreases, leading to two notable consequences. Firstly, the benefits of Hall-Petch hardening increase progressively with further grain refinement. For example, reducing the grain size of iron from 50 nm to 25 nm results in approximately a 40% increase in hardness, whereas decreasing the grain size from 15 nm to 14 nm improves the properties by 3.5%. These represent significant improvements for such minor structural variations. A second observation regards the divergency to zero, particularly it is evident that this regime cannot be sustained indefinitely. In fact, the Hall-Petch relationship has been extensively verified experimentally on micro- or nanocrystalline metals to grains of about 10 nm in size. However, significant deviations from the Hall-Petch equation seem to occur as grain size below 10 nm; some studies indicate a possible saturation value for the yield stress reaching a plateau trend[95], while other works suggest a reversal Hall-Petch tendency[96]. This spatial limit has prompted the scientific community to address this fundamental issue of what happens to the mechanical properties below 10 nm, still considered an open question.

Certainly, at such small dimensions the contribution of grain boundaries effects cannot be neglected. Besides, manufacturing nanostructured metals with uniform grain size and shape below 10 nm is extremely challenging due to the very high grain boundary energy in metals. Grain uniformity is essential for understanding mechanical properties because these properties are collective attributes of the material's microstructure: in other words, the distribution of grain sizes is more significant than their average value. In this framework, Hall-Petch deviations could possibly be due to a plastic deformation on grain boundaries or linked to a lack of non-thermodynamic detects in nanocrystalline materials, thanks to their slow-growing rate with respect to their dimensions[97].

Another characteristic of nanocrystalline materials which must be considered to understand properly their potential applications, besides the dominant presence of grain boundaries, is their thermal stability. In this regard, it has been shown that the unique mechanical properties of nanomaterials significantly decrease where thermal-induced mechanical instability occurred[98]. The reason for

this tendency is the excess of nanomaterials' Gibbs free energy, which makes them susceptible to thermal activation or other effects that can drive them back towards equilibrium. Therefore, thermodynamics promotes grain growth and, accordingly, the gradual elimination of the very microstructural features responsible for the superior mechanical properties of nanostructured metals[99]. An increase in temperature, by promoting homogenization and the removal of non-equilibrium features, leads to the loss of the nanostructure and the associated properties, rendering nanomaterials unsuitable for high-temperature applications and potentially less stable over time. Despite some possible solutions that have been explored to stabilize thermally nanostructures by thermodynamic or kinetic approaches[100,101] or by microstructural architectures[102], nanostructured metals are in principle more suitable for low-temperature applications. This condition leads to different processing methods for these materials, as, for instance, they cannot be welded, but rather be formed into their final shape through low-temperature processes. However, some studies suggest that their workability and formability are greater than those of conventional metals, thereby reducing production costs and the risk of failures during manufacturing[90,103].

3.1.2 Synthesis methods of nanocrystalline metals

The production of nanocrystalline metals with increasingly smaller grain sizes is therefore not only a scientifically significant goal for studying fundamental issues such as the inverse Hall-Petch effect, but also a desirable technology due to the potential to strengthen metals solely through control over their microstructure.

The synthesis of nanostructured metals has therefore been pursued by materials scientists so far, leading to the development of various methods, which, according to the conventions and terminology of nanoscience, are categorized as top-down and bottom-up approaches[104,105].

Top-down methods start with a microcrystalline metal and involve refining the grain size to the nanometric scale through severe plastic deformations. These

methods include ball milling (mechanical alloying)[106], extrusion (equal channel angular extrusion)[107], and the application of high-pressure torsion[108].

Bottom-up methods use simple starting materials such as atoms, ions, or small molecules, and involve assembling them into extended materials through deposition techniques. These methods include: physical vapor deposition (PVD)[109], which involves the physical deposition of atoms or molecules from a vaporized source onto a substrate in a vacuum; chemical vapor deposition (CVD)[110], that uses chemical reactions in the gas phase to deposit thin films onto a substrate; electrodeposition[111], which requires an electric current to deposit metal ions from a solution onto a conductive substrate, forming a thin film; molecular beam epitaxy (MBE)[112], an advanced technique for growing thin films with high precision and control over the crystal structure; pulsed electron deposition (PED)[113], a physical vapor deposition technique that uses a pulsed laser to ablate a target material, creating a plasma of atoms or ions that are deposited onto a substrate. Each of these techniques provides different control over the film's thickness, composition, and microstructure, making them suitable for various applications in electronics, coatings, and advanced materials.

Once nanometals have been synthesised, both with top-down or bottom-up approaches, powder metallurgic methods like sintering[114], liquid phase sintering[115], and hot isostatic pressing[116], which can be employed to promote grain growth in specific applications.

The synthesis methods for nanocrystalline metals that are most extensively studied are top-down methods, as they offer the advantage of producing relatively large quantities of material, sufficient for direct mechanical testing such as tensile and indentation tests. Despite this significant advantage, plastic deformation-based methods have the limitation of not being able to refine grain sizes significantly below the upper limit of nanocrystallinity (~100 nm), thereby limiting the potential of Hall-Petch strengthening. Additionally, these methods require substantial energy expenditure and impart high strain to the metal, which reduces its fatigue resistance. Among top-down methods, ball milling allows for the greatest grain refinement (<50 nm). However, the main limitation, apart from the inherent danger of creating

pyrophoric nanocrystalline powders, is the need to compact and densify the powders. Powder densification is a limiting factor because mechanical properties degrade rapidly with increasing residual porosity, and techniques used to increase density, such as compression or sintering, promote grain growth, thus negating the advantage of starting with very fine powders[117]. One approach used to limit grain growth during sintering is the use of immiscible metal alloys, which prevents the production of pure metals.

In contrast, bottom-up methods have the advantage of potentially producing nanocrystalline materials with very small grain sizes (<20 nm) and controlling their size by varying synthesis conditions. These methods create materials free of strain that do not require densification, but their application is limited by scalability, as they typically produce small quantities of material, insufficient for large-scale applications.

3.2 Iron-based nanomaterials

One of the most widely used metals in mechanical applications is constituted by iron. In fact, iron is one of the most abundant elements on Earth, making up about 5% of the Earth's crust by weight. This abundance, combined with its widespread availability in the form of iron ores like hematite and magnetite, makes iron a crucial resource for various industrial applications. Its plentiful supply ensures that iron is both cost-effective and readily accessible, which has contributed to its extensive use in the construction, automotive, and manufacturing industries, particularly for mechanical applications. In its bulk form, iron is the foundation of numerous structural components, such as beams, machinery, and automotive parts, where its high tensile strength and durability are essential. In its nanostructural form, iron exhibits unique properties, including enhanced magnetic behaviour for applicability in data storage and actuators, increased surface reactivity, and improved mechanical strength. These properties make iron nanoparticles valuable in advanced applications, such as in the development of high-performance magnetic materials[118], catalysts[119], and sensors[120]. Moreover, they have been demonstrated to

be highly valuable in protective coatings as iron nanofilms, where durability and resistance to corrosion and abrasion are critical[121]. In addition to their mechanical robustness, iron-based nanofilms are also used in microelectromechanical systems (MEMS)[122] and nanoelectromechanical systems (NEMS)[123], where their precise thickness control and high strength-to-weight ratio are essential for the miniaturization and performance of devices.

Iron nanofilms are synthesized using mainly bottom-up approaches, such as PVD[124], CVD[125,126], and electrodeposition[127].

3.2.1 Chemical Vapor Deposition for iron thin films

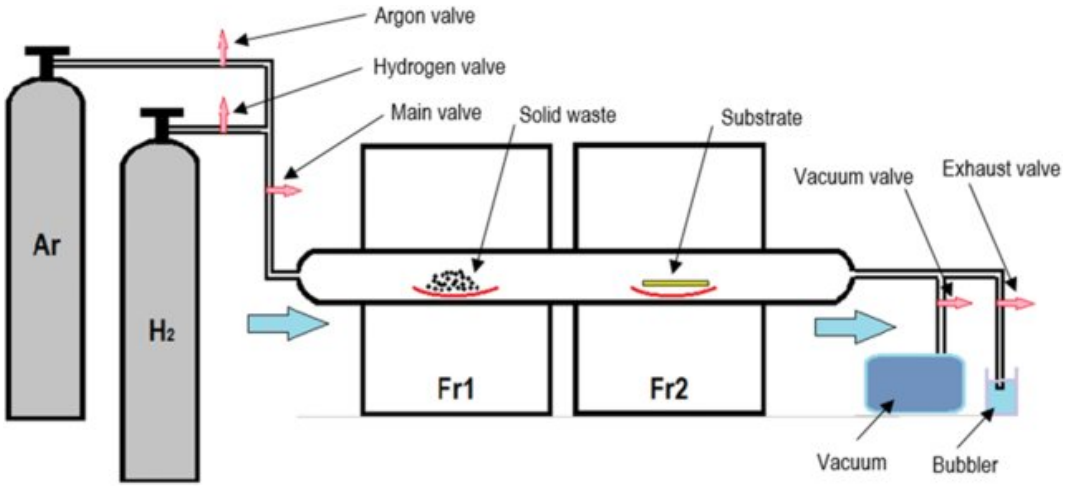

Figure 3.2.1 *Chemical Vapor Deposition schematic chamber process*[128].

In CVD processes, schematically reproduced in Figure 3.2.1, iron-containing gaseous precursors are introduced into a reaction chamber where they decompose and deposit onto a substrate to form iron nanofilms from iron pentacarbonyl[129]. This method allows for precise control over film composition and structure and is suitable for producing high-quality films over large areas. Specifically, it enables the production of nanocrystals with very small dimensions

(~15 nm), whose growth can be precisely controlled through the precursor mass flux and the reaction chamber temperature. Additionally, this method directly produces materials that do not require further densification, as the nanostructured surfaces exhibit high reactivity, ensuring rapid and uniform growth across the entire exposed area.

3.3 Experimental idea on “bulk” Fe-nanofilms

From the previous discussion, it is evident that the use of nanomaterials, specifically metal ones, instead of the same type but in bulk structures holds significant potential for enhancing both the efficiency and performance of equal applications, such as the mechanical sector. As described, nanomaterials can enable higher throughput, lower energy consumption, and greater precision in these processes, thereby pushing the boundaries of current technological capabilities.

Merging the large-scale applications of bulk structures with the high performance of nanomaterials, particularly nanometals, could represent a significant advancement in the mechanical sector. This integration could combine the structural robustness and cost-effectiveness of bulk materials with the superior mechanical, electrical, and thermal properties of nanomaterials. Such a synergy would enable the development of next-generation technologies that are both highly efficient and durable, leading to substantial improvements in performance, durability, and overall technological capability within the mechanical industry.

In this framework, this PhD Thesis presents a new synthetic set-up, analogous to the previously described CVD method, developed with the aim to obtain a massive quantity of nanocrystalline iron, with the smaller dimension possible of the grains, merging in this way the bulk and nanoscale benefits.

Iron pentacarbonyl $Fe(CO)_5$ has been selected as iron precursor for this synthesis process, due to its ability to provide zero-valent iron and its clean, quantitative decomposition, which is ideal for producing high-purity elemental iron

and low-carbon steels. Its high volatility and low decomposition temperature also reduce the energy consumption associated with its vaporization, gas-phase transport, and decomposition, allowing to produce iron materials at lower temperatures (the iron and steel industry is the highest energy-consuming manufacturing sector worldwide)[130].

Although the technology for producing nanocrystalline powders[131] and nanostructured iron thin films[129] has been well-developed and explored, there are currently no attempts in the literature to apply these fabrication technologies beyond nanoparticles and 2D materials to produce "bulk" nanocrystalline iron.

3.4 Materials and methods

This thesis work focuses on the synthesis and characterization of nanostructured iron, aiming to obtain bulk samples with grain sizes approximately 10 nm in order to study their mechanical properties.

All reagents and solvents were obtained from commercial sources (Sigma-Aldrich) and were used without further purification. The reagents employed are specified here below. Particularly, 1-odecene (technical grade, 70% purity) and oleylamine (technical grade, 70% purity) were initially used as solvent and ligand, respectively. It was hypothesized that oleylamine would coordinate to the surface of the iron, limiting grain growth and facilitating the formation of a dense and uniform structure. Iron pentacarbonyl ($Fe(CO)_5$ - reagent grade, > 99% purity) was used as the precursor for iron deposition. This choice was made due to its ability to decompose cleanly and quantitatively, producing high-purity elemental iron.

3.4.1 Home-made experimental synthesis set-up

The synthesis of the samples was conducted using chemical vapor deposition (CVD) of an organometallic precursor, employing a decomposition reaction at ambient pressure within a self-fabricated reactor.

$$Fe(CO)_5\ (g) \quad \rightarrow \quad Fe\ +\ 5\,CO\ (g)$$

where iron pentacarbonyl $Fe(CO)_5$ is the organometallic precursor and carbon monoxide CO is the reaction byproduct.

The experimental setup was modified and optimized throughout the course of the research. Initially, a radiatively heated deposition chamber was used, connected to a flask containing the reagent mixture. Subsequently, a system was developed with a separate evaporation chamber and a heated tubular reactor for the decomposition of the precursor.

The purpose of these modifications was to optimize the reaction conditions, particularly by adjusting three parameters, such as:

- The temperature of the deposition chamber to facilitate the decomposition of iron pentacarbonyl and limit side reactions that lead to the formation of carbides;
- The deposition rate, regulated to allow complete desolvation of iron pentacarbonyl and prevent solvent inclusion in the deposition;
- The flow of inert gas, utilized to promote the evaporation of iron pentacarbonyl at room temperature and transport it to the decomposition chamber.

Details regarding the specific modifications are outlined below:

- **Setup 1**: The reaction setup consists of a three-neck flask connected via standard tubes and adapters to a Schlenk line for nitrogen inlet and to a bubbler at the outlet, which acts as a trap for effluent gases particularly for any outgoing carbonyl compounds. The central neck of the flask is

equipped with a custom-built deposition chamber, which is heated radiatively by a 24-volt halogen lamp with a reflector. The deposition chamber is composed of a glass tube sealed at one end and fitted with a ground glass joint at the other, allowing it to be inserted into the main neck of the reaction flask. The upper portion of the deposition chamber is shielded with aluminum foil to reduce radiative heat transfer, thereby lowering the maximum temperature of the system. Inside the deposition chamber, a 1 cm x 1 cm microscope slide, cut to size, is mounted on a metal support and serves as the substrate for deposition.

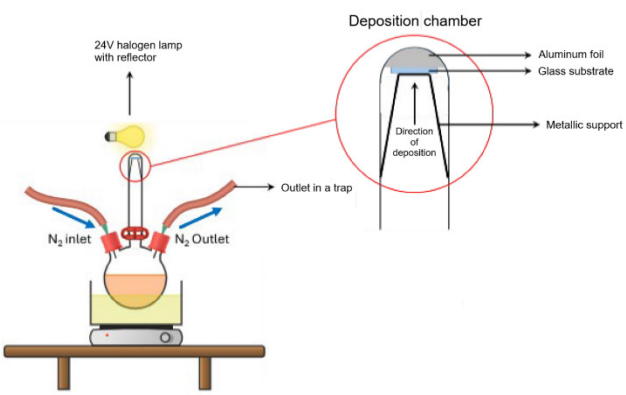

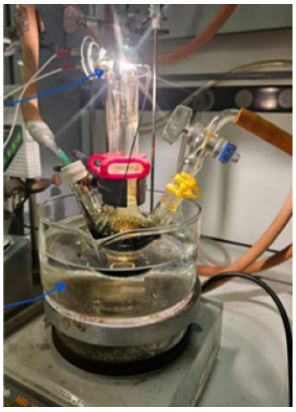

- **Setup 2**: A similar set-up has been developed, consisting of a deposition chamber equipped with two glass adapter tubes at the top, allowing them to be connected via two additional rubber hoses, respect with **setup 1**, to the Schlenk line, creating a nitrogen flow within the chamber. The chamber is mounted into the main neck of the flask using a standard ground glass joint. The heating process is performed by radiative heat as in **setup 1**.

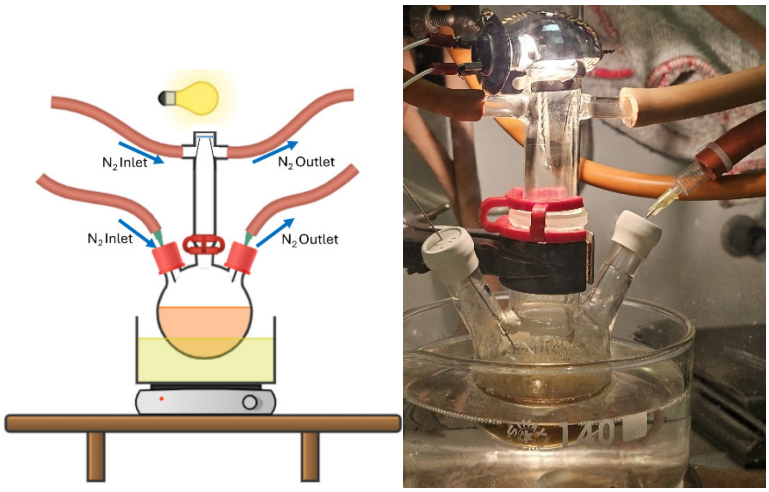

- **Setup 3**: The reaction chamber has been reduced in size, with the substrate closer to the reagents. The set-up apertures are two as in **setup 1**, with the same heater.

- **Setup 4**: In this case, a thermal lance has been used as a heating element in place of the bulb, in order to evaluate the impact of the heater. The test tube is thus directly heated. No reagent flasks are present, as the reagent is placed in a syringe which pumps it into the test tube.

- **Setup 5**: The setup consists of a reagent reservoir made up of a 10 mL vial sealed with a septum, and a tubular reactor heated by a thermal lance (as in **setup 4**). The tubular reactor is composed of a glass tube, sealed at one end with a rubber septum, and connected via standard fittings to the bubbler. The connection between the reagent reservoir and the tubular reactor is established by puncturing both septa with a Teflon cannula fitted with needles.

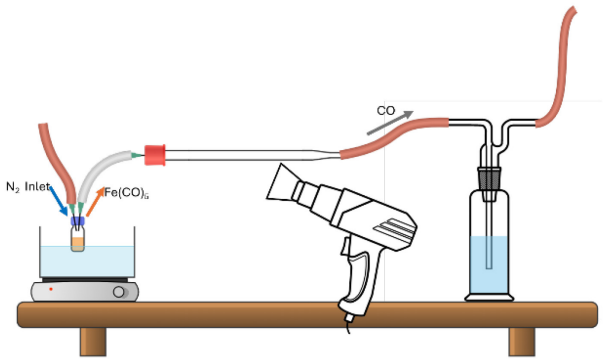

The differences between all the designed experimental setups have been considered in order to evaluate the contribution of all the elements involved in the synthesis, such as the heating element, the shape of the reaction chamber, and possible contaminations.

3.4.2 Characterization techniques

The materials were characterized using X-ray Diffraction (XRD), employed to identify the materials obtained from the syntheses and to estimate the crystalline grain size by applying the Scherrer equation to the main iron peak, and Scanning Electron Microscopy (SEM), to observe the morphology of the deposited material and with Energy-Dispersive X-ray Spectroscopy (EDX) mode for elemental analysis and semi-quantitative composition estimation of the material (for further details on the technique, see Paragraph 2.3).

3.4.3 Consideration on employed methods

In this study, the size of the crystalline grains D was estimated from the diffraction pattern by applying the Scherrer equation to the main peak of iron. The Scherrer equation is expressed as follows:

$$D = \frac{k\lambda}{\beta \cos(\theta)} \tag{4}$$

where λ is the X-ray wavelength, β is the full width at half maximum (FWHM) as the peak width, θ is the diffraction angle, and k is a dimensionless constant known as the Scherrer constant. The value of the Scherrer constant depends on several factors, including the definition of peak width, the *hkl* indices of the reflection considered, the shape of the crystallites, and the distribution of their sizes[129], but the standard value k = 0.9 constitutes a good approximation[132]. Although vapor-phase deposition may promote grain growth along a preferential direction and nanocrystals may exhibit a morphology distinct from their macroscopic counterparts, this was considered an acceptable approximation in the

absence of additional information regarding the shape and size distribution of the crystallites.

A semi-quantitative analysis of the phases was performed by applying the Reference Intensity Ratio (RIR) method to the XRD pattern. The RIR method involves reducing all factors that contribute to the intensity of the XRD peaks of a phase (scaling factor, density, linear attenuation coefficient) to a constant, except for concentration, by comparison with a reference phase, corundum. The ratio of the intensity of the phase considered (I) to the intensity of corundum (I_C) is given by:

$$I/I_C = \frac{\mu\gamma\rho_C}{\gamma_C\mu_C\rho} \tag{5}$$

where μ is the linear attenuation coefficient, γ is the absolute scaling factor, ρ is the density of the phase, and the subscript C refers to corundum. The values of I/I_C can be determined experimentally or calculated from cell parameters obtained from single crystal measurements. The calculated values of I/I_C for numerous phases are included in the PDF-4 database and were utilized in this thesis work.

The Intensity of the *i-th* reflection of a phase a (I_{ia}) is expressed as:

$$I_{ia} = \frac{K_{ia}X}{\mu\rho_a} \tag{6}$$

where X is the mass fraction of phase a to be determined, and K_{ia} is a constant that incorporates the scaling factor, the structure factor, the Lorentz polarization factor, and the temperature factor for the *i-th* reflection of phase a.

Substituting (6) into (5) and developing the calculations yields:

$$I_a/I_C = \frac{K_aX_a\rho_C}{K_CX_C\rho_a} \tag{7}$$

By collecting all constant terms in (7) into a single constant K, the result is:

$$I_a/I_C = K\frac{X_a}{X_C} \tag{8}$$

For a mixture of phases *a* and *b*, the following expression is derived:

$$\frac{I_a}{I_b} = \left(\frac{I_a/I_C}{I_b/I_C}\right)\frac{X_a}{X_b} \tag{9}$$

The values of I_a and I_b are obtained from the experimental XRD pattern, and the values of I_a/I_C and I_b/I_C are contained in the PDF-4 database, thus allowing the mass fractions of phases *a* and *b* to be derived from equation (9) in a semi-quantitative manner[133].

3.5 Experimental results and discussion

3.5.1 Preliminary experiments

The initial observation regarding the possibility of obtaining nanocrystalline iron through the decomposition of iron pentacarbonyl occurred in our laboratory during the synthesis of iron nanoparticles in solution. The synthesis protocol involved heating a mixture of 1-octadecene, oleylamine, and iron pentacarbonyl at 165°C under an argon atmosphere. Applying a 225°C flexible heating mantle to the upper part of the flask formed a metallic film on the hot reactor surfaces. The recovered material was characterized as elemental iron with a grain size of 13 nm.

Given iron's exceptionally high surface energy (2.25 J/m² [134]), such limited grain growth was unusual without surface stabilization. The initial hypothesis for the formation of this material is that intense heating causes oleylamine to evaporate from the reaction mixture. The oleylamine vapors then coordinate the iron surface, halting grain growth by encapsulating the grains in a ligand sphere. This ligand sphere also allows grains to slide over one another until they reach an equilibrium position, creating a relatively dense and uniform structure.

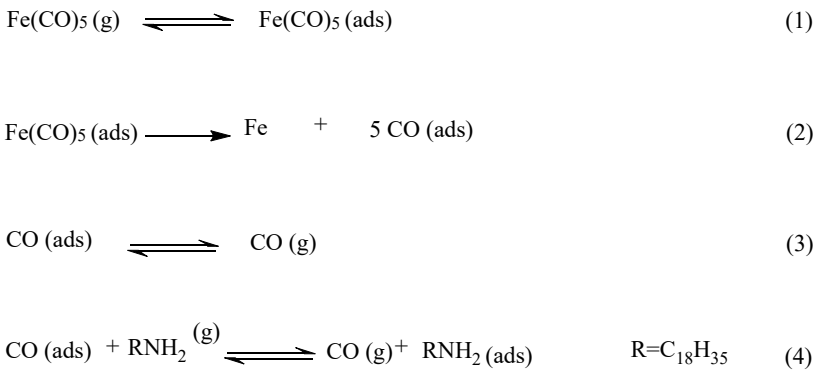

Scheme 3.5.1 *Proposed deposition process reactions.*

The proposed reactions are reported in Scheme 3.5.1. In the first reaction step, vaporized iron pentacarbonyl adsorbs onto a hot surface (initially glass, later on the formed iron surface). Following adsorption, iron pentacarbonyl decomposes with the release of five CO molecules (2). Reaction (2) is the sum of five consecutive steps, each involving a single CO molecule dissociating from the precursor, but for our purposes, only the overall reaction is relevant. At the temperatures used in this process the precursor decomposition is much faster than the reverse recombination with CO, intermediates are short-lived, making their concentration effectively zero and the deposition reaction is under kinetic control[135].

The adsorbed CO must desorb for further iron deposition to proceed (3). This is the critical process step, as CO adsorbed on iron can undergo various parasitic reactions, including (5) and (6), reported in Scheme 3.5.2. Reaction (5) involves CO decomposition into its elements, leading to the formation of iron oxides and carbides in the deposited material, while reaction (6) produces elemental carbon, which remains in the deposit as amorphous or graphitic residue.

Oleylamine plays a critical role by competing with CO for surface sites (4), coordinating the iron nanocrystals with a ligand sphere. Amines exhibit high affinity for iron, and the adsorption energy of an amine on an iron surface is comparable to CO's adsorption energy (ranging from 42–71 kJ/mol for ammonia[134] and 35–48 kJ/mol for CO[136] according to DFT calculations). Thus, oleylamine's surface coordination would inhibit parasitic reactions, passivating the iron surface.

Secondary and parasitic reactions considered include the one reported in Scheme 3.5.2.

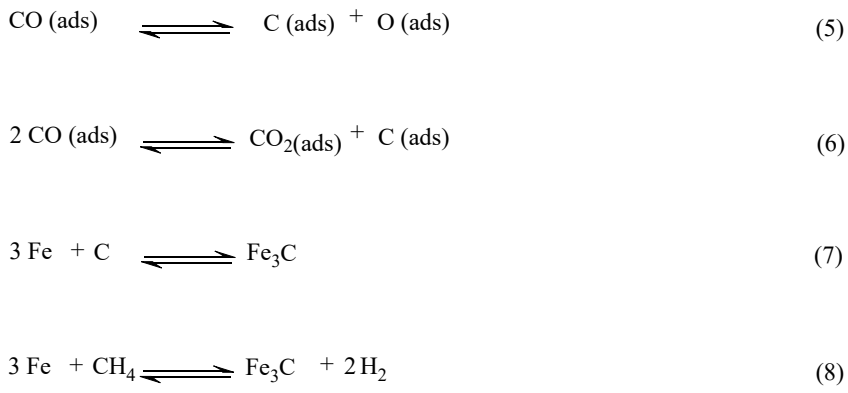

Scheme 3.5.2 *Parasitic reactions in the deposition process.*

Reactions involving CO (5)[137] and hydrocarbon (8)[138] adsorption on iron surfaces has been studied extensively in the Fischer-Tropsch process for producing hydrocarbons from CO and H_2 mixtures, and these findings are directly applicable here. Reaction (6), known as the Boudouard equilibrium, is catalyzed by metals like iron and nickel, as well as their oxides and carbides. This reaction is highly significant in industry, causing Fischer-Tropsch catalyst deactivation via carbonaceous deposits, corrosion in CO_2-cooled graphite-core nuclear reactors, and disintegration of iron refractories in furnaces due to carbon accumulation in pores, but it is also exploited for carbon black production[139].

The Boudouard equilibrium shifts to the right up to 700 °C; however, even in the presence of a catalyst, an appreciable reaction rate only occurs above 400 °C, with iron showing peak catalytic activity at 550°C[140]. At this temperature, carbon from the reaction can diffuse over the iron surface or within its crystalline structure, forming cementite (Fe_3C) via reaction (7), or Fe_2C at lower temperatures (400°C)[141]. This process would result in not only the erosion of deposited iron but also carbide inclusion in its structure, which degrades mechanical properties by reducing metal plasticity and creating micro-segregations as carbides crystallize as a separate phase from iron[142].

Further carbide-forming reactions include hydrocarbon decomposition catalyzed by the iron surface (8)[143] and pyrolysis of hydrocarbons in an inert

atmosphere. These reactions become increasingly favored at higher temperatures (the activation energy for carbon deposition between 285 and 338°C is only 27 kcal/mol[144]). Consequently, iron deposition from a mixture of iron pentacarbonyl, octadecene, and oleylamine must occur below a threshold temperature to prevent parasitic reactions.

Given the negative impact of carbides on mechanical properties, minimizing carbon content is essential for obtaining functional nanostructured iron, aiming to keep carbon levels below those typical of cast iron (around 3 wt.%).

3.5.2 Controlling the synthesis conditions

The aim of the initial syntheses was to replicate the initial observation in a controlled environment. To this end, it is necessary to have a deposition chamber separated from the reaction environment, achieving greater control over the process temperatures and even simplifying product recovery.

A radiatively heated deposition chamber was designed to fit onto a flask. With this setup, the temperatures of both the reagent mixture in the flask and the deposition chamber can be controlled independently. Within the deposition chamber, a 1 cm × 1 cm glass slide can be placed as the target for deposition. The setup used is described in detail in the experimental section.

The reaction was carried out by maintaining the flask at the initial reaction temperature (165°C) while increasing the deposition chamber temperature to 325°C. Under these conditions, a reflective deposition of nanocrystalline iron with a grain size of 13 nm was obtained. Images of the material and related characterizations are shown in Figure 3.5.1.

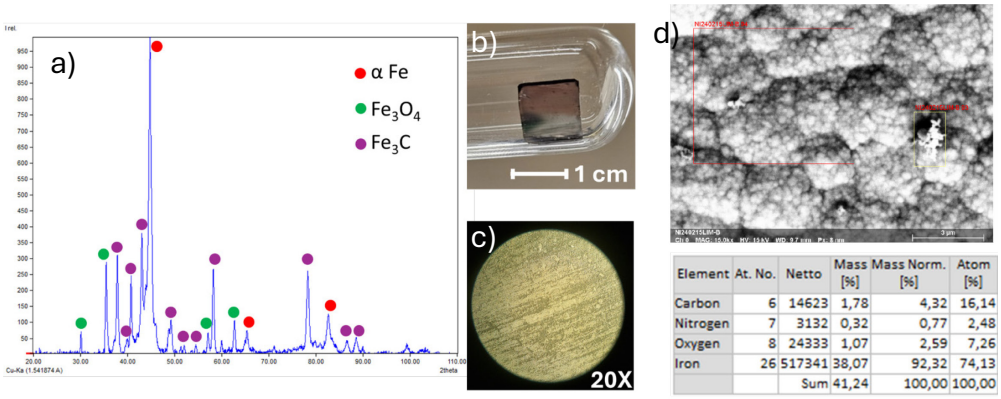

Element	At. No.	Netto	Mass [%]	Mass Norm. [%]	Atom [%]
Carbon	6	14623	1,78	4,32	16,14
Nitrogen	7	3132	0,32	0,77	2,48
Oxygen	8	24333	1,07	2,59	7,26
Iron	26	517341	38,07	92,32	74,13
		Sum	41,24	100,00	100,00

Figure 3.5.1 *a) XRD of the produced material; b), c) the produced material at different magnifications; d) SEM images and EDX analysis.*

The XRD pattern of the obtained material indicates the presence of iron carbide (Fe_3C) as a secondary phase, along with a smaller amount of oxides (primarily magnetite, Fe_3O_4). Under these operating conditions, the oxides are unavoidable due to inert atmosphere contamination during synthesis and exposure of the samples to air. Thus, the presence of a small amount of oxide was not considered an intrinsic limitation of the process.

The carbon content, estimated independently using the RIR method on the XRD pattern and by EDX analysis, is approximately 5% by mass. This is considered a rough estimate; for precise results, variable-angle XPS measurements would be needed to accurately quantify the carbon and study its distribution within the deposited material, which was not available in this thesis work.

Considering the negative impact of carbide on mechanical properties, the next goal was to reduce the carbon content in the deposition. To this end, the deposition chamber temperature was initially evaluated.

The deposition chamber temperature (325°C) was set high enough to ensure rapid and quantitative decomposition of iron pentacarbonyl but not so high as to activate CO disproportionation. This reaction leads to the formation of elemental carbon, potentially the source of iron carbide.

To verify whether this reaction occurred under our conditions, the pH of gases from the reaction environment was tested by bubbling them through an aqueous solution containing an indicator. Passage of gases through the solution did not cause acidification, indicating the absence of CO_2. Thus, it is concluded that either the rate of CO disproportionation is negligible at the given temperature or that the gas residence times in the reaction system are too short to initiate the reaction. Therefore, the formation of elemental carbon due to the Boudouard equilibrium is excluded.

The carbon source for iron carbide formation was traced to the octadecene used as the solvent: within the deposition chamber, an aerosol of octadecene and iron pentacarbonyl is observed. It is hypothesized that incomplete desolvation of the mixture droplets leads to the inclusion of octadecene in the deposition, with pyrolyzed carbon as the main carbon source.

To test this hypothesis, it was considered necessary to reduce the deposition rate by introducing iron pentacarbonyl slowly into the reaction environment using a syringe pump. Slowing the evaporation rate allows greater desolvation of iron pentacarbonyl, avoiding hydrocarbon solvent inclusion in the deposition.

Slowly introducing iron pentacarbonyl during the reaction also ensures a constant precursor evaporation rate and a homogeneous vapor composition throughout the reaction. Initial procedures involved instantaneous injection of iron pentacarbonyl, but this led to a decrease in vapor production over time: iron pentacarbonyl, the lowest-boiling component of the mixture, evaporates quickly after injection.

Using the syringe pump allows for the safe handling of larger amounts of iron pentacarbonyl, enabling the production of bulk material. Given these advantages, the syringe pump was used in all subsequent syntheses.

This modification reduced the carbon content to 3.5% by mass (RIR method) but did not eliminate iron carbide as a secondary phase segregated from the iron.

The second reaction parameter optimized was the temperatures of both the iron reservoir in the flask and the deposition chamber, to increase the amount of material produced and obtain the desired morphology. Under initial conditions, most iron pentacarbonyl decomposed in solution, limiting precursor evaporation and material deposition. The reaction conditions also resulted in two different morphologies: reflective, smooth macroscopic flakes, and black iron powder forming sponge-like aggregates. The two morphologies obtained are shown in Figure 3.5.2.

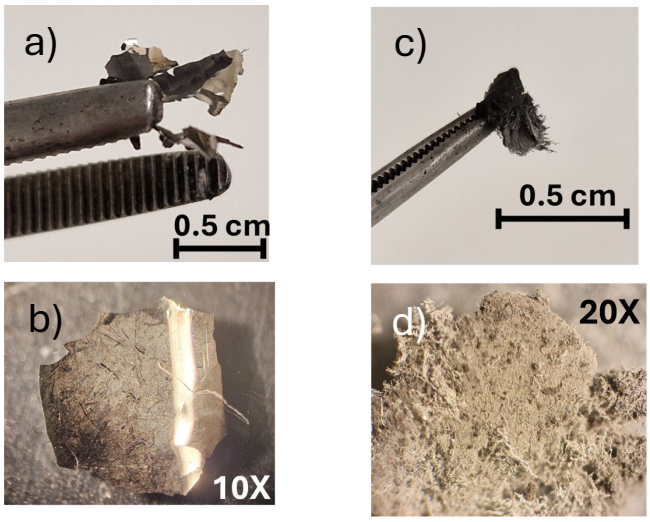

Figure 3.5.2 *Two morphologies of the material at different magnifications: (a), (b) metal flakes, and (c), (d) iron sponge.*

Metal flakes form by heterogeneous-phase decomposition of iron pentacarbonyl on the hot walls of the deposition chamber. The flakes expand during the reaction, coating the entire hot surface with a metal film approximately 10 μm thick, adhering strongly to the glass. Upon cooling, the flakes develop cracks and detach, likely due to the differing thermal conductivities and expansion coefficients of the two materials in contact.

The presence of iron powder suggests homogeneous-phase decomposition of gaseous iron pentacarbonyl rather than heterogeneous decomposition on a hot surface. SEM images of the synthesized material (Figure 3.5.3) show micrometer-sized particles on the iron deposit, indicating their formation in the gas phase and aggregation on the iron surface to form dendritic structures.

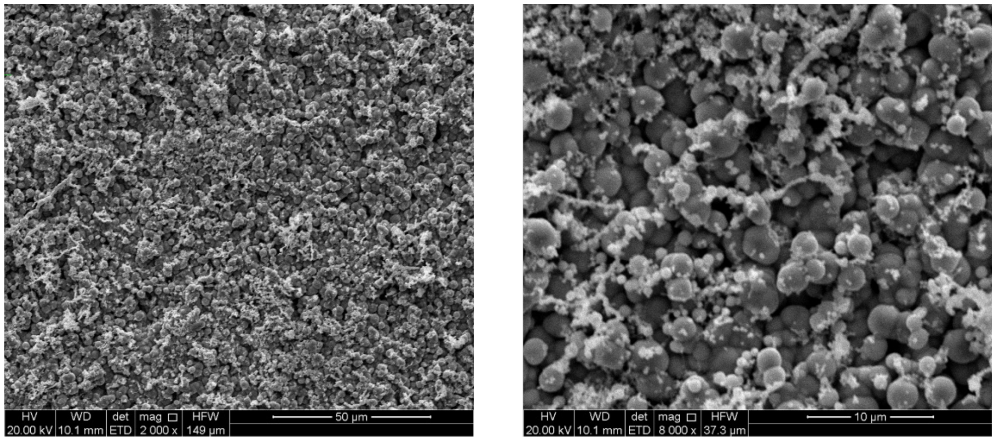

Figure 3.5.3 *SEM images of the deposition at different magnifications.*

The iron powder also exhibits nanometric grain sizes (12–15 nm), indicating that it consists of nanoparticle aggregates. However, it is a less desirable product than the deposited iron flakes because it lacks compactness. Reaction temperatures were optimized to preferentially induce deposition over powder formation. Thus, the chamber temperature is capped to avoid secondary reactions and ensure the precursor decomposes upon reaching the deposition target.

Below 250°C, no reflective deposition occurs, and the carbon content is higher, possibly due to incomplete or slow decomposition of iron pentacarbonyl, while above 350°C, black powder becomes the dominant morphology. To maximize iron deposition, the chamber must be maintained within this temperature range. A temperature near the upper limit is preferred for rapid and complete iron pentacarbonyl decomposition.

XRD analyses of the black powder confirm it consists solely of iron, with no carbides, indicating high-temperature decomposition of iron pentacarbonyl

without carbon residue. Carbides detected in the deposited material are attributed to pyrolyzed solvent, not to incomplete precursor decomposition.

To reduce iron pentacarbonyl decomposition in solution, the reaction mixture temperature in the flask was lowered. Conditions for iron pentacarbonyl decomposition were further investigated due to conflicting literature on its exact decomposition temperature. Deposition trials were conducted with iron pentacarbonyl alone, without solvents or binders.

These trials identified the boiling point of iron pentacarbonyl at 105°C and decomposition onset at 110°C. An interesting finding was the formation of triiron dodecacarbonyl ($Fe_3(CO)_{12}$), a dark green compound, when heating iron pentacarbonyl to its boiling point in an inert atmosphere.

Subsequent iron syntheses were conducted below 100°C in the flask and/or with doubled concentration to promote iron pentacarbonyl evaporation while minimizing solvent evaporation. Although these syntheses reduced carbon content to 2% by mass, they yielded very thin or no deposits, indicating that at these temperatures, the evaporation rate is too low to produce a bulk material despite prolonged reaction times of up to 6 hours.

3.5.3 CVD-like synthesis of nanostructured iron

Since it was not possible to significantly increase the evaporation rate by raising the temperature without causing the decomposition of iron pentacarbonyl, the decision was made to promote evaporation by pumping an inert gas through a reservoir of the reagent at room temperature. The iron pentacarbonyl is then transported by the gas into a separate heated chamber for decomposition. To this end, a new reaction setup was designed with an evaporation chamber and a heated tubular reactor for precursor decomposition, detailed in the experimental section.

The first synthesis was conducted solely with iron pentacarbonyl, heating the deposition chamber to 350°C, and unexpectedly resulted in the deposition of nanocrystalline iron with 13 nm grains without any ligand present. This observation allowed for a significant simplification of the reaction system and conclusively disproved the initial hypothesis regarding the role of ligands. Such limited grain growth is surprising when considering conventional nucleation and growth, which is typically governed by a decrease in free energy.

The hypothesis regarding the formation of such small grains without any surface stabilization is that the thermal shock associated with the contact between the precursor and the surface generates a supersaturation burst, leading to the formation of a vast number of nanoscale nuclei, and the deposition occurs so rapidly that growth is inhibited.

By eliminating solvents and ligands, and having verified that iron pentacarbonyl decomposes cleanly without leaving carbon residues, the iron deposited using this technique was carbide-free in XRD (Figure 3.5.4). EDX analyses indicate a carbon content of 5% by mass, consistent with organic substances adsorbed on surfaces exposed to the atmosphere. The most significant finding is the absence of a secondary iron carbide phase.

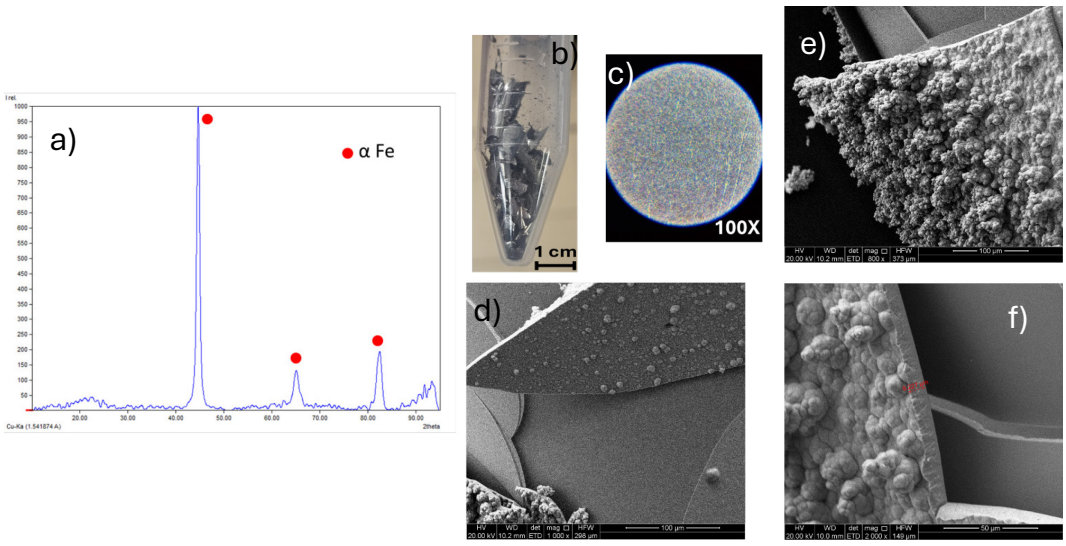

Figure 3.5.4 *a) XRD pattern of the produced material; b), c) the produced material at different magnifications; d), e) SEM images of the material's surface; f) SEM image of the material cross-section.*

SEM images reveal two different growth regimes: initially, a uniform layer about 10 μm thick forms, followed by irregular deposition. The initial uniform layer suggests growth limited by reaction kinetics, while the irregular deposition implies growth limited by diffusion, amplifying surface irregularities.

A transition between growth regimes is hypothesized, attributed to the formation of a carbon monoxide-saturated boundary layer above the iron deposit. The boundary layer uniformly covers the deposition, so any irregularity that rises above the film profile acts as a point of higher reactivity and is amplified by the reaction. Additional material deposits in the higher regions of the iron film, enhancing irregularities. To achieve uniform growth throughout the reaction, it is necessary to eliminate the boundary layer, so pulsed deposition is preferred over continuous deposition.

Since it is not possible to create vacuum cycles in this system, small aliquots of iron pentacarbonyl are introduced, waiting for the boundary layer to dissipate through diffusion between each aliquot.

To reduce grain size below 10 nm, a synthesis was conducted at 600°C. This synthesis produced a very thin deposit and a large quantity of powder. The grain size of the deposit was found to be 22 nm, suggesting that the high temperature caused grain growth.

This phenomenon demonstrates that grain size can be controlled by varying the deposition chamber temperature, reagent mass flow, and residence time in the reaction chamber, allowing for samples with variable grain sizes that can undergo mechanical testing to study a Hall-Petch limit behavior.

The graph in Figure 3.5.5 represents the melting point variation of different iron compounds observed during this thesis work as a function of the curvature radius of a spherical nanoparticle. The melting point of a 13 nm iron nanoparticle is 1158°C, compared to 1538°C for coarse-grained iron. This indicates that at the working temperatures considered (between 200 and 400°C), it is possible to stabilize even smaller grains, below 10 nm, suggesting that the studied process has not reached its thermodynamic limit for grain size.

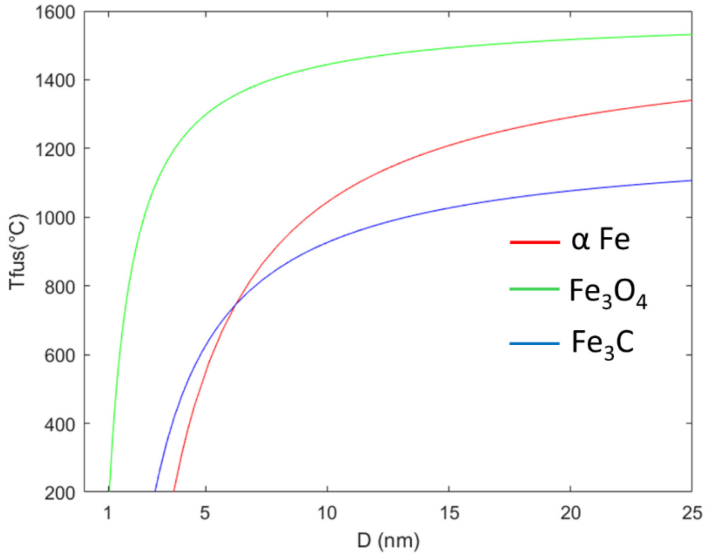

Figure 3.5.5 *Variation in the melting point of different iron compounds as a function of curvature.*

3.6 Conclusions on nanostructured iron project

The aim of this project was to synthesize a bulk sample of nanocrystalline iron with grain sizes close to 10 nm and to study its mechanical properties. The synthesis was carried out through a home-made setup for chemical vapor deposition (CVD) of iron pentacarbonyl, chosen for its clean and quantitative decomposition into high-purity elemental iron.

It has been possible to successfully synthesized nanostructured iron with grain sizes down to around 13 nm. This was achieved by optimizing reaction parameters, including deposition chamber temperature, precursor deposition rate, and inert gas flow. Notably, nanostructured iron films with a thickness up to 10 μm were produced, an unprecedented result in the literature for CVD-produced nanostructured iron films. The purity of deposition was enhanced to obtain a single α-iron phase by eliminating solvents and binders from the deposition process and controlling parasitic reactions that could lead to carbide formation. Reaction conditions were optimized to achieve the desired morphology, the compact metallic

flakes, and reduce the production of iron powder. This was accomplished by finely adjusting reaction temperatures and precursor introduction rates.

The study demonstrated that the deposition process has not yet reached its thermodynamic limits, suggesting the potential for materials with even smaller grain structures, opening pathways for further mechanical property enhancements. Additional studies are required to overcome the boundary layer issue, a carbon monoxide-saturated layer formed above the iron deposition, hindering uniform material growth. A possible solution may involve implementing a pulsed deposition method, allowing the boundary layer to dissipate between precursor aliquots. The ultimate goal is to obtain a macroscopically thick and dense material which can undergo standard mechanical characterizations to determine its hardness. Mechanical characterization of the produced material is essential to evaluate the impact of grain size on the properties of nanostructured iron. Specifically, studying the behavior of mechanical properties near the Hall-Petch limit could provide valuable insights into the behavior of nanostructured metals.

4 Conclusions

The present section summarizes my research activities conducted during my Ph.D. in Materials Science and Technology at the University of Parma, where I focused on the study of fundamental mechanisms and innovative low-energy strategies for crystallization processes and metal production. My work primarily examined metal-induced crystallization (MIC) of silicon dioxide (SiO_2), aiming to lower energy requirements for phase transformation from amorphous to crystalline states. I explored how metal cations affect SiO_2 crystallization, employing alkali and alkaline-earth metal salts to drive crystallization at temperatures below those of conventional methods via calcination treatments as potential industrially scalable processes. I deeply investigated the products obtained via Powder X-ray diffraction as the primary structural characterization method, combined with additional analytical techniques, which allowed me to formulate hypotheses on the fundamental mechanisms driving MIC.

The experimental results indicate that alkali cations play an active role in the crystallization of amorphous SiO_2, promoting the formation of cristobalite and tridymite at lower temperatures than those typically required to overcome high activation energies. The dependence of the c-lattice parameter increment on cation size, the shift to lower frequencies of the symmetric Si-O-Si stretching band, and the homogeneous distribution of these elements within the silica matrix provide evidence for the incorporation of alkali metal cations within the silica structure. This phenomenon likely underlies the crystallization of amorphous SiO_2 at temperatures otherwise impossible without the addition of these metal elements. In contrast, the experiments conducted on alkaline earth cations suggest a possible two-phase crystallization mechanism, in which firstly the metals react with SiO_2 to form intermediate silicates during calcination and subsequently these silicates

promote quartz nucleation and growth. Unlike the phenomenon observed in alkali metals, alkaline earth cations are not incorporated into the final quartz structure and can be removed by acid washing. In this latter case a detailed understanding of the crystallization mechanism induced by alkaline earth cations opens new pathways for the controlled synthesis of high-purity quartz, selectively obtained in the proposed calcination treatments to reduce the energy footprint of SiO_2 production across various industries. Similarly, it should be possible to determine optimal conditions for selectively obtaining also cristobalite and tridymite phases by metal induced crystallization, proposing alternative and low energy consuming processes also for the applicative point of view. It can thus be stated that this study has successfully advanced comprehension of the crystallization mechanism of amorphous silica induced by metal use. However, further investigations are required to fully elucidate this process, specifically in understanding the chemical processes enabling metals to catalyze crystallization, using local techniques.

In a secondary project, I focused on the bulk synthesis of nanocrystalline iron via chemical vapor deposition (CVD) carried out in a home-made setup, achieving nanometer-scale grain sizes and controlled morphologies in iron films. This study underscored the potential for producing dense, nanostructured materials with enhanced mechanical properties. These findings open further opportunities to optimize synthesis conditions for achieving the desired combination of small-scale features and bulk material applications, particularly in industrial sectors requiring high durability with reduced energy input.

In conclusion, this Ph.D. thesis provides a step forward in our understanding of metal-induced crystallization of SiO_2 and synthesis of nanostructured metals, highlighting methods to reduce energy consumption and improve material performance that are critical for sustainable industrial development. The findings not only aim to contribute to the fundamental science behind these processes, but also pave the way for applied research to optimize production techniques, supporting a sustainable future for energy-intensive industries.

Bibliography

1. Scheel, H. J. *Crystal Growth Technology: Semiconductors and Dielectrics*. (Wiley-VCH, Weinheim, 2011).

2. Zhu, Y., Lu, C. & Shum, P. Photonic crystal fibers and their applications in optical communications and sensors. in (eds. Jian, S., Shen, S. & Okamoto, K.) 37 (Shanghai, China, 2002). doi:10.1117/12.481255.

3. Huber, G., Kränkel, C. & Petermann, K. Solid-state lasers: status and future [Invited]. *J. Opt. Soc. Am. B* **27**, B93 (2010).

4. Krauss, T. Photonic crystals in the optical regime — past, present and future. *Prog. Quantum Electron.* **23**, 51–96 (1999).

5. Yang, Y. M. *et al.* Development of high-performance multicrystalline silicon for photovoltaic industry. *Prog. Photovolt. Res. Appl.* **23**, 340–351 (2015).

6. Frenzel, S. Kristallisationsschemata in der Zuckerindustrie. *Chem. Ing. Tech.* **92**, 769–776 (2020).

7. Quilaqueo, M., Duizer, L. & Aguilera, J. M. The morphology of salt crystals affects the perception of saltiness. *Food Res. Int.* **76**, 675–681 (2015).

8. Rohani, S. Applications of the crystallization process in the pharmaceutical industry. *Front. Chem. Eng. China* **4**, 2–9 (2010).

9. Cressler, J. D. Silicon Earth: A Historical Perspective on the Invention/Discovery of the Transistor. *IEEE Electron Devices Mag.* **1**, 16–24 (2023).

10. Haller, E. E. Germanium: From its discovery to SiGe devices. *Mater. Sci. Semicond. Process.* **9**, 408–422 (2006).

11. Fornari, R. Bulk Crystal Growth of Semiconductors: An Overview. in *Comprehensive Semiconductor Science and Technology* 1–35 (Elsevier, 2011). doi:10.1016/B978-0-44-453153-7.00088-2.

12. Sangwal, K. *Additives and Crystallization Processes: From Fundamentals to Applications*. (Wiley, 2007). doi:10.1002/9780470517833.

13. De Sio, A. *et al.* Physical vapor deposition synthesis of amorphous silicate layers and nanostructures as cosmic dust analogs. *Astron. Astrophys.* **589**, A4 (2016).

14. Yang, J. *et al.* Amorphous-Phase-Mediated Crystallization of Ni Nanocrystals Revealed by High-Resolution Liquid-Phase Electron Microscopy. *J. Am. Chem. Soc.* **141**, 763–768 (2019).

15. Feng, T., Pinal, R. & Carvajal, M. T. Process Induced Disorder in Crystalline Materials:Differentiating Defective Crystals from the Amorphous Form of Griseofulvin. *J. Pharm. Sci.* **97**, 3207–3221 (2008).

16. Edurev. Potential Energy curve.

17. Nadarajan, R., Wan Abu Bakar, W. A. & Ali, R. Effect of Calcination Temperature on Metal Oxides and their Photocatalytic Activity. *Adv. Mater. Res.* **1107**, 73–78 (2015).

18. Guo, F., Peng, Z.-G., Dai, J.-Y. & Xiu, Z.-L. Calcined sodium silicate as solid base catalyst for biodiesel production. *Fuel Process. Technol.* **91**, 322–328 (2010).

19. Kim, S., Lee, G. S., Shrout, T. R. & Venkataramani, S. Fabrication of fine-grain piezoelectric ceramics using reactive calcination. *J. Mater. Sci.* **26**, 4411–4415 (1991).

20. Wang, M., Wang, J., Zhang, Y., Yu, Y. & Shan, W. High-temperature calcination enhances the activity of MnO_x catalysts for soot oxidation. *Catal. Sci. Technol.* 10.1039.D4CY00983E (2024) doi:10.1039/D4CY00983E.

21. Shen, H. L. *et al.* Effect of calcination temperature on the microstructure, crystallinity and photocatalytic activity of TiO2 hollow spheres. *J. Alloys Compd.* **542**, 32–36 (2012).

22. Aneziris, C. G., Homola, F. & Borzov, D. Materials and Process Development of Advanced Refractories for Innovative Metal Processing. *Adv. Eng. Mater.* **6**, 562–568 (2004).

23. Wolfenden, R. & Snider, M. J. The Depth of Chemical Time and the Power of Enzymes as Catalysts. *Acc. Chem. Res.* **34**, 938–945 (2001).

24. Yadav, G. D. & Nair, J. J. Sulfated zirconia and its modified versions as promising catalysts for industrial processes. *Microporous Mesoporous Mater.* **33**, 1–48 (1999).

25. Konno, T. J. & Sinclair, R. Metal-contact-induced crystallization of semiconductors. *Mater. Sci. Eng. A* **179–180**, 426–432 (1994).

26. Kryshtal, A., Bogatyrenko, S. & Ferreira, P. Metal-induced crystallization of amorphous semiconductor films: Nucleation phenomena in Ag-Ge films. *Appl. Surf. Sci.* **606**, 154873 (2022).

27. Yang, C., Hirose, Y., Nakao, S., Hoang, N. L. H. & Hasegawa, T. Metal-induced solid-phase crystallization of amorphous TiO_2 thin films. *Appl. Phys. Lett.* **101**, 052101 (2012).

28. Trentler, T. J., Denler, T. E., Bertone, J. F., Agrawal, A. & Colvin, V. L. Synthesis of TiO_2 Nanocrystals by Nonhydrolytic Solution-Based Reactions. *J. Am. Chem. Soc.* **121**, 1613–1614 (1999).

29. Venezia, A. M., La Parola, V., Longo, A. & Martorana, A. Effect of Alkali Ions on the Amorphous to Crystalline Phase Transition of Silica. *J. Solid State Chem.* **161**, 373–378 (2001).

30. Hanaor, D. A. H. & Sorrell, C. C. Review of the anatase to rutile phase transformation. *J. Mater. Sci.* **46**, 855–874 (2011).

31. Danty, P. M. P. *et al.* Microwave-Assisted and Metal-Induced Crystallization: A Rapid and Low Temperature Combination. *Inorg. Chem.* **59**, 6232–6241 (2020).

32. Garníca-Romo, M. G. *et al.* Structure of heat-treated sol-gel SiO_2 glasses containing silver. *J. Mater. Res.* **16**, 2007–2012 (2001).

33. Carretero-Genevrier, A., Drisko, G. L., Grosso, D., Boissiere, C. & Sanchez, C. Mesoscopically structured nanocrystalline metal oxide thin films. *Nanoscale* **6**, 14025–14043 (2014).

34. Yang, C., Hirose, Y., Nakao, S., Hoang, N. L. H. & Hasegawa, T. Metal-induced solid-phase crystallization of amorphous TiO 2 thin films. *Appl. Phys. Lett.* **101**, 052101 (2012).

35. Sangani, L. D. V., Sri, K. V., Mohiddon, Md. A. & Krishna, M. G. Low temperature Au induced crystallization of titanium dioxide thin films for resistive switching applications. *RSC Adv.* **5**, 67493–67499 (2015).

36. *Metal-Induced Crystallization: Fundamentals and Applications*. (Jenny Stanford Publishing, 2015). doi:10.1201/b18032.

37. Drisko, G. L. *et al.* Water-Induced Phase Separation Forming Macrostructured Epitaxial Quartz Films on Silicon. *Adv. Funct. Mater.* **24**, 5494–5502 (2014).

38. Lin, C.-C., Chen, S.-F., Liu, L. & Li, C.-C. Size effects of modifying cations on the structure and elastic properties of Na2O–MO–SiO2 glasses (M=Mg, Ca, Sr, Ba). *Mater. Chem. Phys.* **123**, 569–580 (2010).

39. Zhuang, C. & Chen, Y. The effect of nano-SiO2 on concrete properties: a review. *Nanotechnol. Rev.* **8**, 562–572 (2019).

40. Guan, F. *et al.* Transparent Conductive Films Based on Silver Nanowires and SiO 2 Nanoparticles for Flexible Electronics. *ACS Appl. Nano Mater.* **7**, 7845–7855 (2024).

41. Kordoš, P. *et al.* High-power SiO2⁄AlGaN⁄GaN metal-oxide-semiconductor heterostructure field-effect transistors. *Appl. Phys. Lett.* **87**, 143501 (2005).

42. Sasan, K. *et al.* Additive Manufacturing of Optical Quality Germania–Silica Glasses. *ACS Appl. Mater. Interfaces* **12**, 6736–6741 (2020).

43. https://serc.carleton.edu/NAGTWorkshops/mineralogy/mineral_physics/phase_equilibria.html. Silica phase diagram.

44. Zhang, L. & Zhang, G. Ultrahigh Pressure Metamorphism. in *Encyclopedia of Geology* 553–560 (Elsevier, 2021). doi:10.1016/B978-0-08-102908-4.00134-X.

45. Bechmann, R. Elastic and Piezoelectric Constants of Alpha-Quartz. *Phys. Rev.* **110**, 1060–1061 (1958).

46. Iwasaki, F. & Iwasaki, H. Historical review of quartz crystal growth. *J. Cryst. Growth* **237–239**, 820–827 (2002).

47. Walker, A. C. Hydrothermal Synthesis of Quartz Crystals. *J. Am. Ceram. Soc.* **36**, 250–256 (1953).

48. Jiang, X., Jiang, Y.-B. & Brinker, C. J. Hydrothermal synthesis of monodisperse single-crystalline alpha-quartz nanospheres. *Chem. Commun.* **47**, 7524 (2011).

49. Nývlt, J. The Ostwald Rule of Stages. *Cryst. Res. Technol.* **30**, 443–449 (1995).

50. Livage, J. Sol-gel processes. *Curr. Opin. Solid State Mater. Sci.* **2**, 132–138 (1997).

51. Brinker, C. J., Hurd, A. J., Schunk, P. R., Frye, G. C. & Ashley, C. S. Review of sol-gel thin film formation. *J. Non-Cryst. Solids* **147–148**, 424–436 (1992).

52. Dehghanghadikolaei, A. *et al.* Sol-gel process applications: A mini-review. *Proc. Nat. Res. Soc.* **2**, 02008 (2018).

53. Patnaik, P. *Handbook of Inorganic Chemicals*. (McGraw-Hill, New York, 2003).

54. Toby, B. H. & Von Dreele, R. B. *GSAS-II* : the genesis of a modern open-source all purpose crystallography software package. *J. Appl. Crystallogr.* **46**, 544–549 (2013).

55. Shinohara, Y. & Kohyama, N. Quantitative Analysis of Tridymite and Cristobalite Crystallized in Rice Husk Ash by Heating. *Ind. Health* **42**, 277–285 (2004).

56. Zheng, R., Ren, Z., Gao, H., Zhang, A. & Bian, Z. Effects of calcination on silica phase transition in diatomite. *J. Alloys Compd.* **757**, 364–371 (2018).

57. Wang, S., Cui, Z., Xia, X. & Xue, Y. Size-dependent decomposition temperature of nanoparticles: A theoretical and experimental study. *Phys. B Condens. Matter* **454**, 175–178 (2014).

58. Atkins, P. W. & de Paula, J. *Atkins' Physical Chemistry*. (Oxford University Press, Oxford, 2006).

59. Fraissler, G., Jöller, M., Brunner, T. & Obernberger, I. Influence of dry and humid gaseous atmosphere on the thermal decomposition of calcium chloride and its impact on the remove of heavy metals by chlorination. *Chem. Eng. Process. Process Intensif.* **48**, 380–388 (2009).

60. Sulka, G. D. Electrochemistry of Thin Films and Nanostructured Materials. *Molecules* **28**, 4040 (2023).

61. Szczech, J. R., Higgins, J. M. & Jin, S. Enhancement of the thermoelectric properties in nanoscale and nanostructured materials. *J Mater Chem* **21**, 4037–4055 (2011).

62. Leslie-Pelecky, D. L. & Rieke, R. D. Magnetic Properties of Nanostructured Materials. *Chem. Mater.* **8**, 1770–1783 (1996).

63. Gavrilenko, V. I. *Optics of Nanomaterials*. (Jenny Stanford Publishing, 2016). doi:10.1201/9781315272894.

64. *The Chemistry of Nanomaterials: Synthesis, Properties and Applications*. (Wiley-VCH, Weinheim, 2006).

65. Kareem, S. & Mawllod, S. Size dependent thermodynamic properties of nanoparticles. *Int. J. Thermodyn.* **23**, 245–250 (2020).

66. Wu, Q., Miao, W., Zhang, Y., Gao, H. & Hui, D. Mechanical properties of nanomaterials: A review. *Nanotechnol. Rev.* **9**, 259–273 (2020).

67. Poh, T. Y. *et al.* Inhaled nanomaterials and the respiratory microbiome: clinical, immunological and toxicological perspectives. *Part. Fibre Toxicol.* **15**, 46 (2018).

68. Koch, C. C. Structural nanocrystalline materials: an overview. *J. Mater. Sci.* **42**, 1403–1414 (2007).

69. Froes, F. H. (Sam), Senkov, O. N. & Baburaj, E. G. Synthesis of nanocrystalline materials — an overview. *Mater. Sci. Eng. A* **301**, 44–53 (2001).

70. Lopeandía, A. F. & Rodríguez-Viejo, J. Size-dependent melting and supercooling of Ge nanoparticles embedded in a SiO2 thin film. *Thermochim. Acta* **461**, 82–87 (2007).

71. Sun, J. & Simon, S. L. The melting behavior of aluminum nanoparticles. *Thermochim. Acta* **463**, 32–40 (2007).

72. Bano, A. *et al.* Enhancing catalytic activity of gold nanoparticles in a standard redox reaction by investigating the impact of AuNPs size, temperature and reductant concentrations. *Sci. Rep.* **13**, 12359 (2023).

73. Kim, B. H., Heo, J. & Park, J. Determination of the 3D Atomic Structures of Nanoparticles. *Small Sci.* **1**, 2000045 (2021).

74. Reghunadhan, A., Kalarikkal, N. & Thomas, S. Mechanical Property Analysis of Nanomaterials. in *Characterization of Nanomaterials* 191–212 (Elsevier, 2018). doi:10.1016/B978-0-08-101973-3.00007-9.

75. Zhang, B. *Physical Fundamentals of Nanomaterials*. (Chemical industry press William Andrew Elsevier, Oxford, 2018).

76. Ramalingam, G. *et al.* Quantum Confinement Effect of 2D Nanomaterials. in *Quantum Dots - Fundamental and Applications* (ed. Divsar, F.) (IntechOpen, 2020). doi:10.5772/intechopen.90140.

77. de Broglie, L. V. *On the Theory of Quanta*. (1925).

78. Khanna, V. K. Nanomaterials and Their Properties. in *Integrated Nanoelectronics* 25–41 (Springer India, New Delhi, 2016). doi:10.1007/978-81-322-3625-2_3.

79. Bharmoria, P. & Ventura, S. P. M. Optical Applications of Nanomaterials. in *Nanomaterials for Healthcare, Energy and Environment* (eds. Bhat, A. H. et al.) vol. 118 1–29 (Springer Singapore, Singapore, 2019).

80. Li, Z. & Yin, Y. Stimuli-Responsive Optical Nanomaterials. *Adv. Mater.* **31**, 1807061 (2019).

81. Kim, H. *et al.* Multifunctional Photonic Nanomaterials for Diagnostic, Therapeutic, and Theranostic Applications. *Adv. Mater.* **30**, 1701460 (2018).

82. Chao, J. *et al.* Optical properties and applications of metal nanomaterials in ultrafast photonics: a review. *J. Mater. Sci.* **59**, 13433–13461 (2024).

83. Ray, P. C. Size and shape dependent second order nonlinear optical properties of nanomaterials and their application in biological and chemical sensing. *Chem. Rev.* **110**, 5332–5365 (2010).

84. Wen, N. *et al.* Emerging flexible sensors based on nanomaterials: recent status and applications. *J. Mater. Chem. A* **8**, 25499–25527 (2020).

85. Mitchell, M. J. *et al.* Engineering precision nanoparticles for drug delivery. *Nat. Rev. Drug Discov.* **20**, 101–124 (2021).

86. Dutta, B., Barick, K. C. & Hassan, P. A. Recent advances in active targeting of nanomaterials for anticancer drug delivery. *Adv. Colloid Interface Sci.* **296**, 102509 (2021).

87. Li, H., Jian, S. & Baalousha, M. Applications of Catalytic Nanomaterials in Energy and Environment. *Molecules* **28**, 4000 (2023).

88. Khalil, M., Kadja, G. T. M. & Ilmi, Moh. M. Advanced nanomaterials for catalysis: Current progress in fine chemical synthesis, hydrocarbon processing, and renewable energy. *J. Ind. Eng. Chem.* **93**, 78–100 (2021).

89. Mokhtar, M. O. A. The effect of hardness on the frictional behaviour of metals. *Wear* **78**, 297–304 (1982).

90. Lowe, T. C., Valiev, R. Z., Li, X. & Ewing, B. R. Commercialization of bulk nanostructured metals and alloys. *MRS Bull.* **46**, 265–272 (2021).

91. Hansen, N. Hall–Petch relation and boundary strengthening. *Scr. Mater.* **51**, 801–806 (2004).

92. Tian, L. & Li, L. A Review on the Strengthening of Nanostructured Materials. *Int. J. Curr. Eng. Technol.* **8**, (2018).

93. Dangwal, S., Edalati, K., Valiev, R. Z. & Langdon, T. G. Breaks in the Hall–Petch Relationship after Severe Plastic Deformation of Magnesium, Aluminum, Copper, and Iron. *Crystals* **13**, 413 (2023).

94. Takeda, K., Nakada, N., Tsuchiyama, T. & Takaki, S. Effect of Interstitial Elements on Hall–Petch Coefficient of Ferritic Iron. *ISIJ Int.* **48**, 1122–1125 (2008).

95. Meyers, M. A., Mishra, A. & Benson, D. J. Mechanical properties of nanocrystalline materials. *Prog. Mater. Sci.* **51**, 427–556 (2006).

96. Naik, S. N. & Walley, S. M. The Hall–Petch and inverse Hall–Petch relations and the hardness of nanocrystalline metals. *J. Mater. Sci.* **55**, 2661–2681 (2020).

97. Ondry, J. C. & Alivisatos, A. P. Application of Dislocation Theory to Minimize Defects in Artificial Solids Built with Nanocrystal Building Blocks. *Acc. Chem. Res.* **54**, 1419–1429 (2021).

98. Zhang, H. W., Huang, X., Pippan, R. & Hansen, N. Thermal behavior of Ni (99.967% and 99.5% purity) deformed to an ultra-high strain by high pressure torsion. *Acta Mater.* **58**, 1698–1707 (2010).

99. Andrievski, R. A. Stability of nanostructured materials. *J. Mater. Sci.* **38**, 1367–1375 (2003).

100. Peng, H. R., Liu, B. S. & Liu, F. A strategy for designing stable nanocrystalline alloys by thermo-kinetic synergy. *J. Mater. Sci. Technol.* **43**, 21–31 (2020).

101. Koch, C. C., Scattergood, R. O., Darling, K. A. & Semones, J. E. Stabilization of nanocrystalline grain sizes by solute additions. *J. Mater. Sci.* **43**, 7264–7272 (2008).

102. Liu, X. C., Zhang, H. W. & Lu, K. Strain-Induced Ultrahard and Ultrastable Nanolaminated Structure in Nickel. *Science* **342**, 337–340 (2013).

103. Liang, N. & Zhao, Y. A review on thermal stability of nanostructured materials. *J. Alloys Compd.* **938**, 168528 (2023).

104. Abid, N. *et al.* Synthesis of nanomaterials using various top-down and bottom-up approaches, influencing factors, advantages, and disadvantages: A review. *Adv. Colloid Interface Sci.* **300**, 102597 (2022).

105. Tschopp, M. A., Murdoch, H. A., Kecskes, L. J. & Darling, K. A. "Bulk" Nanocrystalline Metals: Review of the Current State of the Art and Future Opportunities for Copper and Copper Alloys. *JOM* **66**, 1000–1019 (2014).

106. Carsley, J. E., Fisher, A., Milligan, W. W. & Aifantis, E. C. Mechanical behavior of a bulk nanostructured iron alloy. *Metall. Mater. Trans. A* **29**, 2261–2271 (1998).

107. Darling, K. A. *et al.* Microstructure and mechanical properties of bulk nanostructured Cu–Ta alloys consolidated by equal channel angular extrusion. *Acta Mater.* **76**, 168–185 (2014).

108. Han, J.-K., Herndon, T., Jang, J., Langdon, T. G. & Kawasaki, M. Synthesis of Hybrid Nanocrystalline Alloys by Mechanical Bonding through High-Pressure Torsion. *Adv. Eng. Mater.* **22**, 1901289 (2020).

109. Baker, M. A. *et al.* The nanostructure and mechanical properties of PVD CrCu (N) coatings. *Surf. Coat. Technol.* **162**, 222–227 (2003).

110. Boyd, E. P., Ketchum, D. R., Deng, H. & Shore, S. G. Chemical Vapor Deposition of Metallic Thin Films Using Homonuclear and Heteronuclear Metal Carbonyls. *Chem. Mater.* **9**, 1154–1158 (1997).

111. Vicenzo, A. Structure and Mechanical Properties of Electrodeposited Nanocrystalline Ni-Fe Alloys. *J. Electrochem. Soc.* **160**, D570–D577 (2013).

112. Mukai, T. *et al.* Nanostructured Al–Fe alloys produced by e-beam deposition: static and dynamic tensile properties. *Acta Mater.* **51**, 4197–4208 (2003).

113. Shen, Y. F., Xue, W. Y., Wang, Y. D., Liu, Z. Y. & Zuo, L. Mechanical properties of nanocrystalline nickel films deposited by pulse plating. *Surf. Coat. Technol.* **202**, 5140–5145 (2008).

114. Groza, J. R. Nanosintering. *Nanostructured Mater.* **12**, 987–992 (1999).

115. Liu, Y. *et al.* Crystallographically Textured Nanomaterials Produced from the Liquid Phase Sintering of $Bi_x Sb_{2-x} Te_3$ Nanocrystal Building Blocks. *Nano Lett.* **18**, 2557–2563 (2018).

116. Wang, Y. & Shi, J. Effect of hot isostatic pressing on nanoparticles reinforced AlSi10Mg produced by selective laser melting. *Mater. Sci. Eng. A* **788**, 139570 (2020).

117. Ji, S., Gu, Q. & Xia, B. Porosity dependence of mechanical properties of solid materials. *J. Mater. Sci.* **41**, 1757–1768 (2006).

118. Zhou, Q., Li, J., Wang, M. & Zhao, D. Iron-based magnetic nanomaterials and their environmental applications. *Crit. Rev. Environ. Sci. Technol.* **46**, 783–826 (2016).

119. Pour, A. N., Housaindokht, M. R., Tayyari, S. F. & Zarkesh, J. Fischer-Tropsch synthesis by nano-structured iron catalyst. *J. Nat. Gas Chem.* **19**, 284–292 (2010).

120. Adampourezare, M., Hasanzadeh, M., Hoseinpourefeizi, M.-A. & Seidi, F. Iron/iron oxide-based magneto-electrochemical sensors/biosensors for ensuring food safety: recent progress and challenges in environmental protection. *RSC Adv.* **13**, 12760–12780 (2023).

121. Kotenev, V. A., Petrunin, M. A., Maksaeva, L. B., Timofeeva, V. A. & Tsivadze, A. Yu. Vacuum oxidation of freshly deposited iron nanofilms. *Prot. Met. Phys. Chem. Surf.* **49**, 479–484 (2013).

122. Krogstad, J. A., Keimel, C. & Hemker, K. J. Emerging materials for microelectromechanical systems at elevated temperatures. *J. Mater. Res.* **29**, 1597–1608 (2014).

123. Ekinci, K. L. & Roukes, M. L. Nanoelectromechanical systems. *Rev. Sci. Instrum.* **76**, 061101 (2005).

124. Lau, K.-T., Loganathan, Z. L. & Abd-Shukor, R. Arc Vapour Deposition of Iron Film during Magnetron Sputtering of Ti Film: Effect of Substrate's Materials and Surface Roughness. *Int. J. Electrochem. Sci.* **10**, 5488–5497 (2015).

125. Choi, C. J., Tolochko, O. & Kim, B. K. Preparation of iron nanoparticles by chemical vapor condensation. *Mater. Lett.* **56**, 289–294 (2002).

126. Krisyuk, V. *et al.* Chemical Vapor Deposition of Iron, Iron Carbides, and Iron Nitride Films from Amidinate Precursors. *J. Electrochem. Soc.* **157**, D454 (2010).

127. Jartych, E., Żurawicz, J. K., Mączka, E. & Borc, J. Preparation of thin iron films by electrodeposition and characterization of their local magnetic properties. *Mater. Chem. Phys.* **72**, 356–359 (2001).

128. Tahir, N. A. M., Abdollah, M. F. B., Tamaldin, N., Zin, M. R. B. M. & Amiruddin, H. Optimisation of graphene grown from solid waste using CVD method. *Int. J. Adv. Manuf. Technol.* **106**, 211–218 (2020).

129. Senocq, F., Duminica, F.-D., Maury, F., Delsol, T. & Vahlas, C. Iron Thin Films from Fe(CO)[sub 5] and FeCp[sub 2]/H[sub 2]O under Atmospheric Pressure. *J. Electrochem. Soc.* **153**, G1025 (2006).

130. Wang, C., Ryman, C. & Dahl, J. Potential CO2 emission reduction for BF–BOF steelmaking based on optimised use of ferrous burden materials. *Int. J. Greenh. Gas Control* **3**, 29–38 (2009).

131. Karlsson, M. N. A., Deppert, K., Wacaser, B. A., Karlsson, L. S. & Malm, J.-O. Size-controlled nanoparticles by thermal cracking of iron pentacarbonyl. *Appl. Phys. A* **80**, 1579–1583 (2005).

132. Langford, J. I. & Wilson, A. J. C. Scherrer after sixty years: A survey and some new results in the determination of crystallite size. *J. Appl. Crystallogr.* **11**, 102–113 (1978).

133. Hubbard, C. R. & Snyder, R. L. RIR - Measurement and Use in Quantitative XRD. *Powder Diffr.* **3**, 74–77 (1988).

134. Błoński, P. & Kiejna, A. Calculation of surface properties of bcc iron. *Vacuum* **74**, 179–183 (2004).

135. Aviziotis, I. G., Duguet, T., Vahlas, C. & Boudouvis, A. G. Combined Macro/Nanoscale Investigation of the Chemical Vapor Deposition of Fe from $Fe(CO)_5$. *Adv. Mater. Interfaces* **4**, 1601185 (2017).

136. Sorescu, D. C., Thompson, D. L., Hurley, M. M. & Chabalowski, C. F. First-principles calculations of the adsorption, diffusion, and dissociation of a CO molecule on the Fe(100) surface. *Phys. Rev. B* **66**, 035416 (2002).

137. Dwyer, D. The catalytic reduction of carbon monoxide over iron surfaces: A surface science investigation. *J. Catal.* **87**, 66–76 (1984).

138. Yoshida, K. & Somorjai, G. A. The chemisorption of CO, CO2, C2H2, C2H4, H2 and NH3 on the clean Fe(100) and (111) crystal surfaces. *Surf. Sci.* **75**, 46–60 (1978).

139. Walker, P. L., Rakszawski, J. F. & Imperial, G. R. Carbon Formation from Carbon Monoxide-Hydrogen Mixtures over Iron Catalysts.I. Properties of Carbon Formed. *J. Phys. Chem.* **63**, 133–140 (1959).

140. Boehm, H. P. Carbon from carbon monoxide disproportionation on nickel and iron catalysts: Morphological studies and possible growth mechanisms. *Carbon* **11**, 583–590 (1973).

141. Ruston, W. R., Warzee, M., Hennaut, J. & Waty, J. The solid reaction products of the catalytic decomposition of carbon monoxide on iron at 550°C. *Carbon* **7**, 47–57 (1969).

142. El-Sesy, I. A. & El-Baradie, Z. M. Influence carbon and/or iron carbide on the structure and properties of dual-phase steels. *Mater. Lett.* **57**, 580–585 (2002).

143. Narkiewicz, U., Podsiadły, M., Jędrzejewski, R. & Pełech, I. Catalytic decomposition of hydrocarbons on cobalt, nickel and iron catalysts to obtain carbon nanomaterials. *Appl. Catal. Gen.* **384**, 27–35 (2010).

144. Dry, M. Factors influencing the formation of carbon on iron Fischer-Tropsch catalysts II. The effect of temperature and of gases and vapors present during Fischer-Tropsch synthesis. *J. Catal.* **17**, 347–354 (1970).

Acknowledgements

I would like to thank first of all Professor Ludovico Cademartiri for his availability and full support during the whole period of my PhD.

I am also deeply grateful to Professor Enrico Dalcanale, an exemplary coordinator who always put his students before everything else.

A special thanks goes to Professor Daniele Cauzzi, not only for his assistance and expertise in research, but also for his warmth and humor outside the academic environment.

I extend my heartfelt thanks to Beppe for his kindness, to Ferdinando for his reliable help and availability in critical moments and to Dr. Andrea Migliori and Franco Corticelli for their essential contributions to the SEM measurements.

I am deeply grateful to Dr. Emmanuele Parisi from PoliTO, who offered his help even before I could ask for it. My gratitude also goes to Prof. Lara Righi for her friendly presence and to Prof. Francesco Mezzadri for his support and guidance in XRD measurements.

I would like to thank Professors Paolo Mazzeo and Matteo Tegoni for their availability and for giving me the opportunity to attend important schools and conferences that have enriched my academic experience. A special thanks to Dr. Giuliana Aquilanti and the XAFS team of ELETTRA for their precious support and acceptance of my proposal.

Let me now switch to Italian, for a less formal thanks.

Ai miei colleghi, grazie per aver condiviso questi anni con me. Una menzione particolare va a quelli poi diventati grandi amici, come Michele (capo della gang della Conad), Manuel (compagno di sventure, ma pieno di risorse) e Flavia ("la laureanda"), presenti e affidabili anche nei momenti difficili.

Ai miei amici lontani, grazie per non essersi mai dimenticati di me, anche nei miei momenti di sparizione.

Ai miei genitori, grazie per non avermi mai fatto mancare il vostro sostegno e la vostra fiducia in tutti questi lunghi anni, nonostante la distanza e il tempo trascorso. Anche se con poche parole so che potremo sempre capirci. Ciao Kev, fa lu brav!

E, dulcis in fundo, grazie a Chiara. Lei, anzi, tu ci sei sempre. Non basterebbe scrivere un'altra tesi per dirti tutto, ma sarebbe inutile, lo sai, meglio farlo insieme ogni giorno, come veri cuties!

A tutti coloro che non ho nominato qui, eppure hanno contribuito tanto o pochissimo che sia, nel bene e nel male, ma comunque in maniera fondamentale a farmi giungere a questo punto, io voglio dire grazie, perché ora solo felice.